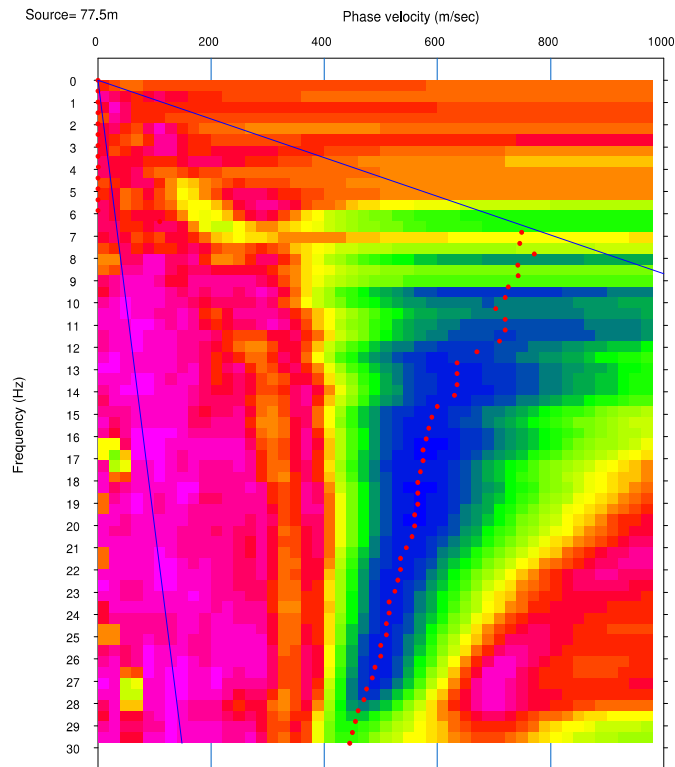


Probabilistic Seismic Hazard Assessment and Observed Ground Motions for the Arcadia, Oklahoma, Dam Site

AUSTIN A. HOLLAND, CHRISTOPHER R. TOTH, AND EMMA M. BAKER



OKLAHOMA GEOLOGICAL SURVEY
THE UNIVERSITY OF OKLAHOMA
MEWBOURNE COLLEGE OF EARTH & ENERGY
Sarkeys Energy Center
100 East Boyd St., Rm. N-131
Norman, Oklahoma 73019-0628

SPECIAL PUBLICATION SERIES

The Oklahoma Geological Survey's Special Publication series is designed to bring new geologic information to the public in a manner efficient in both time and cost. The material undergoes a minimum of editing and is published for the most part as a final, author-prepared report.

Each publication is numbered according to the year in which it was published and the order of its publication within that year. Gaps in the series occur when a publication has gone out of print or when no applicable publications were issued in that year.

This publication is issued by the Oklahoma Geological Survey as authorized by Title 70, Oklahoma Statutes, 1971, Section 3310, and Title 74, Oklahoma Statutes, 1971, Sections 231-238.

This publication is only available as an electronic publication.

1 Summary

Earthquake activity within Oklahoma has increased more than an order of magnitude since late 2009. This rate increase is significant and unprecedented with dramatic implications for the seismic hazard throughout Oklahoma. The seismicity observed in this time period is primarily concentrated within central Oklahoma where, prior, there had only been a few earthquakes observed. This seismicity is concentrated just east of Oklahoma City and activity occurring on the Wilzetta Fault near Prague, Oklahoma. This increase in earthquakes within central Oklahoma raises concern about a previous study by the Oklahoma Geological Survey (OGS) that assess the seismic hazard and ground-motion potential from future earthquakes (Lawson, 1985). This study clearly states that the major assumptions made in the seismic hazard assessment were that earthquakes would continue to occur in areas that had been seismically active, at comparable rates through time, and that the past seismicity could be used to define the most active areas of the state.

These assumptions have been invalidated by the recent earthquake activity. Ground-motions for the November 5, 2011 M5.6 Prague, Oklahoma, earthquake most likely exceeded the 2,000-year estimated maximum ground-motions at the Arcadia Dam site for the previous study by Lawson (1985). This study will provide a modern Probabilistic Seismic Hazard Assessment (PSHA) for the Arcadia Dam. The goal is to provide realistic ground-motion estimates based on another 35 years of seismicity observations and advances in PSHA techniques in accordance with the U.S. Army Corp of Engineers Regulation No. ER 1110-2-1806. This study used newly available open-source software for PSHA calculations (Crowley et al., 2012; Field et al., 2003). We did not distinguish the seismicity through micro-zonation, but instead consider the likelihood of seismicity throughout Oklahoma. This removed the assumption from the PSHA that future seismicity will follow past spatial seismicity patterns.

It remains unclear how to best account for a significant change in earthquake recurrence rates that were observed in Oklahoma from 2009 through 2012. Generally PSHA studies assume constant rates through time. However, this model does not work for the recent earthquake activity in Oklahoma. Rate changes at this scale are unprecedented so there was no documented method to deal with such changes. The final PSHA models attempted to address contributions from seismicity rate changes. We assigned a 20% likelihood of earthquakes that occur at the new rate and an 80% likelihood to the rate of earthquake occurrence prior to the increase in seismicity. V_{s30} is the shear wave velocity within 30 m of the surface and is used to characterize soil stiffness and site conditions applicable to ground motion predictions. V_{s30} measurements near the Arcadia Dam provided very different results (281 and 628 m/s) such that both V_{s30} cases were considered in the final PSHA. The V_{s30} value of 281 m/s was measured below the dam, and the V_{s30} value greater than 600 m/s was measured near the Arcadia Dam office. For two final cases mean equal hazard spectral amplitudes (UHS) are shown in Tables 1.1 and 1.2. A V_{s30} calculated for the V_{s30} value of 281 m/s provides greater ground motions than for a V_{s30} value of 600 m/s. It remains unclear if the 281 m/s simply represents backfill or geologic conditions on which the dam was constructed. Accelerations determined in this study for the V_{s30} values of 600 m/s are roughly consistent with the results of Lawson (1985). However, for the V_{s30} value of 281 m/s the ground motion predictions are larger in this study. Until it is determined which V_{s30} value most

accurately represents the geologic conditions beneath the Arcadia Dam, it is recommended to use the PSHA results for a Vs30 of 281 m/s.

Table 1.1 – Mean UHS for acceleration in units of g for different spectral amplitude periods and return periods for the case where Vs30 is 600 m/s.

Return Period (years)	72	144	475	950	2000	5000	10000	
Period (s)	0.01	1.29E-02	2.13E-02	4.02E-02	5.28E-02	6.74E-02	9.14E-02	1.18E-01
	0.02	1.31E-02	2.18E-02	4.08E-02	5.36E-02	6.86E-02	9.31E-02	1.20E-01
	0.03	1.37E-02	2.30E-02	4.30E-02	5.66E-02	7.30E-02	1.01E-01	1.28E-01
	0.05	1.57E-02	2.72E-02	5.16E-02	6.78E-02	8.76E-02	1.21E-01	1.55E-01
	0.08	1.97E-02	3.49E-02	6.52E-02	8.56E-02	1.10E-01	1.56E-01	1.99E-01
	0.10	2.31E-02	4.08E-02	7.65E-02	9.99E-02	1.30E-01	1.81E-01	2.34E-01
	0.30	2.23E-02	3.92E-02	7.36E-02	9.83E-02	1.27E-01	1.66E-01	2.12E-01
	0.50	1.39E-02	2.51E-02	4.85E-02	6.57E-02	8.61E-02	1.13E-01	1.41E-01
	1.00	8.03E-03	1.10E-02	2.23E-02	3.05E-02	4.22E-02	5.65E-02	6.68E-02
	2.00	5.59E-03	6.53E-03	8.89E-03	1.18E-02	1.65E-02	2.30E-02	2.82E-02
	3.00	5.12E-03	5.47E-03	6.54E-03	7.51E-03	9.24E-03	1.26E-02	1.57E-02
	4.00	5.02E-03	5.15E-03	5.70E-03	6.28E-03	7.16E-03	8.97E-03	1.08E-02

Table 1.2 – Mean UHS for acceleration in units of g for different spectral amplitude periods and return periods for the case where Vs30 is 281 m/s.

Return Period (years)	72	144	475	950	2000	5000	10000	
Period (s)	0.01	1.64E-02	2.77E-02	5.01E-02	6.49E-02	8.01E-02	1.09E-01	1.37E-01
	0.02	1.65E-02	2.80E-02	5.06E-02	6.55E-02	8.09E-02	1.11E-01	1.40E-01
	0.03	1.71E-02	2.93E-02	5.28E-02	6.82E-02	8.48E-02	1.17E-01	1.47E-01
	0.05	1.95E-02	3.37E-02	6.06E-02	7.75E-02	9.82E-02	1.35E-01	1.71E-01
	0.08	2.42E-02	4.20E-02	7.49E-02	9.48E-02	1.20E-01	1.66E-01	2.13E-01
	0.10	2.89E-02	4.96E-02	8.75E-02	1.12E-01	1.41E-01	1.97E-01	2.49E-01
	0.30	3.25E-02	5.56E-02	9.91E-02	1.28E-01	1.62E-01	2.08E-01	2.59E-01
	0.50	2.17E-02	3.81E-02	7.12E-02	9.57E-02	1.24E-01	1.61E-01	1.92E-01
	1.00	1.05E-02	1.74E-02	3.45E-02	4.80E-02	6.47E-02	8.51E-02	1.03E-01
	2.00	6.51E-03	8.22E-03	1.39E-02	1.95E-02	2.69E-02	3.70E-02	4.59E-02
	3.00	5.51E-03	6.31E-03	8.38E-03	1.11E-02	1.51E-02	2.09E-02	2.57E-02
	4.00	5.18E-03	5.61E-03	6.78E-03	8.07E-03	1.04E-02	1.43E-02	1.75E-02

2 Table of Contents

1 Summary.....	i
2 Table of Contents.....	iii
2.1 List of Figures.....	iv
2.2 List of Tables.....	vii
3 List of Electronic Data Associated With Digital Copy	viii
4 Introduction.....	1
5 Earthquake Catalog.....	2
5.1 Catalog De-Clustering.....	5
5.2 Catalog Completeness and Earthquake Recurrence	7
6 Vs30 Method and Results	16
6.1 Field Methods	16
6.2 Data Analysis.....	18
6.3 Results	19
7 Ground Motion Measurements and Site Amplification.....	28
7.1 Method.....	28
7.2 Conversion from Instrumental Records to Ground Motion Records	29
7.3 TA and ADOK Site Amplification Factors	29
7.4 M5.6 Epicentral and ADOK Spectral Acceleration	31
7.5 Results.....	32
8 Meers Fault.....	36
8.1 Geologic Background.....	36
8.2 Structure of the Meers Fault.....	37
8.3 Previous Studies of the Meers Fault.....	39
8.4 Recurrence Intervals of the Meers Fault.....	39
9 Probabilistic Seismic Hazard Assessment.....	40
9.1 Earthquake Source Models	40
9.2 Maximum Magnitude	40
9.3 Ground Motion Prediction Equations	41
9.4 Comparison of Area Sources in PSHA.....	44
9.5 Meers Fault PSHA Parameters.....	49
10 Results of PSHA for Arcadia Dam.....	54
11 Recommendations.....	58
12 Acknowledgements.....	58
13 References.....	59
Appendix A - Table of Abbreviations.....	62

List of Figures

Figure 5.1 – Comparison of OGS measured \ln and M_w along with published relationships between \ln and M_w (Hanks and Kanamori, 1979; Miao and Langston, 2007). 4

Figure 5.2 – \ln - M_w relationship determined from this study with 23 observations. The fit to the linear relationship has a b value of 0.893. 5

Figure 5.3 – Complete earthquake catalog from 1882-2011 for all of Oklahoma. Earthquakes are shown as red + scaled by magnitude. Regional faults are shown as thick solid black lines from (Northcutt and Campbell, 1995). 6

Figure 5.4– De-clustered earthquake catalog from 1882-2011 for all of Oklahoma. Earthquakes are shown as red + scaled by magnitude. Regional faults are shown as thick solid black lines from (Northcutt and Campbell, 1995). 7

Figure 5.5 – Stepp plots for the time period of 1882-2008 with annual rates of recurrence for the complete earthquake catalog. 9

Figure 5.6 – Stepp plots for the time period of 1882-2008 with annual rates of recurrence for the de-clustered earthquake catalog. 10

Figure 5.7 – Stepp plots for the time period of 1882-2011 with annual rates of recurrence for the complete earthquake catalog. 11

Figure 5.8 – Stepp plots for the time period of 1882-2011 with annual rates of recurrence for the de-clustered earthquake catalog. 12

Figure 5.9 – Gutenberg-Richter relationship for the time period 1882-2008 de-clustered catalog determined using the correction for catalog completeness (Weichert, 1980), where $b=1.082\pm 0.138$, and $a=3.167\pm 0.230$ 13

Figure 5.10 – Gutenberg-Richter relationship for the time period 1882-2011 de-clustered catalog determined using the correction for catalog completeness (Weichert, 1980), where $b=1.099\pm 0.108$ and $a=3.436\pm 0.277$ 14

Figure 5.11 – Gutenberg-Richter relationship for the time period 2009-2011 de-clustered catalog determined using the maximum likelihood estimator for b-value (Bender, 1983), where $b=0.951\pm 0.051$ and $a=4.21\pm 0.226$ 15

Figure 5.12 – Gutenberg-Richter relationship for the time period 2009-2011 complete catalog determined using the maximum likelihood estimator for b-value (Bender, 1983), where $b=1.06\pm 0.022$ and $a=5.163\pm 0.122$ 16

Figure 6.1 - Location of 57.5 m ADOK MASW survey by OGS seismic monitoring station, depicted by the red line. The shown intersection is of Old Route 66/Edmond Rd and S. Douglas Blvd in Edmond, OK. The building is the Army Corps of Engineers Arcadia Dam facility. Image courtesy of Google Earth. 17

Figure 6.2 - Location of 57.5m Arcadia Dam MASW survey directly east of Arcadia Dam, depicted by the red line. The edge of Lake Arcadia is shown on the western edge of the picture, and the spillway is shown to the north and east of the survey line. Image courtesy of Google Earth. 18

Figure 6.3 - Dispersion curve of ADOK long source offset MASW survey. Blue regions indicated better correlations of phase velocity to the observed frequency dispersion. Phase velocities could only be analyzed down to 7 Hz and lower frequencies were unresolvable. 20

Figure 6.4 - Dispersion curve of ADOK short source offset MASW survey. Blue regions indicated better correlations of phase velocity to the observed frequency dispersion. Phase velocities could only be analyzed down to 13 Hz and most lower frequencies were unresolvable. 21

Figure 6.5 - Dispersion curve of Arcadia Dam long offset MASW survey. Blue regions indicated better correlations of phase velocity to the observed frequency dispersion. Phase velocities could be analyzed down to 4 Hz.....	22
Figure 6.6 - Dispersion curve of Arcadia Dam long offset MASW survey. Blue regions indicated better correlations of phase velocity to the observed frequency dispersion. Phase velocities could be analyzed between 6 Hz to 50 Hz.....	23
Figure 6.7 - Dispersion plot of ADOK combining the long and short source offset surveys with overlapping values averaged. Overlapping values occurred between in the range of 10 to 30 Hz.	24
Figure 6.8 - Dispersion plot of Arcadia Dam combining the two long source offset surveys. Overlapping phase velocities were not averaged, creating a sawtooth appearance in the dispersion plot.....	25
Figure 6.9 - Shear-wave velocity model down to 30 m for ADOK. This model is the result of inversion with 5 iterations. The RMS error of the model was reduced from 49.1 m/sec to 34.1 m/sec during the inversion.....	26
Figure 6.10 - Shear-wave velocity model down to 30 m for Arcadia Dam. This model is the result of inversion with 5 iterations. The RMS error of the model was reduced from 49.1 m/sec to 34.1 m/sec during the inversion.....	27
Figure 7.1 - Location of seismic stations (circles) with station identification codes within Oklahoma. The ground motion study stations are coded by network where GS and US are USGS stations, OK are OGS seismic stations, and TA are Earthscope Transportable Array stations. Earthquakes observed at ADOK and used for ground-motion calculations (Figure 7.3) at ADOK are shown as red crosses scaled by magnitude. Faults (Northcutt and Campbell, 1995) are shown as thick black lines.	29
Figure 7.2 - Vertical site amplifications at ADOK for individual events, plotted against: a.) Distance from the epicenter to ADOK, and b.) Azimuth from the epicenter to ADOK. The linear scale shows positive skew in the data. Because no correlation between site amplification, distance and azimuth was apparent, variation in individual site amplifications is likely due to source characteristics.	32
Figure 7.3 - Calculated peak horizontal spectral accelerations experienced at ADOK. Values are derived from the removal of instrument response from the seismogram.....	35
Figure 9.1 - Area source logic tree for the case shown in the final results. Earthquake occurrence models are shown above a branch line and the probability of occurrence for that branch is shown in parentheses below the branch line. This considers the occurrence of the increased clustered seismicity to be much less likely than the de-clustered earthquake rates.....	42
Figure 9.2 - M_{max} logic tree used for the determination of a truncated Gutenberg-Richter relationships for area source within the PSHA. The maximum magnitude model is listed above the branch line and the probability of occurrence for that branch is shown in parentheses below the branch line.....	43
Figure 9.3 - Complete logic tree including only area sources used for comparing results of PSHA from the different area sources.....	44
Figure 9.4 - Mean UHS for the de-clustered area source model is based on the Gutenberg-Richter recurrence parameters for the de-clustered earthquake catalog from 1882-2011 using a Vs30 of 600 m/s. The de-clustered logic-tree is available in the Electronic Supplement ES5.....	45

Figure 9.5 - Mean UHS for the clustered area source model is based on the Gutenberg-Richter recurrence parameters for the complete catalog from 2009-2011 using a V_{s30} of 600 m/s. The clustered logic tree is available in the Electronic Supplement ES5. 46

Figure 9.6 - Mean UHS for the complete logic tree and area point sources instead of line sources with a V_{s30} of 600 m/s. The complete logic tree is available in the Electronic Supplement ES5 and can be seen in Figure 9.3. 47

Figure 9.7 - Mean UHS for the complete area source logic tree using cross-hair line sources with a V_{s30} of 600 m/s. The complete logic-tree is available in the Electronic Supplement ES5 and can be seen in Figure 9.3. 48

Figure 9.8 - Mean UHS for the complete area source logic-tree using cross-hair line sources with a V_{s30} of 281 m/s. The complete area source logic tree is available in the Electronic Supplement ES5 and can be seen in Figure 9.3. 49

Figure 9.9 - Mean UHS computed for different return periods at the Arcadia Dam for the USGS hazard model (Petersen et al., 2008) for the Meers Fault. 50

Figure 9.10 - Mean UHS for different return periods at the Arcadia Dam for strike-slip earthquakes on the Meers Fault. 51

Figure 9.11 - Mean UHS for different return periods at the Arcadia Dam for earthquakes with mostly strike-slip and a component of reverse motion on the Meers Fault. 52

Figure 9.12 - Mean UHS for a return period of 10,000 years for different recurrence rates of a magnitude 7.1 earthquake on the Meers Fault. 53

Figure 10.1 - Complete logic tree for final PSHA calculations. The Meers Fault is not a distinct source, but is included as a source with the shown parameters in each source model. The complete logic tree in expanded format is available in the Electronic Supplement ES5. 55

Figure 10.2 - Mean UHS for different return periods for the case where V_{s30} is 600 m/s. The complete logic tree is available in the Electronic Supplement ES5 and can be seen in Figure 10.1. 56

Figure 10.3 - Mean UHS for different return periods for the case where V_{s30} is 281 m/s. The complete logic tree is available in the Electronic Supplement ES5 and can be seen in Figure 10.1. 57

2.1 List of Tables

Table 1.2 - Mean UHS for acceleration in units of g for different spectral amplitude periods and return periods for the case where V_{s30} is 281 m/s.	ii
Table 5.1 - Moment magnitude relationships for different instrumental magnitude measurements.	3
Table 5.2 - Moment magnitude relation to maximum Modified Mercalli Intensity Relationship (Johnston, 1996b).....	3
Table 5.3 - Periods of completeness in the de-clustered earthquake catalog by magnitude interval determined from Stepp plots.	8
Table 7.1 - Table of frequency dependent coefficients originally presented in Atkinson (2004). Values were not always provided for exactly 0.3, 1, 3, and 10 Hz in the various tables. Where this is the case, the values used in this study and presented here were obtained by linear interpolation with the two nearest provided values.	30
Table 7.2 Vertical site amplifications and standard deviations, values are expressed as the average of the log10 site amplifications plus/minus one standard deviation.....	33
Table 7.3 - Horizontal site amplifications and standard deviations, values are expressed as the average of the log10 site amplifications plus/minus one standard deviation.	34
Table 7.4 ADOK peak ground accelerations estimated for the Magnitude 5.6 November 5, 2011 earthquake.	35
Table 9.1 - Inferred Gutenberg-Richter a-values for different recurrence intervals of magnitude 7.1 earthquakes on the Meers Fault assuming a b-value of 1.0.....	53
Table 10.1 - Mean UHS for acceleration in units of g for different spectral amplitude periods and return periods for the case where V_{s30} is 600 m/s.	55
Table 10.2 - Mean UHS for acceleration in units of g for different spectral amplitude periods and return periods for the case where V_{s30} is 281 m/s.	56
Table 10.3 - Standard deviation values in acceleration units of g for the mean UHS values reported in this study. Demonstrating the significant variability between different logic-tree samples.	57

3 List of Electronic Data Associated With Digital Copy

- ES1. Comma Separated Values (CSV) spreadsheet of compiled earthquake catalog and documentation of fields. Compiled in a zip file.
- ES2. Shape files and large format digital maps of both the complete compiled earthquake catalog and the de-clustered earthquake catalog. Compiled in a zip file.
- ES3. Phase-picks from Vs30 dispersion curves and the original MASW data. Compiled in a zip file.
- ES4. ADOK accelerograms corrected for instrument response and uncorrected with corresponding response files used to correct waveform recordings. Compiled in a zip file.
- ES5. Complete logic trees used for different PSHA scenarios in expanded digital format.
- ES6. Input files to control the OpenQuake PSHA calculations and associated output for each case. Compiled in a zip file.
- ES7. Compilation of computer programs and raw data used in this study not in previous supplements. Compiled in a zip file.

4 Introduction

Earthquake activity within Oklahoma has increased more than an order of magnitude since late 2009. This rate increase is significant and has implications for the seismic hazard throughout Oklahoma. The seismicity observed in this time period is primarily concentrated within central Oklahoma, just east of Oklahoma City, and activity occurring on the Wilzetta Fault near Prague, Oklahoma. This increase in earthquakes within central Oklahoma raises concern about a previous study by the Oklahoma Geological Survey (OGS) that assess the seismic hazard and ground-motion potential from future earthquakes (Lawson, 1985). This study clearly states that the major assumptions made in the seismic hazard assessment were that earthquakes would continue to occur in areas that had been seismically active and at comparable rates, and that the past seismicity could be used to define the most active areas of the state.

These assumptions have been invalidated by the recent earthquake activity. In fact ground-motions for the November 5, 2011 M5.6 Prague, Oklahoma, earthquake may have exceeded the 2000 design ground-motions for the previous study (Lawson, 1985). This study will provide a modern Probabilistic Seismic Hazard Assessment (PSHA) for the Arcadia Dam. The goal is to provide realistic ground-motion estimates based on another 35 years of seismicity observations and advances in PSHA techniques in accordance with the U.S. Army Corp of Engineers Regulation No. ER 1110-2-1806. This study used newly available open-source software for PSHA calculations (Crowley et al., 2012; Field et al., 2003). In addition we do not distinguish the seismicity through micro-zonation, but instead consider the likelihood of seismicity throughout Oklahoma. This removes the assumption from PSHA that future seismicity will follow past spatial seismicity patterns.

It remains unclear how to best account for a significant change in earthquake recurrence rates that was observed in Oklahoma from 2009 through 2012. Generally PSHA studies assume constant rates through time. However, this model will not work for the recent earthquake activity in Oklahoma. The final PSHA models attempted to address contributions from seismicity rate changes, but this magnitude of rate change may be unprecedented.

This work required careful compilation of the earthquake catalog, determination of catalog completeness, and earthquake recurrence rates. These recurrence rates were used as inputs for the area sources included in the PSHA. In addition, we conducted MASW Vs30 profiling to determine the potential soil amplification effects at the Arcadia Dam. Vs30 is used to classify soils at a site and has a large impact on the site amplification (Dobry et al., 2000). The measured Vs30 values were used in final PSHA calculations. We also evaluated ground-motions that were directly measured or can be reasonably inferred from recent earthquakes within Oklahoma using accelerometers operating within the area, one was located at the Arcadia Dam Office, and regional seismic stations. We addressed the additional hazard associated with the Meers Fault, which is the only known Quaternary fault with surface expression in Oklahoma. Finally we demonstrate the sensitivities of PSHA input parameters and their effect on the computed hazard and calculated the mean UHS for two final cases.

5 Earthquake Catalog

The Oklahoma earthquake catalog was compiled from previously compiled earthquake catalogs from the Oklahoma Geological Survey and the U.S. Geological Survey (USGS, 2012a). Both the USGS Preliminary Determination of Epicenters (PDE) and historical earthquake databases were used as sources for the compiled catalog. Any earthquakes without an origin time known to at least the hour were discarded from the compiled catalog. The OGS catalog was considered the primary data source for origin times and hypocenters. Information from the USGS catalog was only used when an earthquake was not in the OGS catalog. It is so noted in the catalog. USGS and OGS earthquakes were considered the same if the origin times were within 10 seconds of each other. Magnitude measurements in the USGS catalog not attributed to the OGS network “TUL” were added to the database and are noted as being from the USGS. Except for Mw, where the source is tracked for this compilation, with all mb, Ms, MS, MFA, and Mw data coming from the USGS earthquake catalog.

A single magnitude for each earthquake within the catalog was necessary. The general choice for such a magnitude estimate is the moment magnitude, **Mw** or **M**. Most earthquakes within the Oklahoma earthquake catalog do not have measured moment magnitudes. The available magnitudes or intensity measures were used to calculate an estimated **M** moment magnitude and associated uncertainty. This was done using a weighted average of the estimated moment magnitudes and their uncertainties following equations. Given N , number of estimates, **M** the weighted mean can be described as

$$\bar{M} = \frac{\sum_{i=1}^N M_i / \sigma_i^2}{\sum_{i=1}^N 1 / \sigma_i^2}, \quad (0.1)$$

and the variance of this estimate as

$$\sigma_{\bar{M}}^2 = \frac{1}{\sum_{i=1}^N \sigma_i^2}. \quad (0.2)$$

These equations determined an estimated moment magnitude and its associated uncertainty based on multiple magnitude measures. If each magnitude estimate used in Equation 5.1 was independent and normally distributed with the same mean, or moment magnitude, then this equation provided a maximum likelihood estimator of **M**. The relationships used in this study are relationships between **M** and other magnitude or earthquake intensity measures in the published literature with preference to relationships determined from data in Central or Eastern North America or other stable continental regions. The relationships used from instrumental measurements of magnitude are shown in Table 5.1. The relationship used for the Maximum Modified Mercalli Intensity (I_0) is shown in Table 5.2. All measured magnitudes and intensities for each earthquake contribute to the estimated moment magnitude. In the case where there are available moment magnitude measurements, these values are used instead. If more than one moment magnitude measurement was available for an earthquake then the moment magnitude was the weighted average following Equations 5.1 and 5.2. The available moment magnitude measures and the source were indicated as “OGSD” indicating an OGS derived moment magnitude.

The OGS began using M_L magnitudes in 2010 by developing a local magnitude relationship following the method of (Miao and Langston, 2007). Because each M_L relationship is based on regional attenuation values, an estimated moment will vary between different M_L relationships. The CEUS-SSC (2012) evaluated many magnitude relationships for the Central and Eastern US, but the M_L relationship currently used by the OGS was not tested. Figure 5.1 shows some M to M_L published relationships. They are clearly not the best fitting relationship for the data. Figure 5.2 shows the M to M_L relationship determined by linear regression for 23 Mw/ M_L observations in the OGS earthquake catalog. The relationship provided a R^2 value of 0.893. This relationship would certainly benefit from more observations, and is likely to be inaccurate above about M5.5 to M6.0.

Table 5.1 – Moment magnitude relationships for different instrumental magnitude measurements.

Magnitude Type	Conversion Relationship	Uncertainty (σ)	Relationship Source
M_S	$M = 5.74 - 0.722M_S + 0.128M_S^2$	0.271	(Johnston, 1996a)
m_b	$M = 1.487 + 0.4527m_b + 0.0513m_b^2$	0.394	(Johnston, 1996a)
m_{bLg}	$M = 1.14 + 0.24m_{bLg} + 0.093m_{bLg}^2$	0.332	(Johnston, 1996a)
M_L	$M = -0.0583 + 1.096M_L$	0.21	This study
M_D	$M = 0.869 + 0.762M_D$	0.25	(CEUS-SSC, 2012)

Table 5.2 – Moment magnitude relation to maximum Modified Mercalli Intensity Relationship (Johnston, 1996b).

Maximum MMI (I_0)	M	σ
II (Felt)	2.9	0.59
III	3.3	0.55
IV	3.8	0.53
V	4.2	0.52
VI	4.7	0.52
VII	5.3	0.52
VIII	5.8	0.52
IX	6.4	0.53

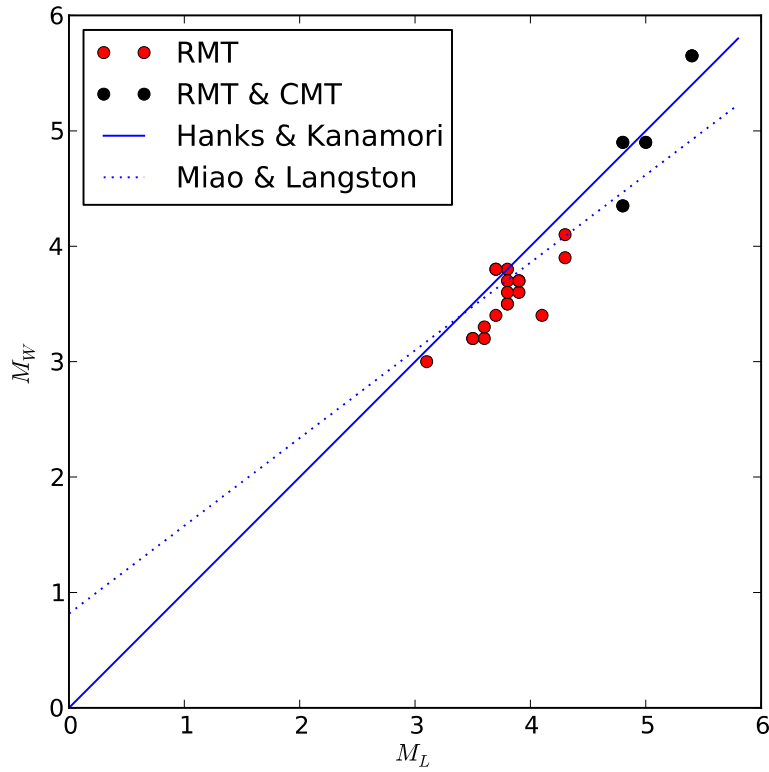


Figure 5.1 – Comparison of OGS measured M_L and M_W along with published relationships between M_L and M_W (Hanks and Kanamori, 1979; Miao and Langston, 2007).

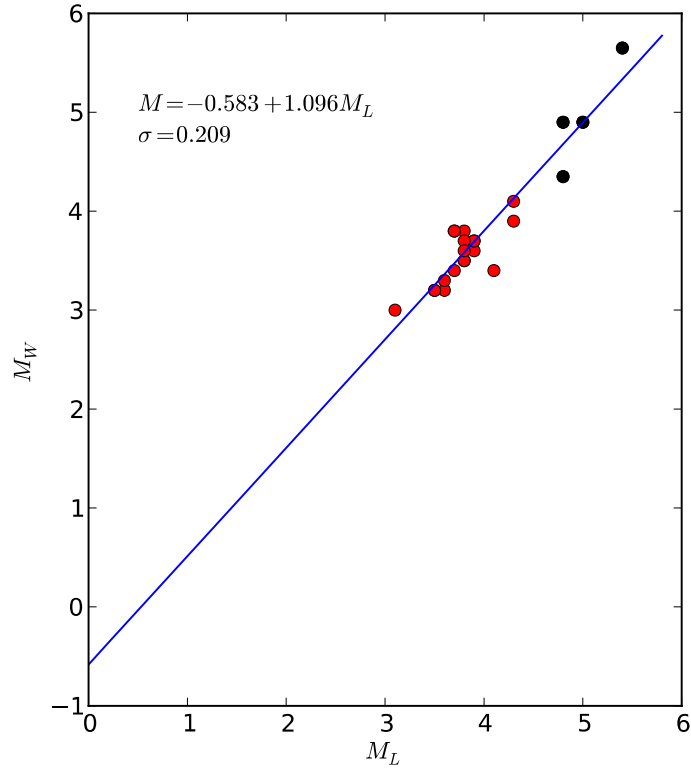


Figure 5.2 – M_L - M_w relationship determined from this study with 23 observations. The fit to the linear relationship has a R^2 value of 0.893.

5.1 Catalog De-Clustering

The PSHA method assumes a Poisson model for independent earthquake occurrence through time. Because of this assumption, the earthquake catalog must be de-clustered to remove dependent earthquakes from the catalog such as foreshocks and aftershocks. This is done following the method of Gardner and Knopoff (1974). This technique creates a spatial and temporal window around an earthquake and assigns an earthquake to be a mainshock, aftershock, or foreshock. The size of the spatial and temporal window in this technique is relative to the magnitude. The spatial window is defined as

$$\log L = 0.1238M + 0.983, \quad (0.3)$$

where L is the distance in kilometers (km), and the temporal window is defined as

$$\begin{aligned} \log T &= 0.5409M - 0.547 & M < 6.5 \\ \log T &= 0.032M + 2.7389 & M \geq 6.5 \end{aligned}, \quad (0.4)$$

where T is time measured in days. The Gardner and Knopoff (1974) method starts with the largest earthquake in the catalog and then identifies all dependent events to that earthquake and then moves onto the next largest independent earthquake and so forth. The original definition was used to identify aftershocks, which are much more common than foreshocks. The

same windowing technique can identify foreshocks and in this case the time window is reduced to $0.2T$. This yielded 313 foreshocks within the compiled catalog. Using this de-clustering algorithm there are 1694 independent earthquakes of the total 5035 earthquakes in the catalog. The clustered and de-clustered catalogs can also be seen in map view in Figures 5.3 and 5.4, and are included in a larger format in the Electronic Supplement ES2.

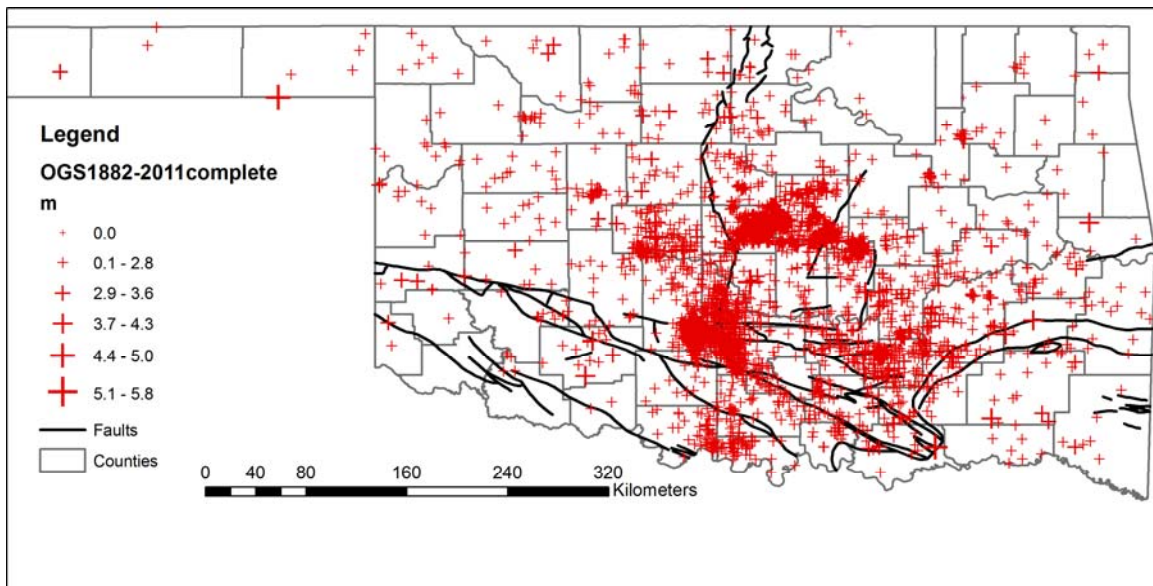


Figure 5.3 – Complete earthquake catalog from 1882-2011 for all of Oklahoma. Earthquakes are shown as red + scaled by magnitude. Regional faults are shown as thick solid black lines from (Northcutt and Campbell, 1995).

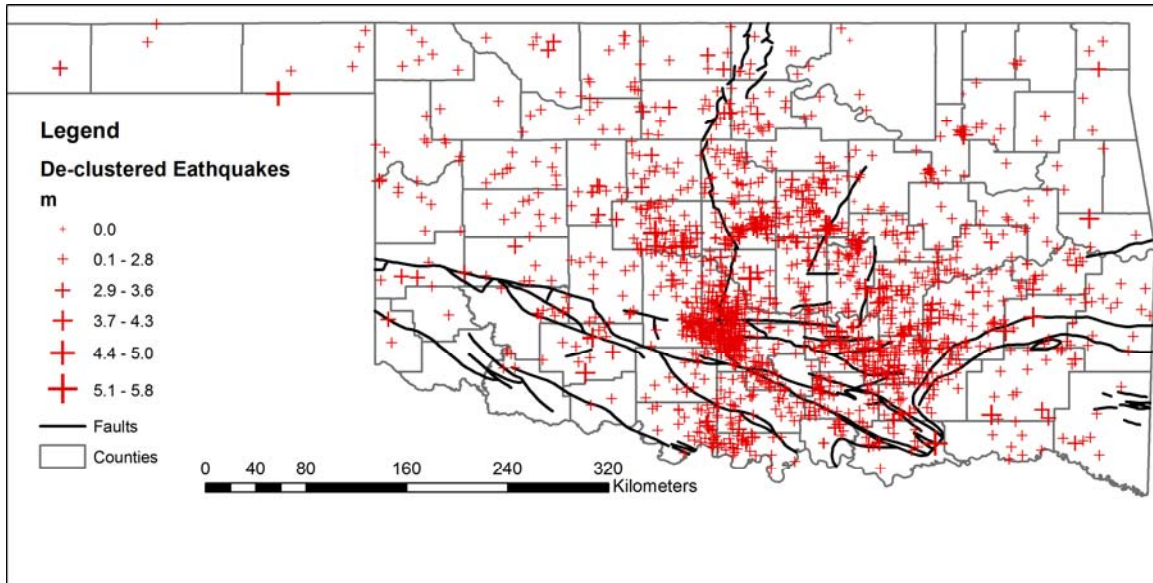


Figure 5.4– De-clustered earthquake catalog from 1882-2011 for all of Oklahoma. Earthquakes are shown as red + scaled by magnitude. Regional faults are shown as thick solid black lines from (Northcutt and Campbell, 1995).

5.2 Catalog Completeness and Earthquake Recurrence

The completeness of an earthquake catalog changes through time. This is in large part a response to changes in seismic monitoring capabilities within the region. The first seismic station in Oklahoma was installed in 1961 and a network of multiple stations was installed in 1978. These network changes are reflected in the determined completeness intervals for the de-clustered catalog through 2008 (Table 5.3). The periods and rough annual rates of completeness were determined using Stepp plots (Stepp, 1972) of the de-clustered catalogs. If the seismicity were a stationary Poissonian process, the annual rate would be a flat line from the present to the period at which the catalog would no longer be complete. Then the annual rate of occurrence decreases through time (CEUS-SSC, 2012). This behavior is generally clear for the larger magnitude earthquakes, but less so for the smaller magnitudes (Figures 5.5 and 5.6). The observed change for smaller magnitude earthquakes could demonstrate that either the completeness for small magnitudes has improved through time or that a stationary Poissonian process cannot model the occurrence of small earthquakes in Oklahoma. This is even more evident when the data is included through 2011. The rates of seismicity increased over the last two years (Figures 5.7 and 5.8).

Table 5.3 – Periods of completeness in the de-clustered earthquake catalog by magnitude interval determined from Stepp plots.

Magnitude Interval	2008 Declustered		2011 Declustered	
	Years	Rate (# Earthquakes per year)	Years	Maximum Rate (# Earthquakes per year)
2.9-3.6	1980	0.155	1980	0.65
3.6-4.3	1960	0.109	1960	0.16
4.3-5.0	1960	0.016	1960	0.023
5.0-5.8	1897	0.007	1897	0.015

The de-clustered catalogs were used to more accurately define a recurrence rate for different magnitudes using the Gutenberg-Richter b - and a -value relationship (Gutenberg and Richter, 1944). This defines the number of earthquakes at a given magnitude that would be expected as

$$\log_{10}(N) = a - bM. \quad (0.5)$$

This formulation does not take into account the different periods of completeness in an earthquake catalog through time. The differences in catalog completeness were accounted for using the method of Weichert (1980). The b -values were determined using the de-clustered catalog for earthquakes occurring prior to 2009 where $b=1.082\pm0.138$ $a=3.167\pm0.230$ (Figure 5.9), and the de-clustered catalog through 2011 where $b=1.099\pm0.108$ $a=3.436\pm0.277$ (Figure 5.10). In addition we look at the a - and b -values for the time-period from 2009 through 2011 without incorporating the completeness interval correction. This time-period was complete to less than magnitude 2.0. The b -value was determined using the maximum likelihood estimator (Aki, 1965) with modifications for magnitude bin widths (Bender, 1983) for magnitudes down to 2.2. This was done for both the de-clustered catalog and the complete catalog (Figures 5.11 and 5.12).

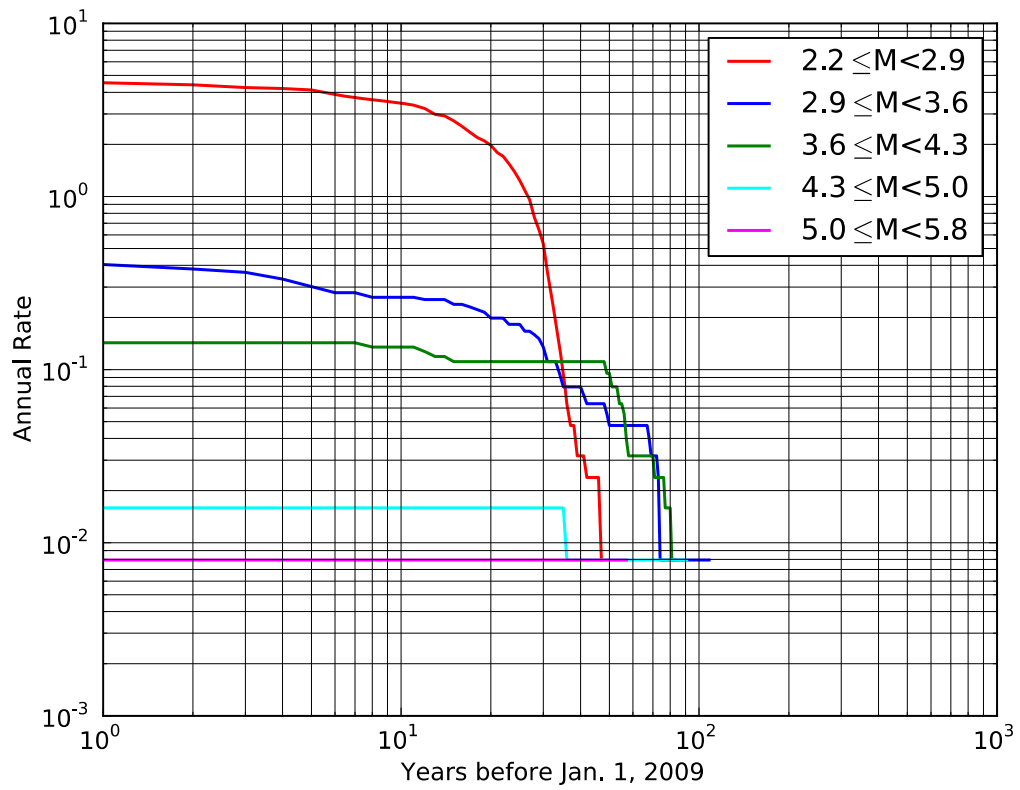


Figure 5.5 – Stepp plots for the time period of 1882-2008 with annual rates of recurrence for the complete earthquake catalog.

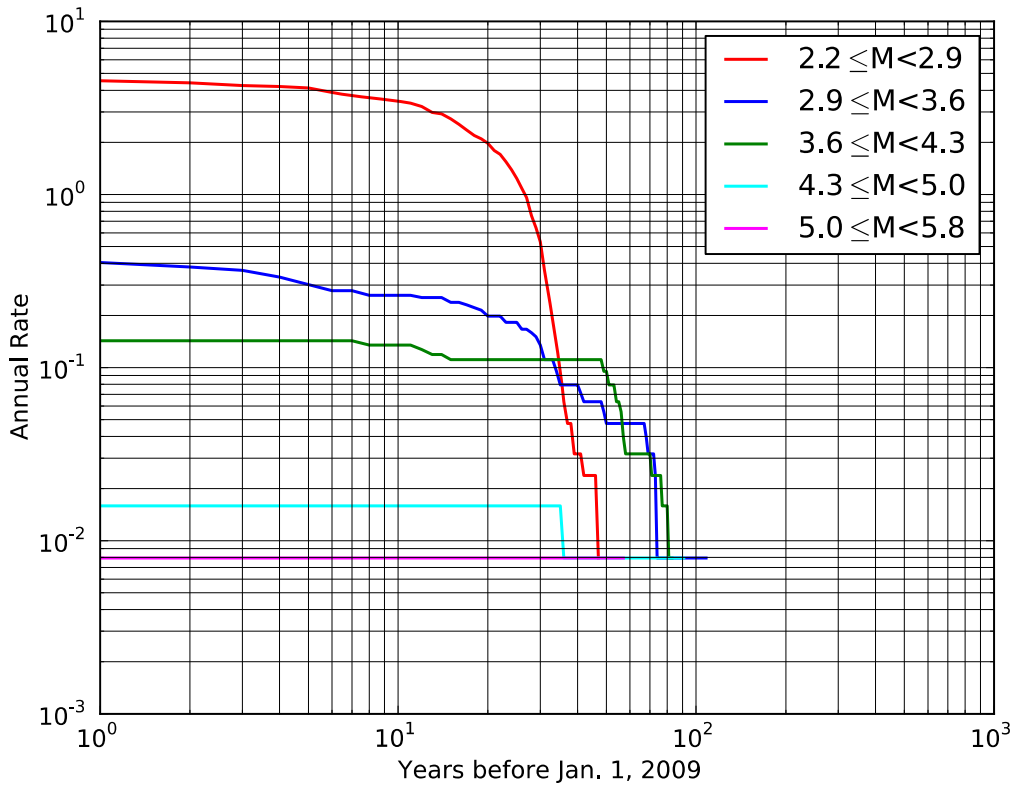


Figure 5.6 – Stepp plots for the time period of 1882-2008 with annual rates of recurrence for the de-clustered earthquake catalog.

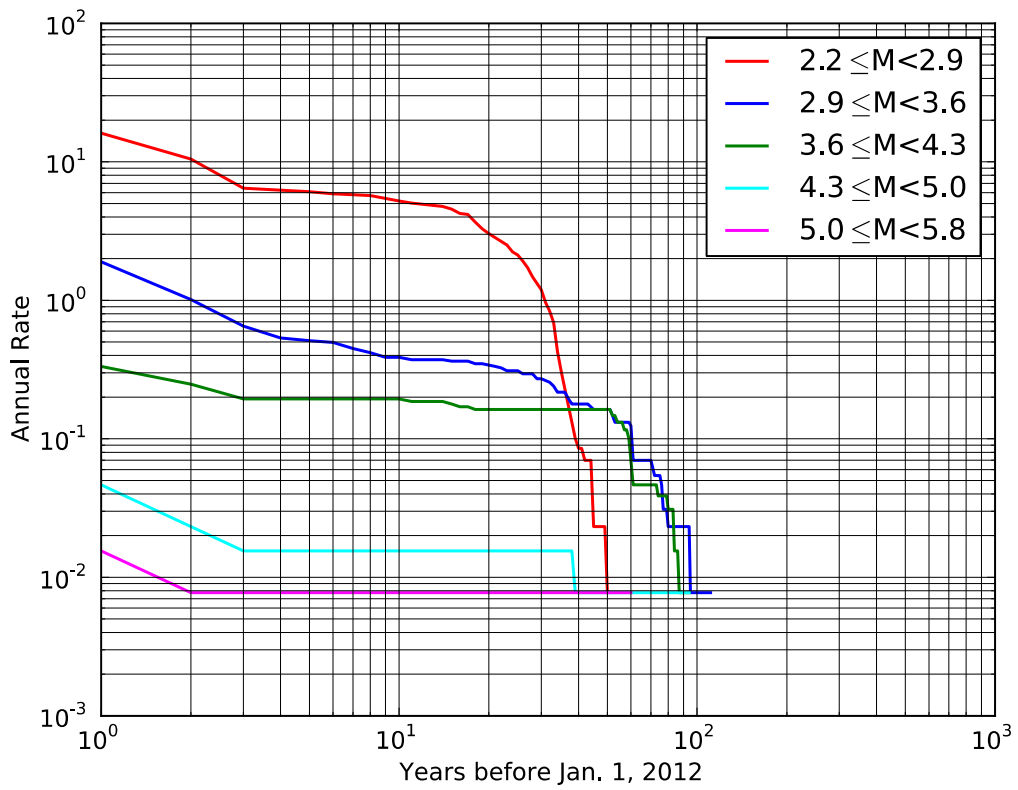


Figure 5.7 – Stepp plots for the time period of 1882-2011 with annual rates of recurrence for the complete earthquake catalog.

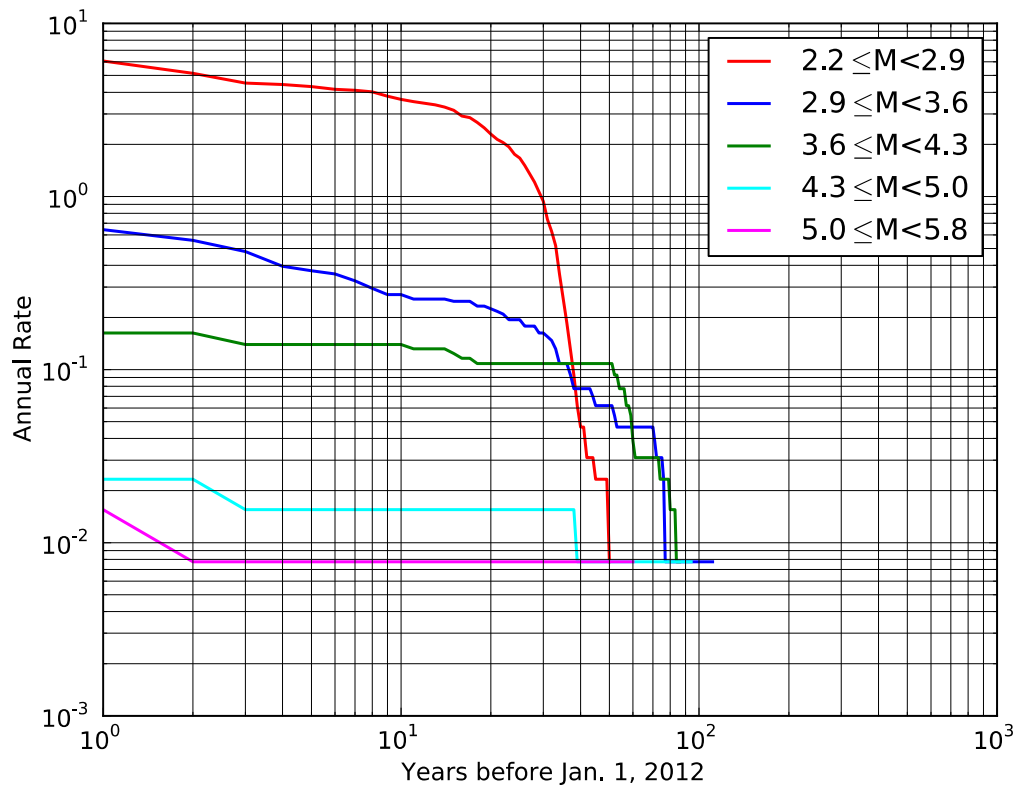


Figure 5.8 – Stepp plots for the time period of 1882-2011 with annual rates of recurrence for the de-clustered earthquake catalog.

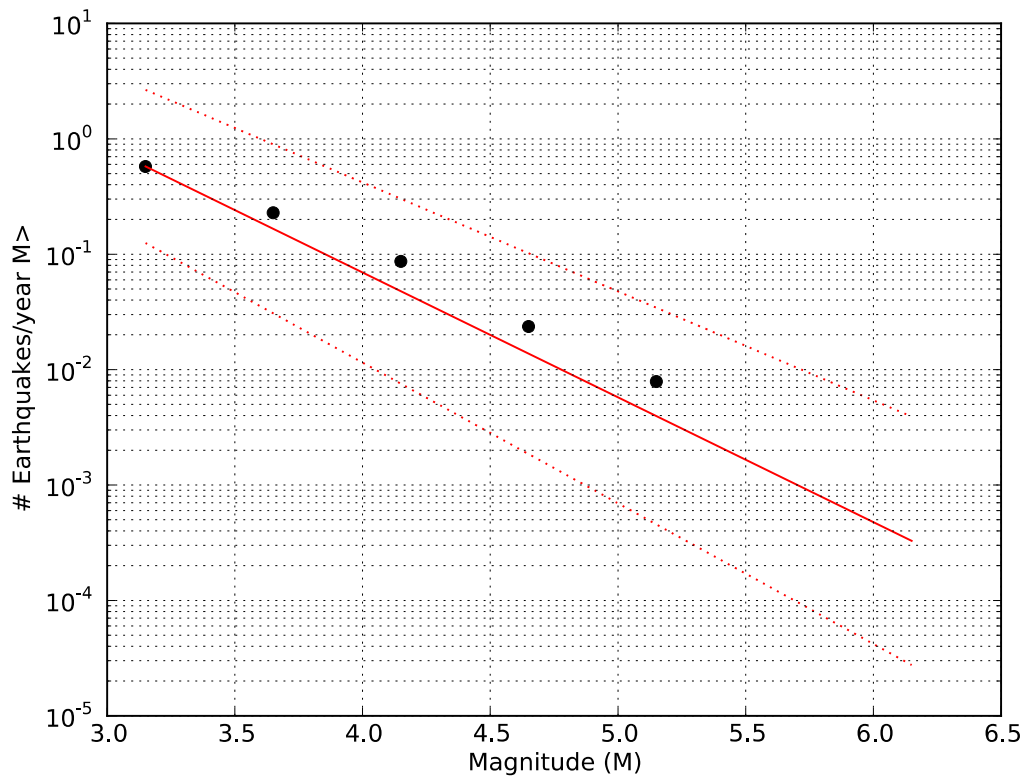


Figure 5.9 – Gutenberg-Richter relationship for the time period 1882-2008 de-clustered catalog determined using the correction for catalog completeness (Weichert, 1980), where $b=1.082\pm 0.138$, and $a=3.167\pm 0.230$.

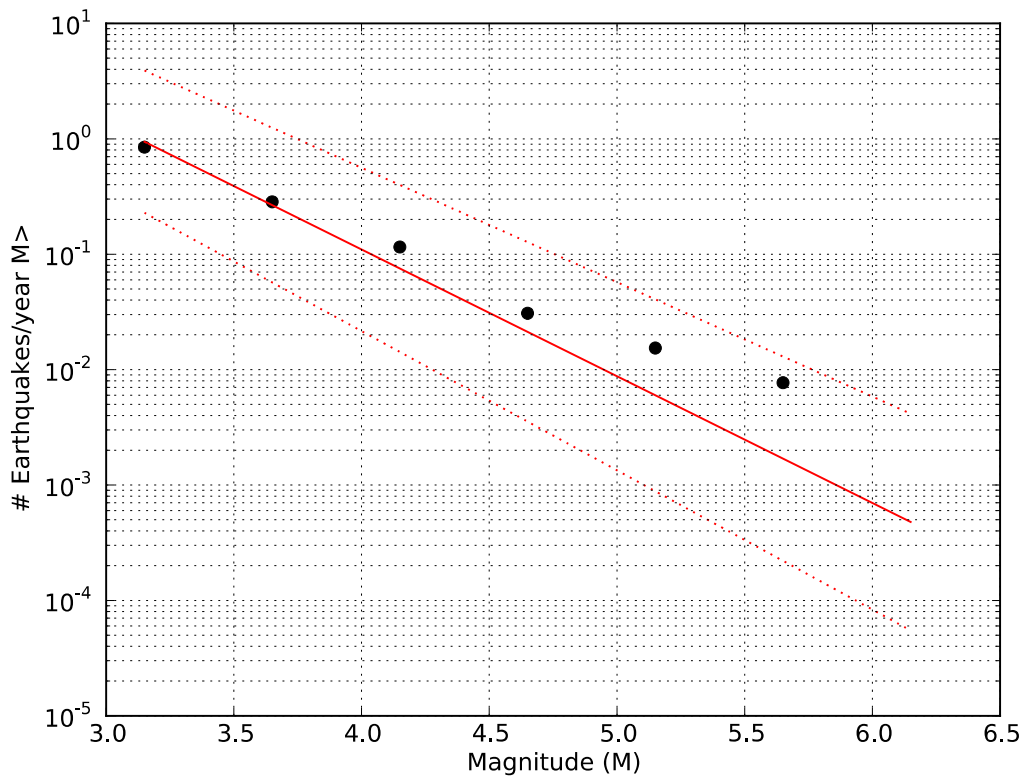


Figure 5.10 – Gutenberg-Richter relationship for the time period 1882-2011 de-clustered catalog determined using the correction for catalog completeness (Weichert, 1980), where $b=1.099\pm 0.108$ and $a=3.436\pm 0.277$.

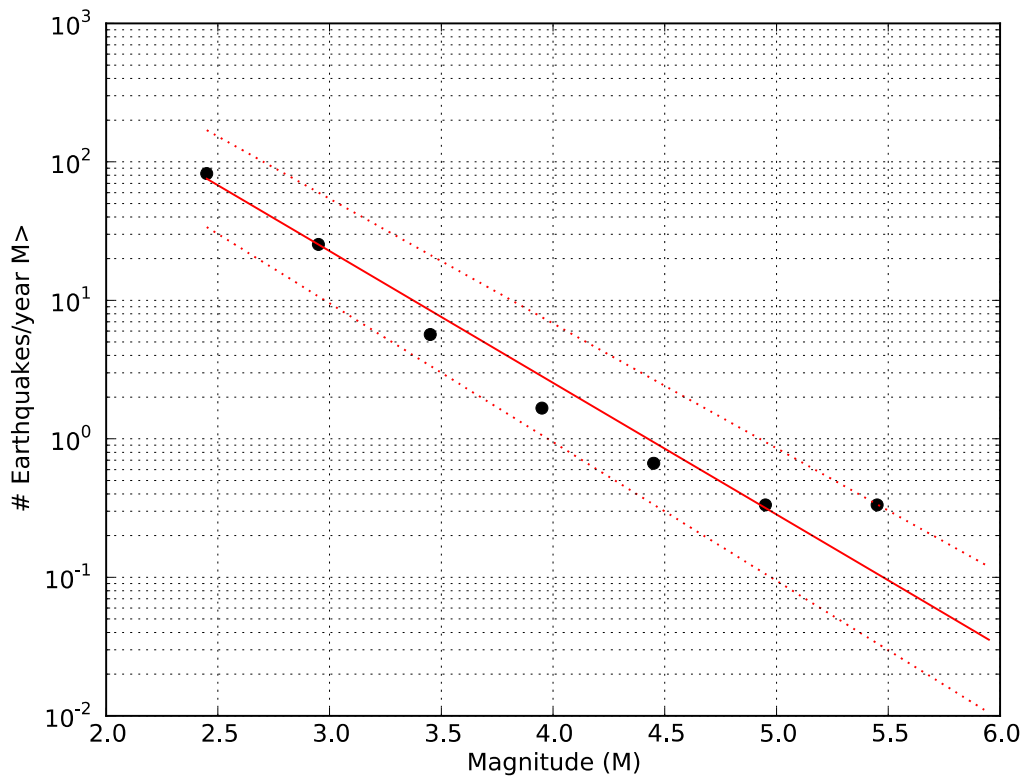


Figure 5.11 – Gutenberg-Richter relationship for the time period 2009-2011 de-clustered catalog determined using the maximum likelihood estimator for b-value (Bender, 1983), where $b=0.951\pm0.051$ and $a=4.21\pm0.226$.

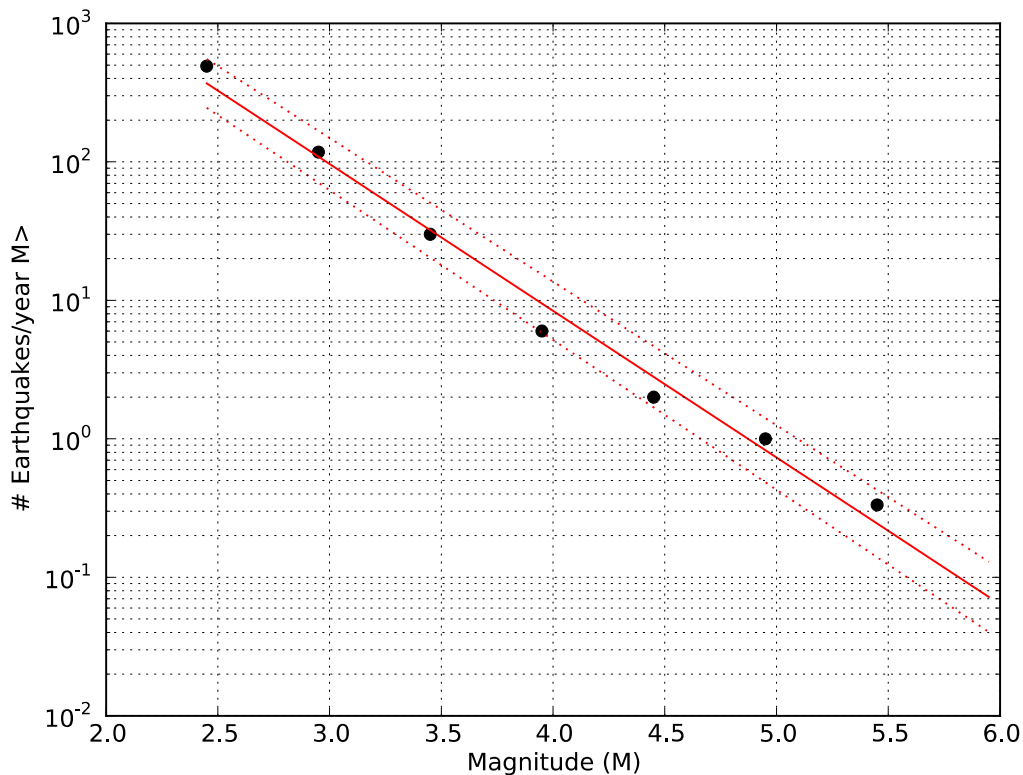


Figure 5.12 – Gutenberg-Richter relationship for the time period 2009-2011 complete catalog determined using the maximum likelihood estimator for b-value (Bender, 1983), where $b=1.06\pm 0.022$ and $a=5.163\pm 0.122$.

6 Vs30 Method and Results

Site-specific Vs30 measurements were obtained for locations that are representative of the accelerometer location at Arcadia Dam Office and the Arcadia Dam. Vs30 is used to classify soils at a site and has a large impact on the site amplification as described by Dobry et al. (2000). Soil classifications determined from Vs30 measurements have a significant impact on observed ground-motions and the estimation of potential ground motions from PSHA. Determined Vs30 values will be used as two different end members in the PSHA assessments.

6.1 Field Methods

Several active-source Multichannel Analysis of Surface Wave (MASW) studies were performed across two locations near Arcadia Lake (Park et al., 1999). The first location was an east-west survey located at 35.6525° N, 97.3709° W, near an accelerometer (ADOK) that is part of the Oklahoma Geological Survey's Seismic Monitoring Network (Figure 6.1). The second was a north-south survey located approximately 200 m east of Arcadia Dam (Figure 6.2).

All surveys used identical instrumentation and receiver geometry. A 24-channel Geometrics geode monitored 4.5 Hz geophones on every channel. Geophones were spaced 2.5 m

apart along a line for a total survey length of 57.5 m. Two source locations were used in each survey. The source consisted of a 12 lb. sledgehammer striking a metal baseplate. Source locations were on the trend of the line, but the distance between the source and the nearest geophone was varied between 10 m and 20 m. Care was taken to minimize noise by not triggering while moving vehicles were nearby or when gusty winds were present.

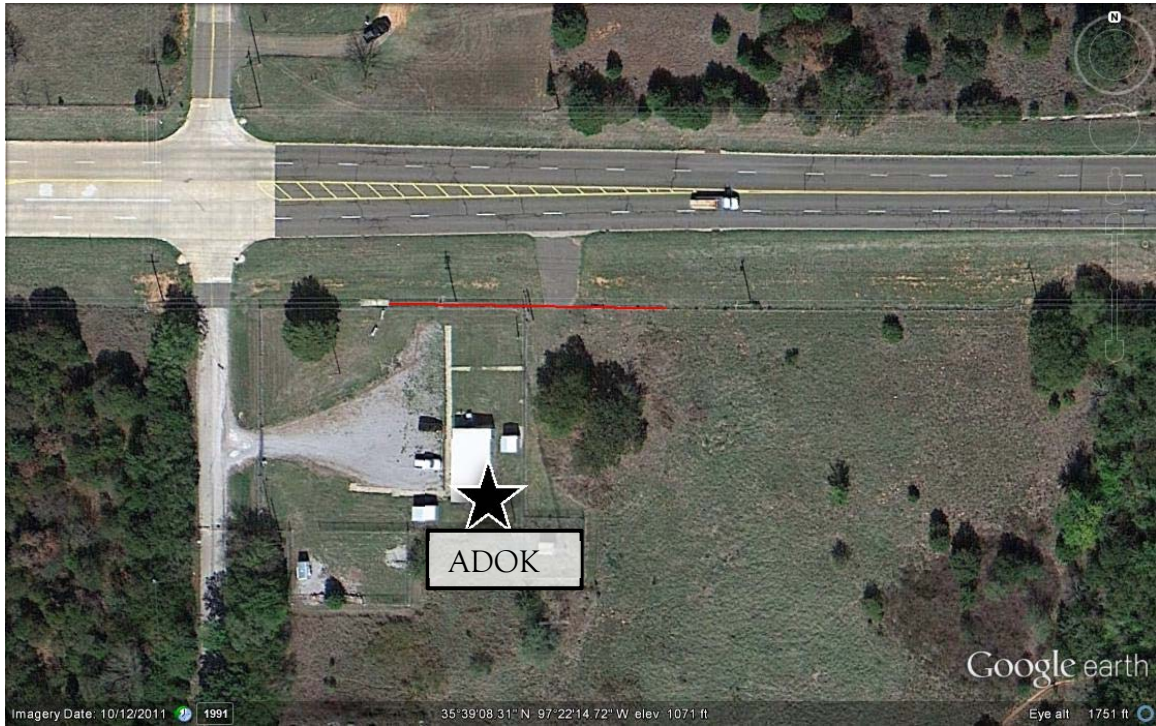


Figure 6.1 - Location of 57.5 m ADOK MASW survey by OGS seismic monitoring station, depicted by the red line. The shown intersection is of Old Route 66/Edmond Rd and S. Douglas Blvd in Edmond, OK. The building is the Army Corps of Engineers Arcadia Dam facility. Image courtesy of Google Earth.



Figure 6.2 - Location of 57.5m Arcadia Dam MASW survey directly east of Arcadia Dam, depicted by the red line. The edge of Lake Arcadia is shown on the western edge of the picture, and the spillway is shown to the north and east of the survey line. Image courtesy of Google Earth.

Three source parameters were varied: 1) minimum source-receiver offset; 2) baseplate restraint, and 3) trace stacking. The minimum source-receiver offset, was varied between either 10 m or 20 m. The second parameter, baseplate restraint, was sometimes used to prevent the baseplate from bouncing after impact. The final parameter, trace stacking, was used to increase the signal-to-noise ratio.

The geode was set up and monitored with Geometric’s Seismodule Controller. The sample rate was .5 ms and the record length was 2 s. An accelerometer was attached to the sledgehammer and connected to the geode such that upon impact the accelerometer would trigger the geode to record.

6.2 Data Analysis

Geometric’s SeisImager was used for the analysis of the recorded surface waves. For both studied locations, one survey was picked that best resolved higher frequencies and another survey was picked that best resolved lower frequencies. As reported by Park et al (1999) and observed in some our data, near-field interference was stronger in lower frequencies and far-field interference at higher frequencies. For this reason, the higher phase velocities at the 12 geophones closest to the source were analyzed. Lower phase velocities were determined from the data recorded on the 12 furthest geophones from the source. Table 6.1 summarizes the surveys used in the analysis in terms of the frequency content and the source parameters. For each of the four surveys, a dispersion curve was generated to show the coherence of the different frequencies in the source signal as a

function of phase velocity (Figures 6.3-6.6). The best-fit phase velocities were picked where they were defined.

Table 6.1 - Description of surveys used in this study.

Survey Location	Frequencies Used	Source Parameters
ADOK	7 Hz - 30 Hz	3 traces stacked, 20 m offset, unrestrained baseplate
ADOK	13 Hz - 50 Hz	3 traces stacked, 10 m offset, unrestrained baseplate
Arcadia Dam	4 Hz - 31 Hz	3 traces stacked, 20 m offset, unrestrained baseplate
Arcadia Dam	6 Hz - 50 Hz	3 traces stacked, 20 m offset, restrained baseplate

Both locations had a survey that better resolved phase velocities for lower frequencies and another that was better resolved for higher frequencies. The two phase velocity picks for each location were merged. The pick files for dispersion curves were merged into a single pick file for each location. The ADOK values were averaged without generating any discontinuities in the dispersion plot (Figure 6.7). The higher frequency phase velocity data at the Arcadia Dam had phase velocities consistently 10 m/s faster than the survey, which resolved lower frequency phase velocities. These two were not averaged because the averaging generated a distinct low velocity zone. The dispersion plot for the Arcadia Dam site (Figure 6.8) did not average the two surveys prior to inversion of the velocity model, but were input directly into the velocity model inversion.

6.3 Results

Final shear wave velocity models to a depth of 30 m are shown in Figures 6.9 and 6.10 for ADOK and Arcadia Dam, respectively. The final average V_{s30} for ADOK was determined to be 621 m/s with an RMS error of 26 m/s after 5 inversion iterations. However, Arcadia Dam yielded a much slower velocity profile, which has an average velocity of 280.8 m/s with an RMS error of 7.6 m/s after the same number of iterations. It remains to be determined whether the 280 m/s velocity actually represents velocities on which the Dam is constructed or simply backfill that does not represent the conditions beneath the Dam.

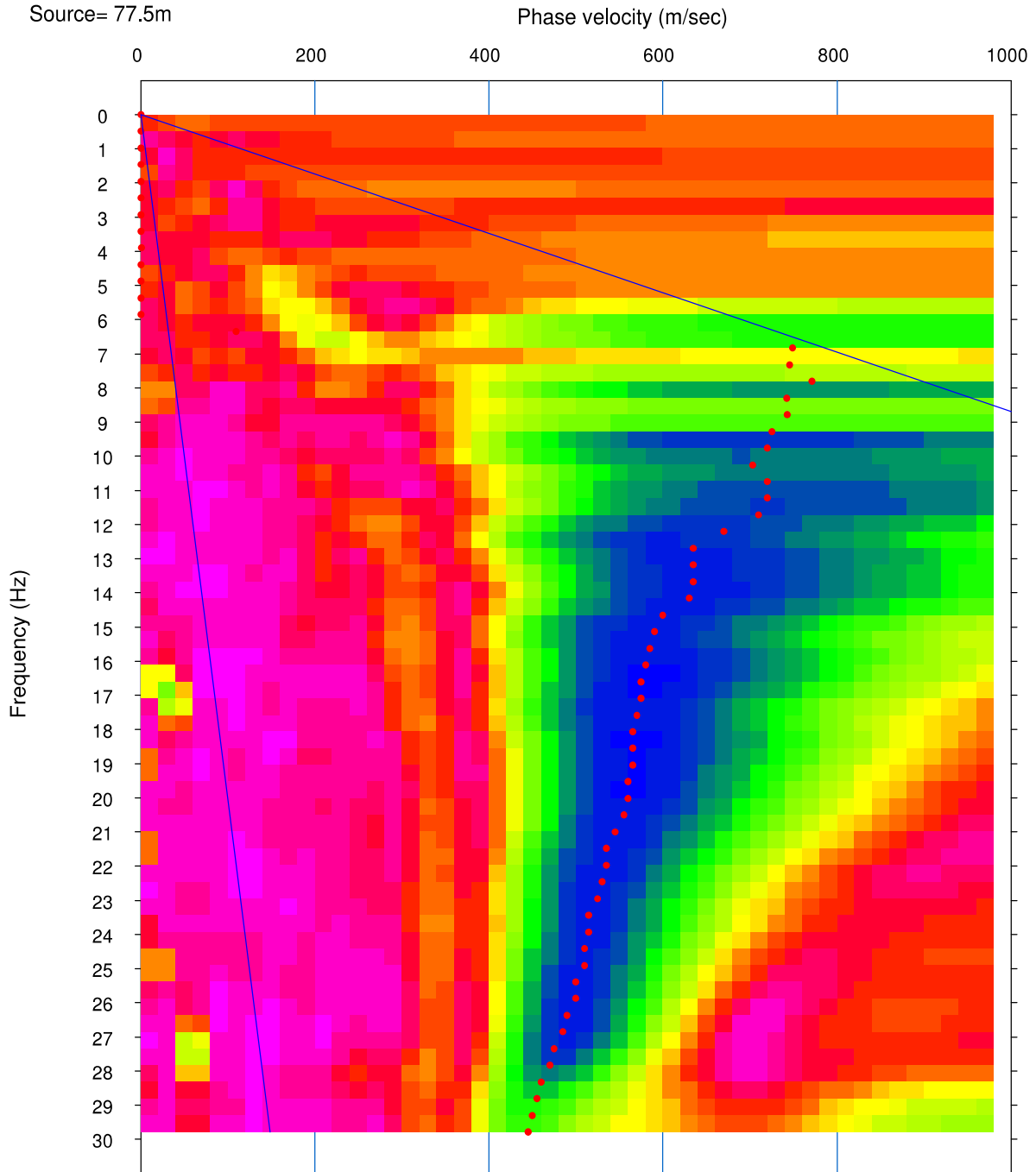


Figure 6.3 - Dispersion curve of ADOK long source offset MASW survey. Blue regions indicated better correlations of phase velocity to the observed frequency dispersion. Phase velocities could only be analyzed down to 7 Hz and lower frequencies were unresolvable.

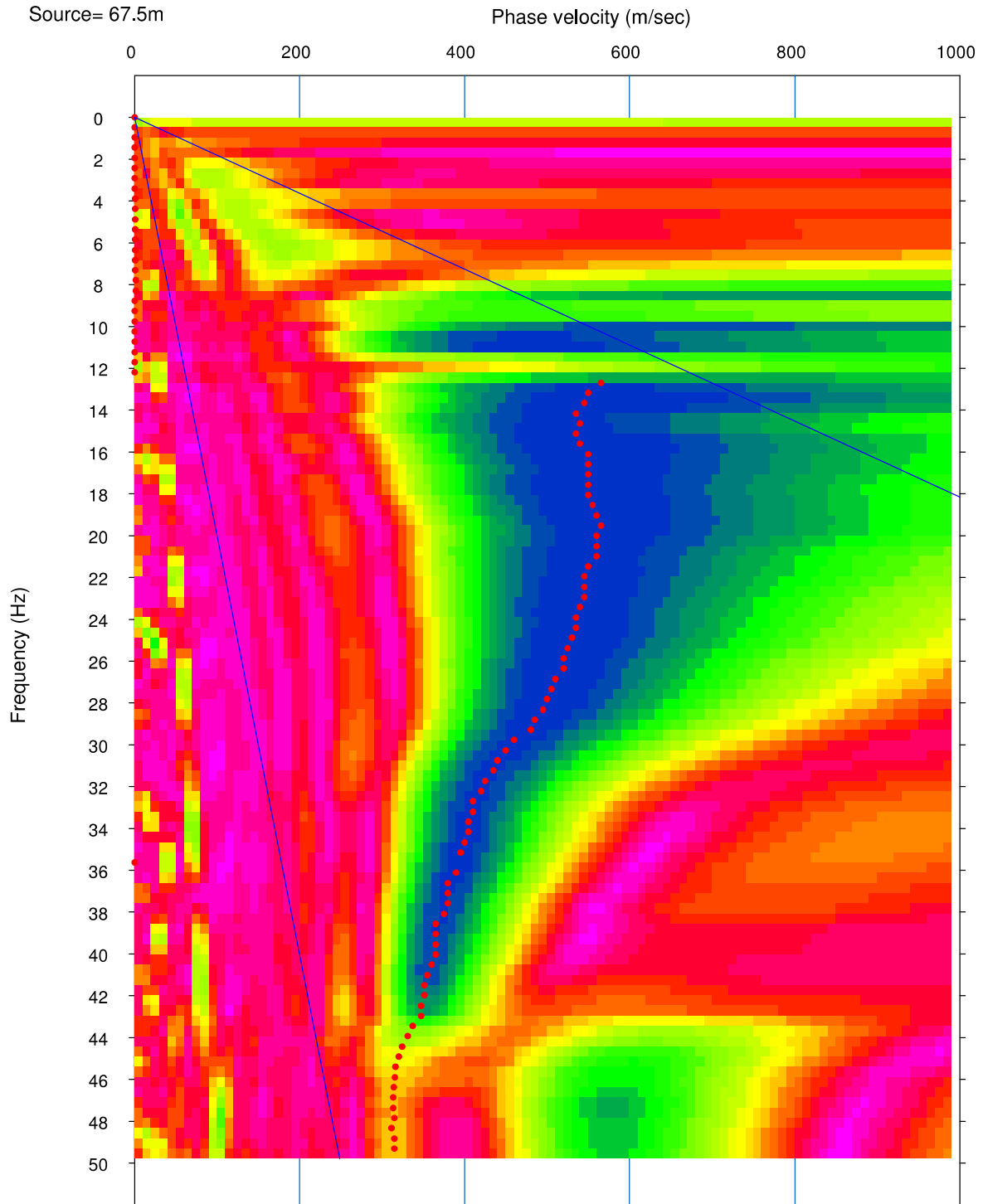


Figure 6.4 - Dispersion curve of ADOK short source offset MASW survey. Blue regions indicated better correlations of phase velocity to the observed frequency dispersion. Phase velocities could only be analyzed down to 13 Hz and most lower frequencies were unresolvable.

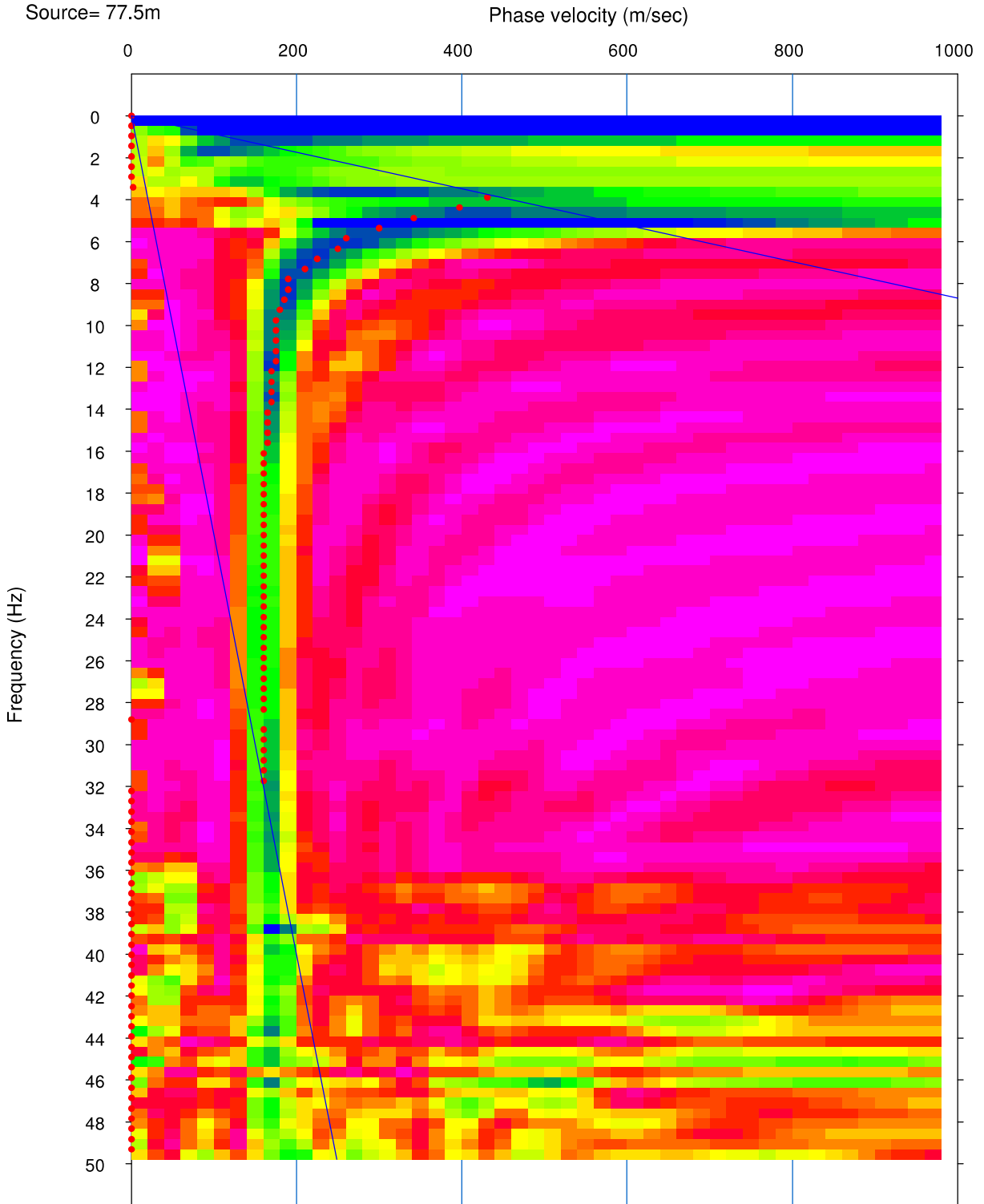


Figure 6.5 - Dispersion curve of Arcadia Dam long offset MASW survey. Blue regions indicated better correlations of phase velocity to the observed frequency dispersion. Phase velocities could be analyzed down to 4 Hz.

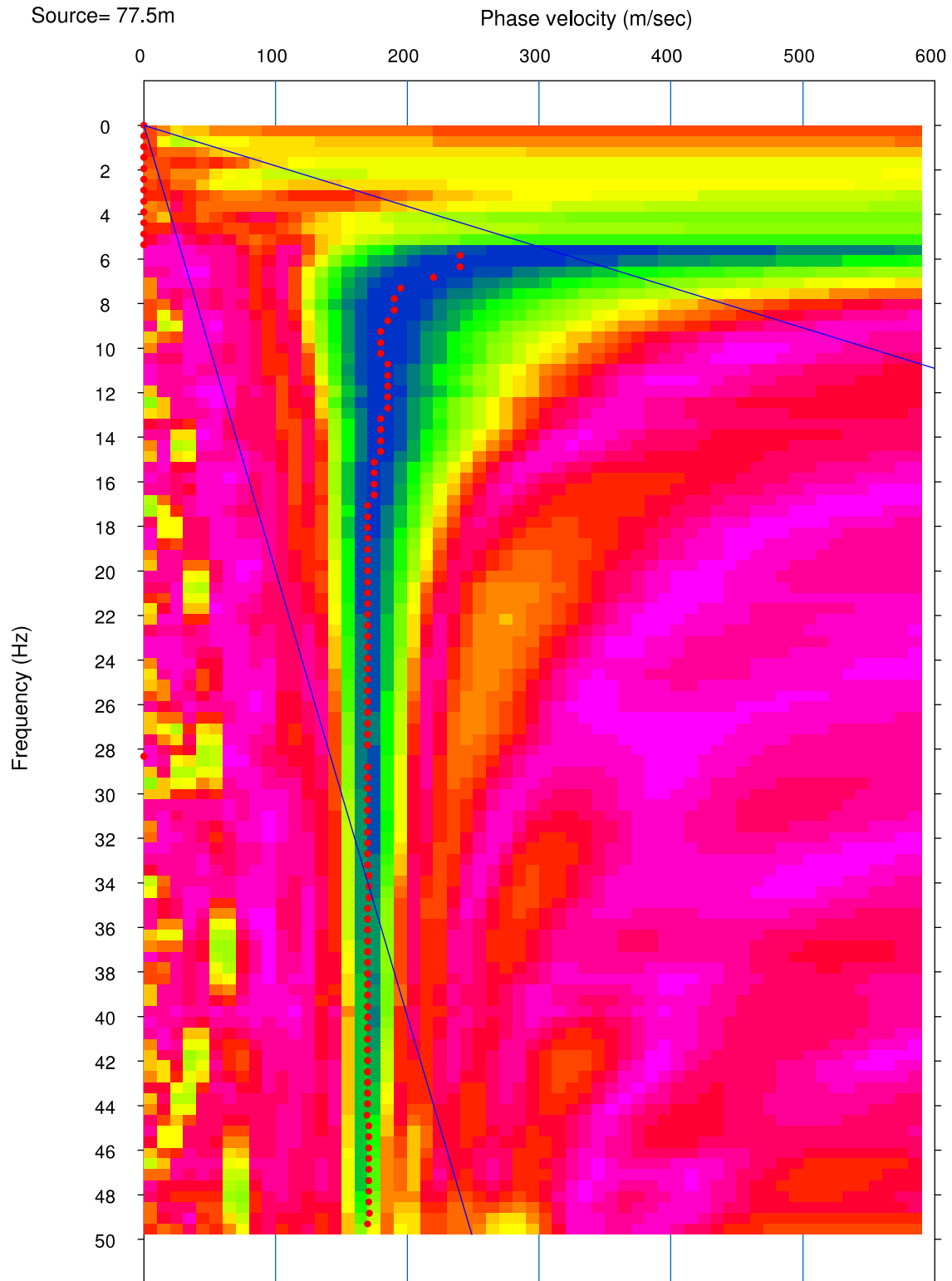


Figure 6.6 - Dispersion curve of Anasazi Dam long offset MASW survey. Blue regions indicated better correlations of phase velocity to the observed frequency dispersion. Phase velocities could be analyzed between 6 Hz to 50 Hz.

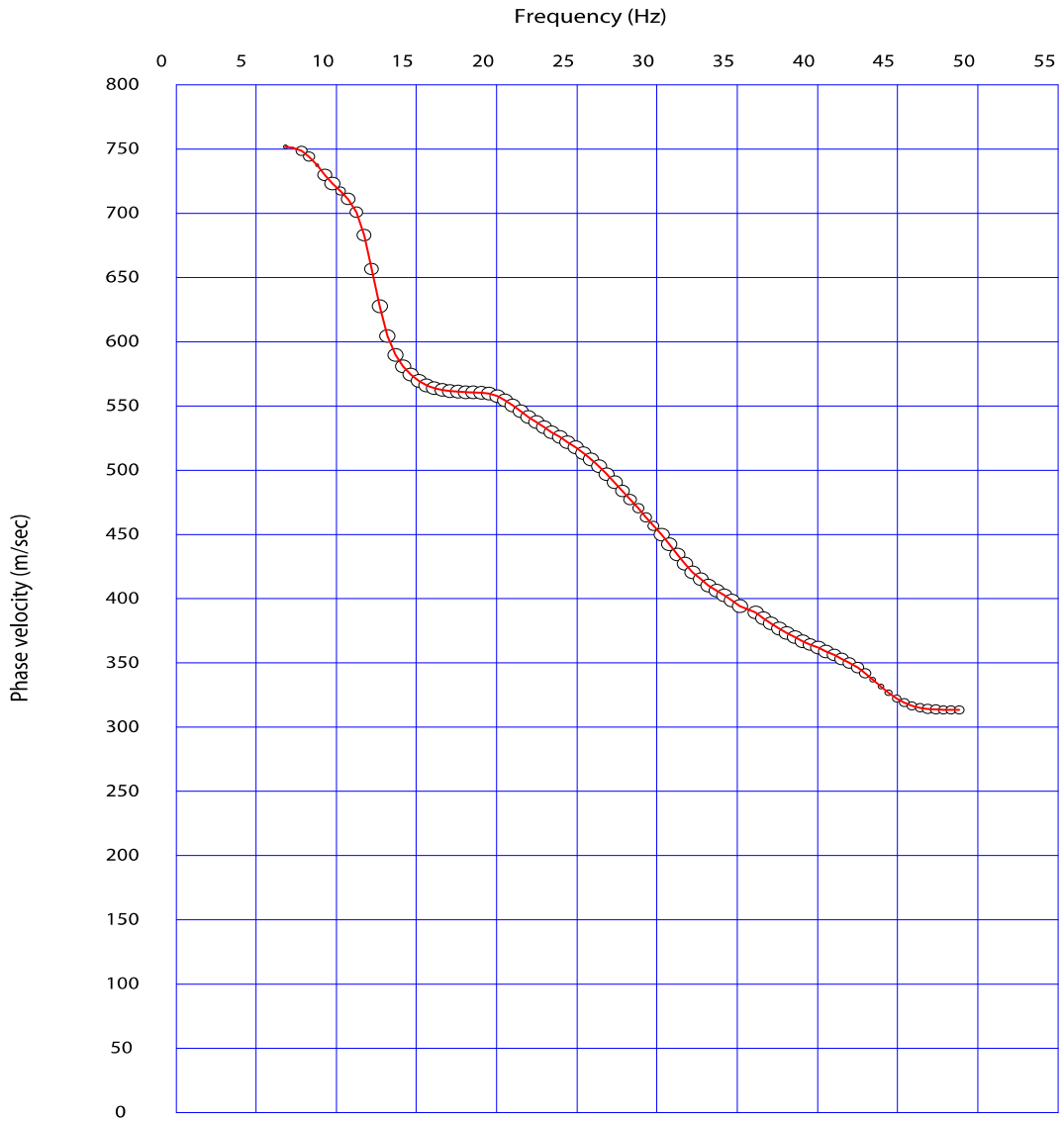


Figure 6.7 - Dispersion plot of ADOK combining the long and short source offset surveys with overlapping values averaged. Overlapping values occurred between in the range of 10 to 30 Hz.

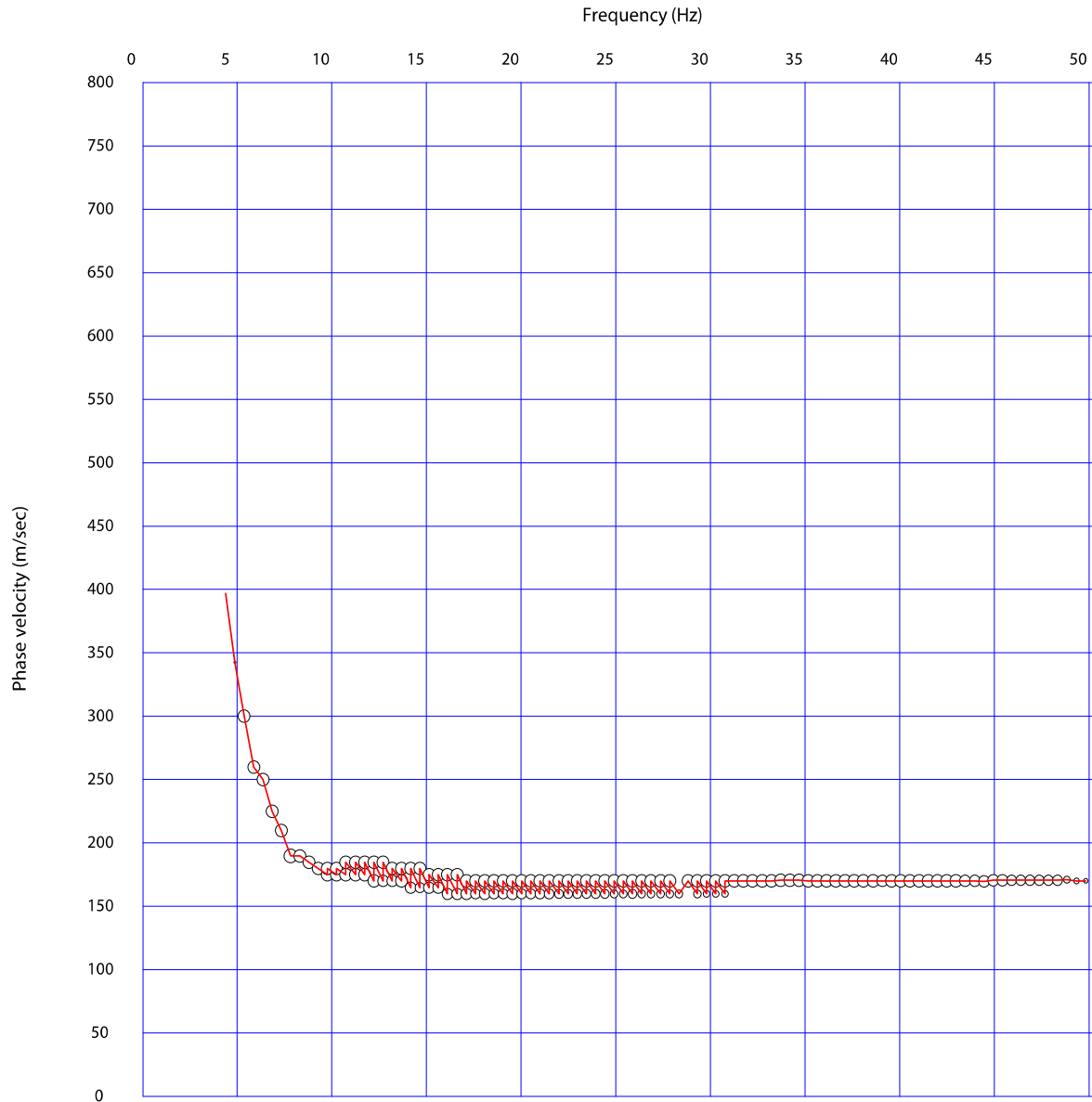


Figure 6.8 - Dispersion plot of Arcadia Dam combining the two long source offset surveys. Overlapping phase velocities were not averaged, creating a sawtooth appearance in the dispersion plot.

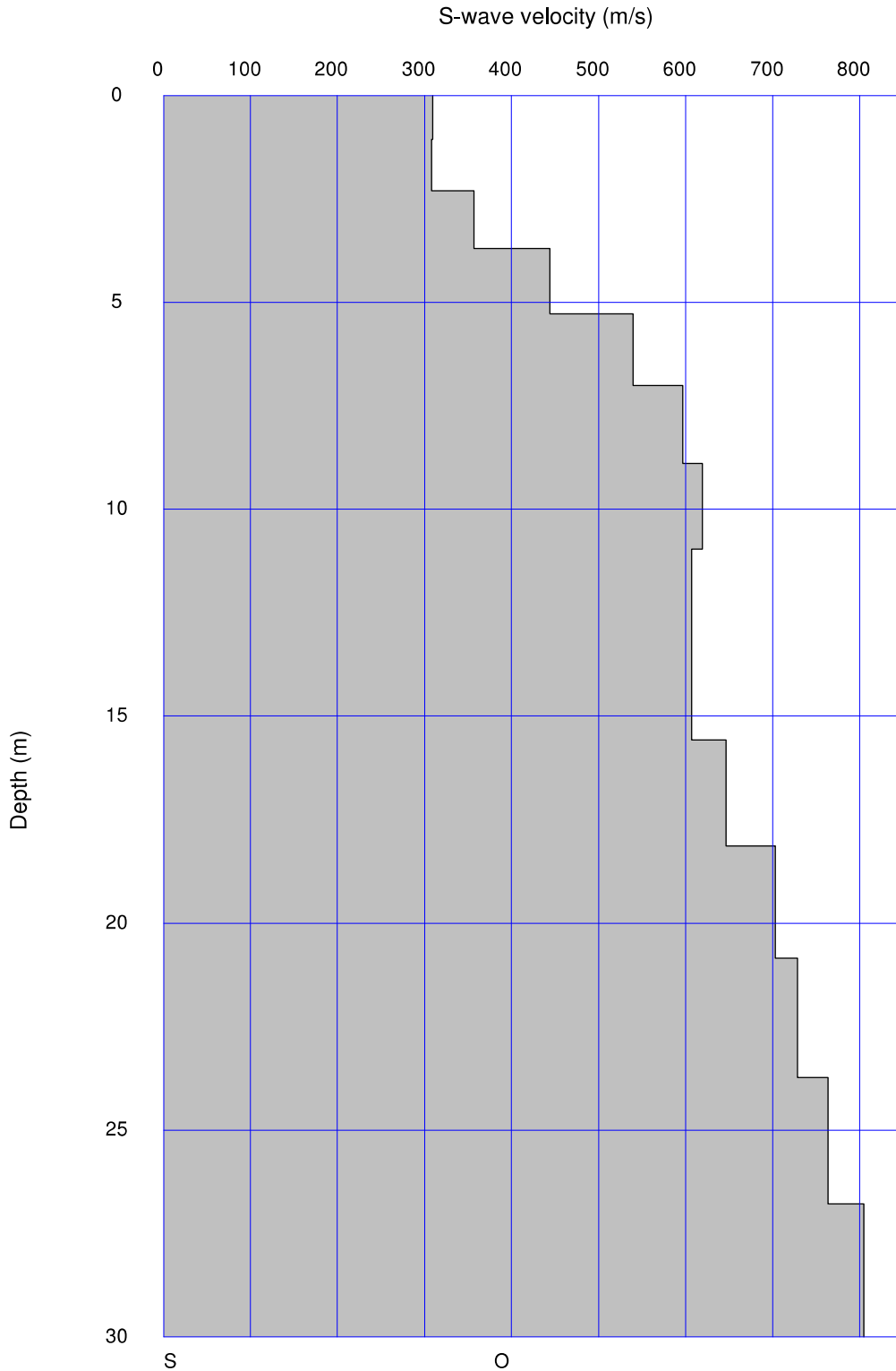


Figure 6.9 - Shear-wave velocity model down to 30 m for ADOK. This model is the result of inversion with 5 iterations. The RMS error of the model was reduced from 49.1 m/sec to 34.1 m/sec during the inversion.

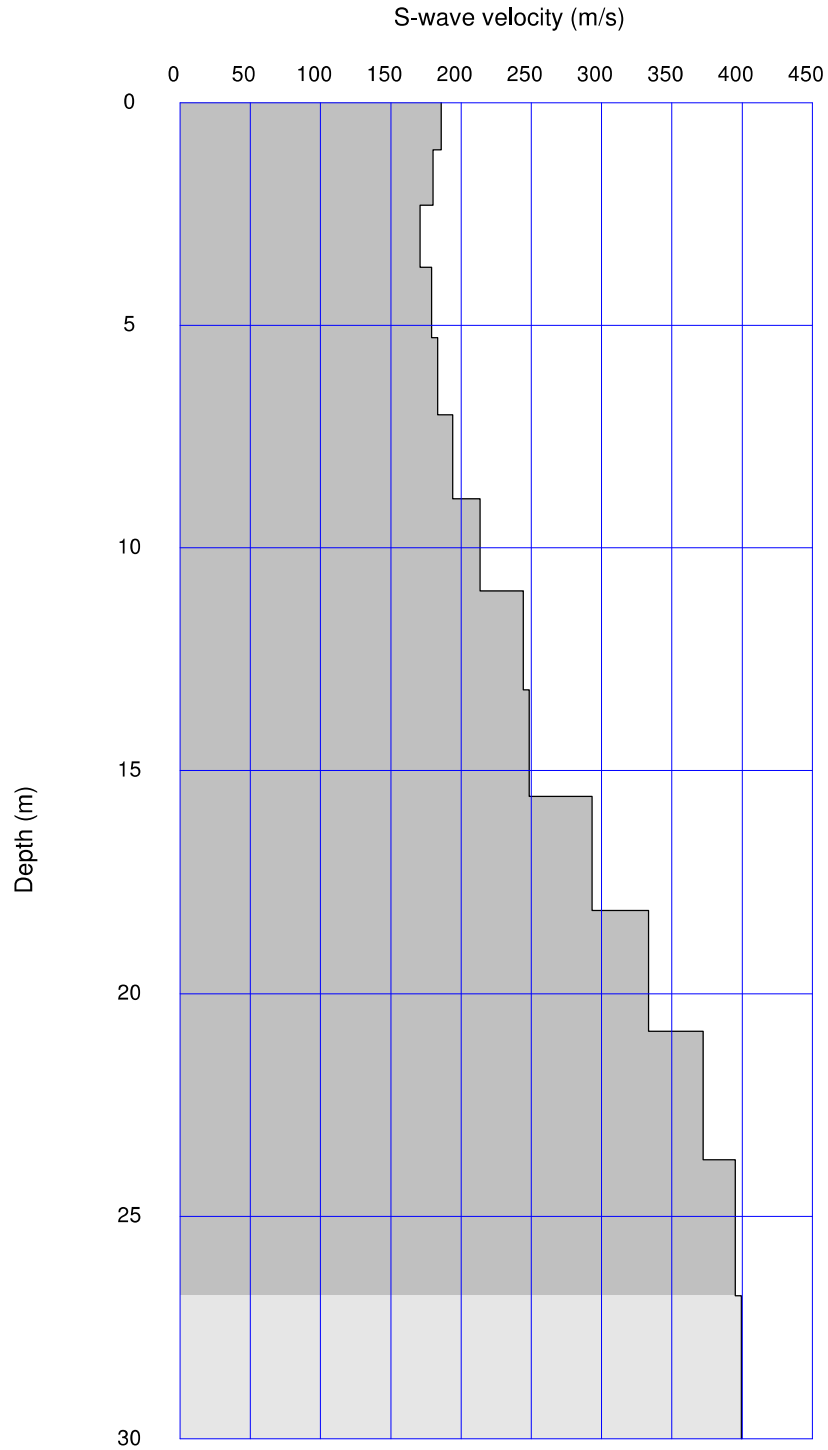


Figure 6.10 - Shear-wave velocity model down to 30 m for Arcadia Dam. This model is the result of inversion with 5 iterations. The RMS error of the model was reduced from 49.1 m/sec to 34.1 m/sec during the inversion.

7 Ground Motion Measurements and Site Amplification

The ground motion from an earthquake can be inferred from seismological records by several empirical models also known as ground motion prediction equations (Abrahamson and Silva, 2008; Atkinson, 2004; Boore and Atkinson, 2008; Campbell, 2003; Campbell and Bozorgnia, 2008; Chiou and Youngs, 2008). The primary factors in these types of estimation are typically epicentral peak ground motion and distance of the earthquake from the location of interest. However, local geologic conditions can increase or decrease the amplitudes of different frequencies of the actual ground motions from what these models would predict – an effect referred to as site amplification.

The purpose of this study is two fold: 1) to determine the site amplification of ADOK, and 2) to estimate the largest earthquake-induced ground motions experienced at this site. Since the epicenter of the largest recorded earthquake in Oklahoma, the M5.6 earthquake that occurred in Prague, OK on November 6, 2011, is less than 60km away from ADOK, we use a ground motion model and site amplification to estimate peak spectral amplitudes at ADOK. Ground acceleration is most closely linked to structural response (Newmark and Hall, 1982). For this reason spectral acceleration amplitudes, specifically at 0.3Hz, 1Hz, 3Hz, and 10Hz, are the focus of our investigation.

7.1 Method

For this study, we used accelerometer records from a seismic monitoring station near Arcadia Dam (herein referred to as ADOK) which is a collaborative station between the OGS and the U.S. Geological Survey, and the EarthScope Transportable Array (TA) seismic stations. Additional OGS stations were not considered because the M5.6 earthquake produced ground motions that exceeded the range of motion the instruments at most of the OGS stations. The time during which the seismograph at ADOK was active is completely bracketed by the occupation of the TA within the region.

Earthquake source parameters scale with magnitude (Kanamori and Anderson, 1975). An analysis that considered earthquakes of too low a magnitude would not be representative of the style of earthquake most pertinent in the analysis of earthquake hazard. However, higher magnitude earthquakes are rare in this region. A compromise was found between having a large enough sample size and not using earthquakes with non-representative source spectra. A cutoff magnitude of 3.0 was chosen. This yielded 153 earthquakes, 18 of which were recorded by ADOK, and all of which were included in this study for the estimation of site amplifications.

Using SeisAn (Havskov and Ottemoller, 1999), origin times and locations for 153 earthquakes between January 14th, 2012 and August 18th were determined by manually picking the arrival times of P- and S-waves. Earthquakes that occurred as part of the Prague sequence from February 2010 through March 2012 were relocated by (Toth et al., 2012). These locations are considered to be more accurate than those calculated with SeisAn. The more accurate hypocenters were refined using the HypoDD double differencing algorithm (Waldhauser and Ellsworth, 2000). Figure 7.1 shows the location of the seismic stations and earthquakes.

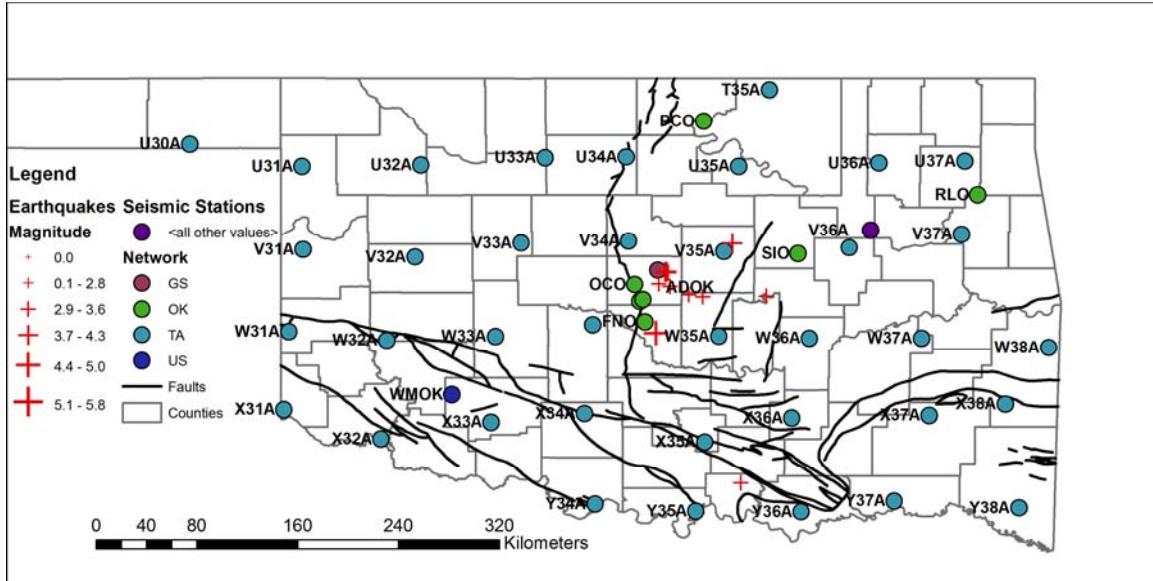


Figure 7.1 - Location of seismic stations (circles) with station identification codes within Oklahoma. The ground motion study stations are coded by network where GS and US are USGS stations, OK are OGS seismic stations, and TA are Earthscope Transportable Array stations. Earthquakes observed at ADOK and used for ground-motion calculations (Figure 7.3) at ADOK are shown as red crosses scaled by magnitude. Faults (Northcutt and Campbell, 1995) are shown as thick black lines.

7.2 Conversion from Instrumental Records to Ground Motion Records

Seismological records represent a convolution of ground motion with several factors, both instrumental and geologic in origin. The recorded ground motion at a site can be described by the following equation:

$$S(f) = A(f) * I(f) * R(f) * B(f) \quad (7.1)$$

where $S(f)$ is the recorded ground motion, $A(f)$ is the source contribution, $I(f)$ is the instrument's response and phase distortion, $R(f)$ is the site response, and $B(f)$ is the attenuation (Scherbaum, 2007).

The information required to remove instrument response and phase distortion are represented by the format specified in the Standard for the Exchange of Earthquake Data, or SEED for short (FDSN, 2012). The ObsPy python libraries (Beyreuther et al., 2010) contain subroutines that read SEED response files and were used to remove these instrumental and recording artifacts. Fundamentally, this removal of $I(f)$ was implemented by a deconvolution in the frequency domain. Long-period signals (i.e. microseismic signal, instrument drift, and filtering artifacts) were also removed from the data using a zero-phase highpass filter with a cutoff frequency of 0.1Hz. The filtering and recording processes result in phase shifting of the data. Phase shifts did not affect spectral acceleration amplitudes of individual frequencies

7.3 TA and ADOK Site Amplification Factors

Site amplification $R(f)$ in equation 7.1 is the deviation in observed ground motion intensity from the theoretical ground motion intensity. To determine site amplification $R(f)$, both the

source spectrum $A(f)$ and attenuation spectrum $B(f)$ are needed. The determination of a regional attenuation model, and thus $B(f)$, is outside the scope of this work. However, previous models demonstrate that Central United States (CUS) and Eastern North America (ENA) have similar source spectra and attenuation characteristics (Atkinson, 1993; Dangkoa and Cramer, 2011). Therefore, we used the (Atkinson, 2004) empirical attenuation model for spectral acceleration in ENA as our attenuation model.

To estimate $A(f)$ we used one attenuation model for ENA (Atkinson, 2004) to remove the effects of attenuation from the seismographs with the following equations:

for $R < 70$ km:

$$\log A_0 = \log A + 1.3 \log R + c_4 R - \log \text{residual}(h) \quad (7.2)$$

for $70 < R < 140$ km:

$$\log A_0 = \log A + 1.3 \log 70 - 0.2 \log\left(\frac{R}{70}\right) + c_4 R - \log \text{residual}(h) \quad (7.3)$$

for $R > 140$ km:

$$\log A_0 = \log A + 1.3 \log 70 - 0.2 \log\left(\frac{140}{70}\right) + 0.5 \log\left(\frac{R}{140}\right) + c_4 R - \log \text{residual}(h) \quad (7.4)$$

Here, A_0 is the source spectral amplitude, A is the observed spectral amplitude at some distance, R is the distance from the epicenter, c_4 is a frequency-dependent anelastic coefficient. The $\text{residual}(h)$ is the focal depth regression residual given by:

$$\log \text{residual}(h) = d_1(h - 10) \log R + d_2 \quad (7.5)$$

where h is the focal depth and d_1 and d_2 are unit-less frequency-dependent regression residuals. The frequency dependent coefficients d_1 , d_2 , and c_4 , are summarized in table 1 below for the frequencies analyzed in this study.

Table 7.1 - Table of frequency dependent coefficients originally presented in Atkinson (2004). Values were not always provided for exactly 0.3, 1, 3, and 10 Hz in the various tables. Where this is the case, the values used in this study and presented here were obtained by linear interpolation with the two nearest provided values.

Frequency (f)	d_1	d_2	c_4
0.3 Hz	0	0	-0.00002 cm/sec
1.0 Hz	0	0	-0.00035 cm/sec
3.0 Hz	0.0022	0.0046	-0.00092 cm/sec
10.0 Hz	0.0052	-0.021	-0.00204 cm/sec

A value for $\log(A_0)$ is generated for every seismogram for every earthquake. For each earthquake, all the $\log(A_0)$ values are averaged to find an estimate for the source amplitude at each frequency. The final result is a set of 153 estimates of source amplitudes at 0.3, 1, 3, and 10 Hz,

which approximate $A(f)$. Following the estimation of $A(f)$, equations 7.2-7.4 were solved for $\log A$ to provide estimates of ground motion at an arbitrary distance R from the epicenter.

for $R < 70$ km:

$$\log A = \log A_0 - 1.3 \log R - c_4 R + \log \text{residual}(h) \quad (7.6)$$

for $70 < R < 140$ km:

$$\log A = \log A_0 - 1.3 \log 70 + 0.2 \log \left(\frac{R}{70} \right) - c_4 R + \log \text{residual}(h) \quad (7.7)$$

for $R > 140$ km:

$$\log A = \log A_0 - 1.3 \log 70 + 0.2 \log \left(\frac{140}{70} \right) - 0.5 \log \left(\frac{R}{140} \right) - c_4 R + \log \text{residual}(h) \quad (7.8)$$

For each of the 153 approximations of $A(f)$, equations 7.6-7.8 were used to generate estimates for what the expected spectral accelerates at every seismograph that recorded that earthquake. Using the following equation, a site amplification factor was generated for every seismograph during every earthquake:

$$SA = \frac{A_{obs}}{A_{est}} \quad (7.9)$$

where SA is the site amplification factor, A_{obs} is the observed spectral acceleration obtained from the removal of $I(f)$ from $S(f)$, and A_{est} is the estimated spectral acceleration as calculated by equations 7.6-7.8 from $A(f)$ and $B(f)$. Since site amplifications are logarithmically scaled, an average and standard deviation of $\log(SA)$ is calculated at every station (Tables 7.2 and 7.3)

Occasionally, calculated site amplification for an individual event was anomalously low or high. Possible reasons for this include large vehicles driving near the seismometer; strong thunder; nearby construction work; etc. Consequently, the data is occasionally contaminated by strong noise, leading to site amplifications as much as several orders of magnitude greater than the average site amplification recorded at that site. Rather than manually reviewing $\sim 10,000$ seismic records to determine where this might be the case, we exclude site amplifications greater than 30. Likewise, instrumental and network errors sometimes result in seismic records that don't record the strongest portions of the earthquake. Site amplifications less than .03 were also excluded from the analysis.

7.4 M5.6 Epicentral and ADOK Spectral Acceleration

A M5.6 earthquake occurred near Prague, OK on November 5th, 2011. The ground motions generated by this event were the largest recorded ground motions in the State of Oklahoma. ADOK is located approximately 60 km WNW of the M5.6 earthquake and the ground motions generated at ADOK by this event are greater than those generated at ADOK by any other recorded earthquake.

For the M5.6 earthquake, peak spectral ground motions at every active seismograph were calculated following the above procedure. The data were appropriately scaled with their corresponding site amplifications from Tables 7.2 and 7.3. Following the procedure described

above, the peak epicentral spectral acceleration amplitudes for $f=0.3, 1, 3,$ and 10 Hz were calculated using equations 7.2-7.4. Finally, equations 7.6-7.8 were used to estimate the spectral acceleration intensities at ADOK, and these intensities were appropriately scaled by the ADOK site amplifications to arrive at the peak ground acceleration, which is displayed in Table 7.4.

7.5 Results

The site amplifications determined in this study for ADOK and the TA stations are shown in Table 7.2 for vertical components and Table 7.3 for horizontal components. Site amplifications have a logarithmic distribution, so to best represent these values for ADOK and the Oklahoma TA stations the average of the \log_{10} of the site amplifications is reported in Tables 7.2 and 7.3. Furthermore, given the skew in a linear plot of the site amplifications (Figure 7.2), the standard deviation of the logarithms of the site amplifications are also presented.

Even though of all the stations ADOK had the greatest variation in site amplification, no correlation between site amplification and epicentral distance or azimuth was apparent in the data (Figure 7.2). The ground motions experienced at ADOK for the 18 events it recorded are displayed in Figure 7.3. The distance and azimuth from the source, as well as the magnitude, varied from event to event.

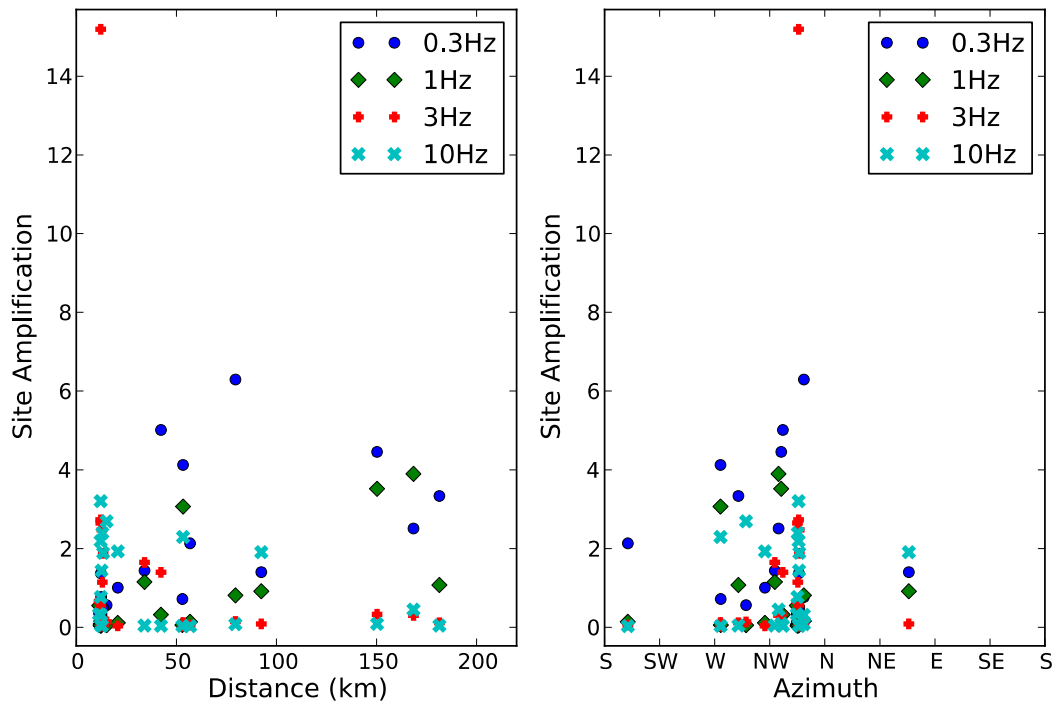


Figure 7.2 - vertical site amplifications at ADOK for individual events, plotted against: a.) Distance from the epicenter to ADOK, and b.) Azimuth from the epicenter to ADOK. The linear scale shows positive skew in the data. Because no correlation between site amplification, distance and azimuth was apparent, variation in individual site amplifications is likely due to source characteristics.

Table 7.2 Vertical site amplifications and standard deviations, values are expressed as the average of the log10 site amplifications plus/minus one standard deviation.

Station	Base 10 Logarithm of Vertical Site Amplification			
	0.3 Hz	1 Hz	3 Hz	10 Hz
ADOK	-0.0 ± 0.54	-0.5 ± 0.62	-0.4 ± 0.73	-0.4 ± 0.76
T35A	-0.2 ± 0.26	-0.1 ± 0.24	0.10 ± 0.31	-0.0 ± 0.30
U30A	0.40 ± 0.24	0.32 ± 0.24	-0.1 ± 0.24	-0.0 ± 0.21
U31A	0.25 ± 0.26	0.29 ± 0.16	0.08 ± 0.37	-0.3 ± 0.33
U32A	0.16 ± 0.29	0.05 ± 0.28	0.09 ± 0.29	-0.0 ± 0.32
U33A	-0.0 ± 0.25	-0.2 ± 0.33	0.01 ± 0.26	0.68 ± 0.23
U34A	-0.1 ± 0.18	-0.2 ± 0.25	-0.0 ± 0.23	0.10 ± 0.22
U35A	-0.4 ± 0.28	-0.2 ± 0.28	-0.2 ± 0.31	-0.0 ± 0.27
U36A	-0.2 ± 0.30	-0.2 ± 0.25	-0.1 ± 0.28	0.09 ± 0.26
V31A	0.28 ± 0.22	0.22 ± 0.27	0.43 ± 0.32	-0.2 ± 0.26
V32A	0.12 ± 0.26	0.01 ± 0.22	0.17 ± 0.23	0.51 ± 0.23
V33A	-0.0 ± 0.28	-0.1 ± 0.16	0.12 ± 0.31	0.22 ± 0.31
V34A	-0.5 ± 0.29	-0.3 ± 0.26	-0.4 ± 0.37	-0.0 ± 0.27
V35A	-0.6 ± 0.28	-0.4 ± 0.35	-0.1 ± 0.30	0.02 ± 0.33
V36A	-0.4 ± 0.28	-0.3 ± 0.30	-0.2 ± 0.27	0.00 ± 0.29
V37A	-0.2 ± 0.30	-0.3 ± 0.21	0.00 ± 0.23	-0.0 ± 0.29
W31A	0.02 ± 0.29	0.06 ± 0.23	-0.1 ± 0.35	0.09 ± 0.31
W32A	-0.1 ± 0.34	0.06 ± 0.30	-0.1 ± 0.25	-0.1 ± 0.21
W33A	0.00 ± 0.17	-0.0 ± 0.26	-0.2 ± 0.20	-0.1 ± 0.23
W34A	-0.2 ± 0.26	-0.1 ± 0.29	-0.3 ± 0.33	-0.0 ± 0.28
W35A	-0.6 ± 0.26	-0.4 ± 0.34	-0.0 ± 0.17	0.01 ± 0.41
W36A	-0.4 ± 0.29	-0.4 ± 0.30	-0.2 ± 0.29	0.01 ± 0.24
W37A	0.06 ± 0.23	-0.0 ± 0.16	-0.2 ± 0.45	-0.1 ± 0.22
W38A	0.33 ± 0.29	0.08 ± 0.28	-0.0 ± 0.26	-0.3 ± 0.29
X31A	0.08 ± 0.30	-0.1 ± 0.38	-0.0 ± 0.24	0.03 ± 0.28
X32A	0.03 ± 0.20	0.04 ± 0.17	0.02 ± 0.27	0.47 ± 0.22
X33A	-0.1 ± 0.26	-0.0 ± 0.30	-0.0 ± 0.18	0.12 ± 0.25
X34A	0.34 ± 0.26	0.19 ± 0.21	0.22 ± 0.27	0.48 ± 0.26
X35A	-0.4 ± 0.25	-0.3 ± 0.34	-0.1 ± 0.31	0.04 ± 0.37
X36A	0.06 ± 0.28	0.04 ± 0.21	-0.1 ± 0.30	0.07 ± 0.25
X37A	0.09 ± 0.29	0.13 ± 0.25	0.03 ± 0.29	-0.2 ± 0.35
X38A	0.11 ± 0.32	0.01 ± 0.23	0.00 ± 0.25	-0.2 ± 0.29
Y34A	-0.2 ± 0.16	-0.2 ± 0.29	-0.1 ± 0.28	-0.1 ± 0.28
Y35A	0.00 ± 0.29	0.06 ± 0.27	-0.2 ± 0.29	-0.3 ± 0.30
Y36A	0.00 ± 0.32	0.22 ± 0.26	0.03 ± 0.32	-0.2 ± 0.27
Y37A	0.08 ± 0.29	0.33 ± 0.28	0.07 ± 0.33	-0.2 ± 0.31
Y38A	0.09 ± 0.30	0.07 ± 0.26	0.10 ± 0.31	-0.3 ± 0.36

Table 7.3 - Horizontal site amplifications and standard deviations, values are expressed as the average of the log10 site amplifications plus/minus one standard deviation.

Station	Base 10 Logarithm of Horizontal Site Amplification			
	0.3 Hz	1 Hz	3 Hz	10 Hz
ADOK	-0.1 ± 0.53	-0.5 ± 0.46	-0.7 ± 0.88	0.09 ± 0.85
T35A	-0.0 ± 0.20	-0.1 ± 0.17	0.11 ± 0.23	-0.0 ± 0.18
U30A	0.27 ± 0.28	0.44 ± 0.27	0.18 ± 0.17	-0.3 ± 0.22
U31A	0.34 ± 0.18	0.29 ± 0.15	-0.0 ± 0.21	-0.1 ± 0.17
U32A	0.27 ± 0.32	0.27 ± 0.20	0.15 ± 0.21	0.07 ± 0.21
U33A	-0.1 ± 0.25	-0.0 ± 0.22	0.03 ± 0.24	0.20 ± 0.18
U34A	-0.1 ± 0.16	-0.2 ± 0.21	-0.0 ± 0.21	0.24 ± 0.19
U35A	-0.2 ± 0.20	-0.2 ± 0.22	-0.0 ± 0.18	0.23 ± 0.18
U36A	-0.2 ± 0.20	-0.2 ± 0.23	-0.1 ± 0.22	0.00 ± 0.19
V31A	0.30 ± 0.22	0.38 ± 0.23	0.47 ± 0.21	-0.3 ± 0.31
V32A	0.16 ± 0.21	0.24 ± 0.18	0.10 ± 0.18	0.06 ± 0.21
V33A	0.03 ± 0.17	0.07 ± 0.22	0.14 ± 0.22	0.30 ± 0.22
V34A	-0.3 ± 0.21	-0.2 ± 0.20	-0.3 ± 0.32	-0.0 ± 0.19
V35A	-0.4 ± 0.30	-0.2 ± 0.26	-0.1 ± 0.23	0.14 ± 0.24
V36A	-0.3 ± 0.25	-0.3 ± 0.22	-0.1 ± 0.20	0.26 ± 0.20
V37A	-0.2 ± 0.23	-0.4 ± 0.23	-0.1 ± 0.17	-0.1 ± 0.23
W31A	0.12 ± 0.25	0.04 ± 0.22	0.15 ± 0.21	-0.1 ± 0.17
W32A	0.08 ± 0.26	-0.0 ± 0.18	0.03 ± 0.19	0.23 ± 0.14
W33A	0.01 ± 0.18	-0.1 ± 0.19	-0.2 ± 0.25	-0.2 ± 0.19
W34A	-0.1 ± 0.20	-0.0 ± 0.20	-0.2 ± 0.23	0.05 ± 0.20
W35A	-0.3 ± 0.24	-0.2 ± 0.26	-0.2 ± 0.25	-0.1 ± 0.21
W36A	-0.2 ± 0.25	-0.2 ± 0.21	-0.2 ± 0.19	0.03 ± 0.18
W37A	-0.0 ± 0.32	-0.1 ± 0.19	0.17 ± 0.26	-0.2 ± 0.20
W38A	0.09 ± 0.19	0.22 ± 0.22	0.01 ± 0.21	0.07 ± 0.22
X31A	0.08 ± 0.25	-0.1 ± 0.16	-0.2 ± 0.28	0.12 ± 0.24
X32A	0.08 ± 0.24	-0.0 ± 0.25	0.06 ± 0.27	0.11 ± 0.21
X33A	-0.2 ± 0.22	-0.0 ± 0.21	0.01 ± 0.15	0.06 ± 0.25
X34A	0.51 ± 0.23	0.27 ± 0.18	0.30 ± 0.18	0.13 ± 0.18
X35A	-0.4 ± 0.19	-0.4 ± 0.27	-0.2 ± 0.20	0.21 ± 0.21
X36A	0.04 ± 0.23	-0.0 ± 0.19	0.14 ± 0.22	0.01 ± 0.19
X37A	0.11 ± 0.25	-0.0 ± 0.28	-0.1 ± 0.33	-0.2 ± 0.38
X38A	0.17 ± 0.23	0.00 ± 0.18	-0.1 ± 0.20	-0.3 ± 0.26
Y34A	-0.1 ± 0.26	0.01 ± 0.32	0.05 ± 0.21	-0.2 ± 0.24
Y35A	0.05 ± 0.20	-0.0 ± 0.16	-0.0 ± 0.18	-0.5 ± 0.20
Y36A	0.05 ± 0.24	0.18 ± 0.17	0.07 ± 0.18	-0.2 ± 0.23
Y37A	0.12 ± 0.21	0.33 ± 0.22	0.13 ± 0.21	-0.2 ± 0.25
Y38A	0.03 ± 0.25	0.32 ± 0.22	0.23 ± 0.27	-0.1 ± 0.24

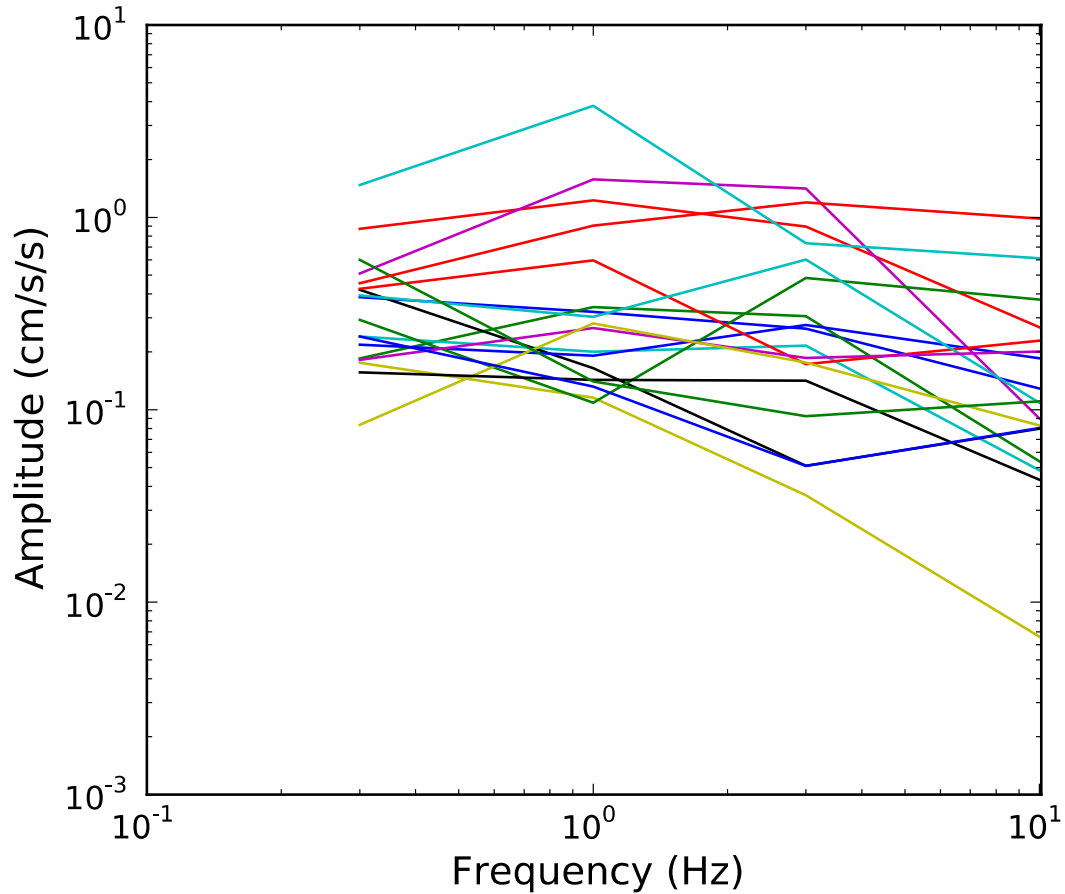


Figure 7.3 - Calculated peak horizontal spectral accelerations experienced at ADOK. Values are derived from the removal of instrument response from the seismogram.

Table 7.4 ADOK peak ground accelerations estimated for the Magnitude 5.6 November 5, 2011 earthquake.

Peak Vertical Acceleration				
Frequency	0.3Hz	1 Hz	3 Hz	10 Hz
Amplitude	56.0 cm/s/s	26.2 cm/s/s	21.5 cm/s/s	14.2 cm/s/s

Peak Horizontal Acceleration				
Frequency	0.3Hz	1 Hz	3 Hz	10 Hz
Amplitude	95.2 cm/s/s	56.4 cm/s/s	34.7 cm/s/s	219.5 cm/s/s

8 Meers Fault

The Meers fault is located in southwestern Oklahoma in Comanche and Kiowa counties. The northwest trending fault scarp has shown prominent activity in the recent geological time during the Holocene. Due to the lack of movement in the historic record, very little work has been done to update the hazards that may be associated with the Meers fault. The last time the fault had a major rupture was approximately 1,300 years ago and could have ranged from a magnitude 6 to greater than a magnitude 7. The hazards assessment done by organizations such as the United States Geological Survey (USGS) may not fully capture the possible magnitudes and ground motions in which the Meers fault could be capable of generating. The national hazard map by the USGS has a single recurrence interval of 4,500 years. This recurrence interval may not represent the potential range for the Meers Fault. The Oklahoma Geological Survey (OGS) re-evaluated the potential size of an earthquake that could occur along the fault. With help from newly available digitally imagery, the possible surface rupture length was re-evaluated. The OGS presents an up-to-date assessment of the Meers Fault using a full range of variables and updated information to obtain a more accurate picture of the hazards associated with the fault.

8.1 Geologic Background

The Meers fault is part of the Wichita Frontal Fault (WFF) system, which separates the Anadarko-Ardmore Basin to the northeast and the Wichita-Amarillo uplift to the southwest (Harlton, 1963). The WFF system extends about 175 km across southern Oklahoma and parts of the Texas Panhandle (Ham et al., 1964; Harlton, 1963). Between the late Precambrian and early Cambrian (~ 540 Ma), an early stage of rifting occurred and produced igneous body intrusions and basaltic flows in addition to normal faulting (Crone and Luza, 1990; Luza et al., 1987). In the early periods of rifting, the igneous rocks were gabbro, anorthosite and troctolite in composition. Later, the composition became hypabyssal granite and rhyolite and ended with thick rhyolitic magmas (Luza et al., 1987). During the late Cambrian to late Mississippian, subsidence of the Anadarko basin begin with mostly nonclastic sediments of carbonates and some quartz sandstones (Crone and Luza, 1990; Luza et al., 1987). Sedimentation during this time period was prevalent, because sediments total over 3 km in thickness at the basin's deepest part (Luza et al., 1987). In the early Pennsylvanian to Permian, the tectonically active area experienced block faulting, uplift and syntectonic sedimentation to form a deep basin over 7.5 km (Luza et al., 1987). Due to crustal weaknesses from the Cambrian, the uplift caused left slip to occurred along the fault (Crone and Luza, 1990; Luza et al., 1987). The displacement and throw of the fault are difficult to determine and, therefore, unknown (Crone and Luza, 1990).

The scarp of the Meers fault is present in the Quaternary indicating a recent movement. Any movement in the post-Paleozoic is difficult to determine because of the lack of Permian rocks in the exposures (Crone and Luza, 1990). The oldest evidence in the Quaternary occurs as offset in valleys and ridges in the middle to late Pleistocene sediments (Jones-Cecil, 1995; Luza et al., 1987). The displaced alluvium deposits coupled with carbon (C^{14}) dating tells us the movement faulted through all but the most recent Alluvium unit, East Cache Alluvium (Crone and Luza, 1990; Luza et al., 1987; Madole, 1988). The C^{14} dating has suggested that the most recent scarp movement occurred about 1,700-1,300 years ago (Luza et al., 1987).

8.2 Structure of the Meers Fault

The regional horizontal compressive stress for the North America is known to be NE to ENE which favors left-lateral movement on WNW faults like the Meers fault (Crone and Luza, 1990). During the Paleozoic, the faulting occurred down to the north with an estimated slip of 2 km (Jones-Cecil, 1995, Crone and Luza, 1990). The Quaternary faulting is down to the south with a left-lateral slip component (Jones-Cecil 1995, Crone and Luza, 1990). Near the northwestern end of the fault, splaying appears to have occurred which would be geometrically consistent with rupture propagation barriers (Jones-Cecil, 1995). This may have terminated the ruptures during either one or both Quaternary movements. The secondary faults on the southeastern end on the scarp are not apparent in ground-magnetic profiles (Jones-Cecil, 1995). This could be due to the faults being primarily strike-slip or limited to a non-magnetic sedimentary section.

The scarp trends N60°W. Estimates for the rupture length of the Meers fault vary significantly. The original estimate of 26 km is based on the length of scarp apparent in the sediment (Luza et al., 1987, Crone and Luza, 1990). However, in low-angle sun aerial photograph of the southeastern extension, the surface rupture length was revised to about 37 km (Ramelli and Slemmons, 1986). Based on the geophysical expression, the rupture length in the subsurface could be as long as 70 km (Slemmons et al., 1980). Based on measurements taken from the digital imagery, the visible scarp extends approximately 30.1 km (Figure 8.1). Using the USGS Quaternary fault database (USGS, 1994), the inferred scarp to the northwest until the splaying is about 11.5 km, and the inferred scarp to the southeast is about 6.9 km. The total length from the southeast end to the top splay (4.9 km) is roughly 53.3 km. The length of the bottom splay was measured at 5.8 km and used as a continuation on the linear path of the actual scarp to get a total length of 54.3 km. Applying the surface rupture length relationship of (Wells and Coppersmith, 1994) the estimates for surface rupture length of strike-slip faults provide a magnitude range from 6.74 to 7.10 with an uncertainty of about 0.25 magnitude units, and using the relationship for a reverse fault we get about the same range, but the uncertainty is nearly double. If we consider the subsurface rupture length proposed by Slemmons et al. (1980) we get a magnitude of 7.08 consistent with other estimates for magnitude.

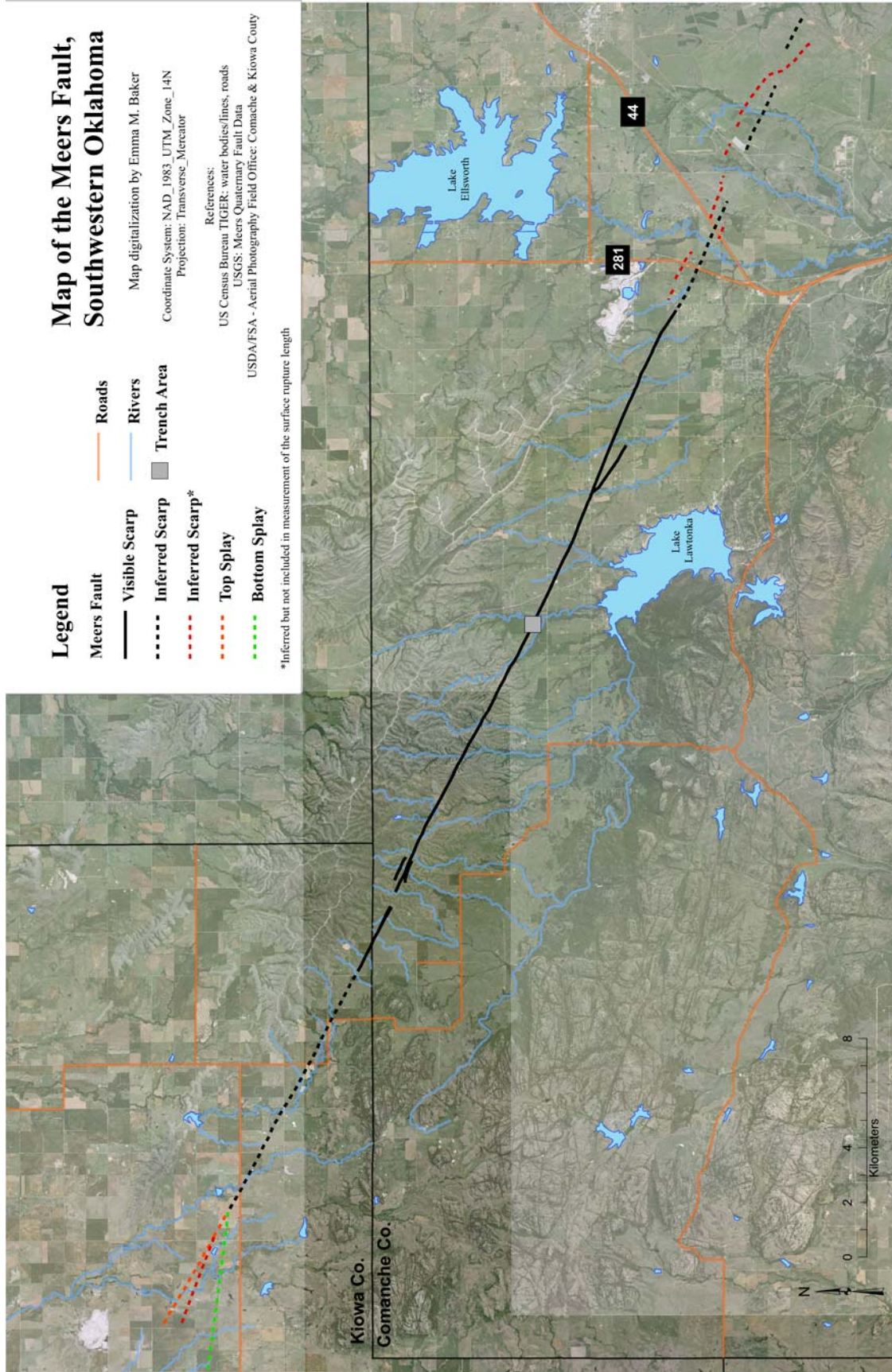


Figure 8.1 – Fault segments for the Meers Fault (USGS, 1994).

8.3 Previous Studies of the Meers Fault

In a previous study, two trenches were dug to get a better idea of the Meers fault (Crone and Luza, 1990). The trench area on the map in Figure 8.1 is the general location of the two trenches. The first trench is located about 150 m ESE of Canyon Creek and the second is located approximately 200 m ESE of trench 1.

Trench 1 was 22 m long and about 2.5 m deep. The dimensions of the scarp in this area was roughly 2.4 m high with an estimated minimum surface offset of 2.2 m and a maximum slope angle of $9^{\circ}22'$. There was clear faulting in through the Hennessey shale near the bottom of the trench and the Browns Creek Alluvium (early to middle Holocene). However, there was no faulting or deformation in the East Cache Alluvium of late Holocene age toward the top of trench 1. The alluvium was warped into a monocline over the fault movement. This implies that the scarp never had a large free face, but there are strong stratigraphic relationships indicating a surface-rupture event. There was 2 m of brittle deformation near the center of the scarp with secondary faulting probably in response to the warping. The southwest side of the fault is reverse separation and near-surface compression due to the monocline. On the northeast side, the normal separation was due to extension. There was less than 1 m of displacement for both secondary faults.

Trench 2 was 19 m long. Due to a high water table, the deepening of the trench was limited, so the bedrock on the on the downthrown side of fault could not be exposed any further. The scarp was about 3.4 m high with a surface offset of 3.0 m and a maximum slope angle of 9° . The fault strikes $N64^{\circ}W$, and dips $56^{\circ}NE$. The bedrock consisted of the Hennessey shale and dolomite, which was adjacent to the fault on the upthrown side. The Porter Hill Alluvium of Pleistocene age was clearly faulted. The stratigraphic throw in the trench was measured at a minimum value of 3.2 to 3.3 m. The warping of the bedforms accounts for 70% to 85% of the deformation at trench 2, and the brittle fracturing is more prominent as compared to trench 1.

Within surficial deposits mapped in trenches the Meers Fault can be seen to have varying dip angles. However, from geophysical data the dip of the Meers fault at depth appears to be quite steep between vertical and 70° (Jones-Cecil, 1995). Estimates of the ratio of strike-slip motion to reverse vertical motion on the fault vary, but generally are on the order of about 1.3-1.5 (Crone and Luza, 1990; Kelson and Swan, 1990) consistent with a rake between 35° and 40° (Kelson and Swan, 1990). For this study we consider the case of a vertical fault and pure strike slip motion or the case of a 70° dipping fault with a rake of 30° which would indicate a ratio of left-lateral to reverse motion greater than 1.5.

8.4 Recurrence Intervals of the Meers Fault

The recurrence rate for the Meers Fault will dramatically control seismic hazard estimates. The Meers Fault is largely aseismic since modern seismic monitoring has occurred in Oklahoma (1978). The lack of seismic activity makes it difficult to assess recurrence rates using modern seismicity. The last major earthquake with surface rupture known to have occurred on the Meers Fault was between 800 and 1,600 years before present (B.P) (Crone and Luza, 1990; Kelson and Swan, 1990; Luza et al., 1987; Madole, 1988) with a preferred value of 1280 ± 140 years B.P. (Crone and Luza, 1990). Recurrence estimates vary dramatically and require further investigation, as they are the largest control on seismic hazard associated with the Meers Fault. Recurrence estimates range from 500,000 years (Crone and Luza, 1990) to about 1,300 years (Kelson and Swan, 1990). These different values have very different implications to seismic hazard and

demonstrate the need for further work to more rigorously constrain recurrence intervals. Because of this, we can only estimate the recurrence interval of the fault. The CEUS-SSC (2011) considered the short recurrence interval to occur within a cluster with a recurrence interval to be 2,153-2,968 years. In this study, we considered the hazard for recurrence intervals of 1,300, 4,500, 20,000 and 100,000 years to estimate the earthquake hazards for the Meers fault.

9 Probabilistic Seismic Hazard Assessment

The Probabilistic Seismic Hazard Assessment (PSHA) was determined using the software OpenQuake version 0.7.0 released May 10, 2012 (Crowley et al., 2012). This software uses the OpenSHA (Field et al., 2003) platform to conduct the PSHA calculations. The PSHA is determined by conducting multiple Monte Carlo traverses of a probabilistic logic-tree. For all cases and results shown here, 1,000 traverses of the logic tree were conducted. The first branch in the logic-tree is a description of the earthquake source models. The next branch in the logic-tree describes the maximum magnitude probabilities for the earthquake sources, and the final branch of the logic-tree is the ground motion prediction equations (GMPE). All PSHA outputs in this study are the mean Uniform Hazard Spectra (UHS) or equal hazard mean spectra for different spectral periods and return periods as specified in ER 1110-2-1806. The UHS ground motion measure is the GMRotI50 (Boore et al., 2006), which is a modified average horizontal acceleration. The hazard is computed independently for each period with an equal probability of exceedance. This means that the UHS doesn't represent the spectra of any particular scenario earthquake or measured earthquake.

9.1 Earthquake Source Models

For this study we only consider earthquake sources within 200 km of the Arcadia Dam Site. We are generating area sources within Oklahoma using our determined Gutenberg-Richter relationships including both the de-clustered catalog from 1882-2011 as well as the clustered seismicity from 2009-2011. The uncertainties from the associated Gutenberg-Richter b-value relationship are also considered in the area source model. The area sources were calculated using a point source as well as line sources. The final results were generated using a cross-hair line source, which takes into account the two most likely orientations of faulting given the regional stress field in Oklahoma and observed focal mechanisms within the state. We consider strike-slip motion on faults with strike orientations of 55° and 145° with dips of 90°. We demonstrated the difference between using finite earthquake ruptures and ground motions determined from a point source. The earthquake ruptures are scaled following the relationships of Wells and Coppersmith (1994). The final area source logic-tree is shown in Figure 9.1.

9.2 Maximum Magnitude

It is common practice within a PSHA to truncate the Gutenberg-Richter relationship with a maximum magnitude M_{max} . Rather than derive a poorly constrained maximum magnitude we will consider maximum magnitudes used within the region by previous studies. The USGS Hazard Map 2008 used multiple M_{max} for the Central and Eastern United States (CEUS) with a maximum of 7.2 (Petersen et al., 2008). The M_{max} USGS logic tree for the CEUS was incorporated fully as one possibility in our models. The other recent determination for M_{max} in

the CEUS for non-Mesozoic and younger extension was included with a maximum M_{max} of 8.0 (CEUS-SSC, 2012). These two models will be included as individual branches in the logic-tree each with an equal weight (Figure 9.2).

9.3 Ground Motion Prediction Equations

The Ground Motion Prediction Equations (GMPE) use the calculated earthquakes from the earthquake source models and describe the level of ground motion at a given site generated from a scenario earthquake similar to the discussion in the previous chapter. Four different GMPE relations were used to determine ground motions at the Arcadia Dam site for periods of 0.01, 0.02, 0.03, 0.05, 0.075, 0.1, 0.3, 0.5, 1.0, 2.0, 3.0, and 4.0 seconds (s) (Abrahamson and Silva, 2008; Boore and Atkinson, 2008; Campbell, 2003; Campbell and Bozorgnia, 2008; Chiou and Youngs, 2008). The four different GMPE relationships were assigned equal probabilities of occurrence (Figure 9.3). For most cases we used a V_{s30} value of 600 m/s. This value is commonly used as a reference value for PSHA within the CEUS; and is within the uncertainty of the measured value near the ADOK accelerometer site. We considered the possibility of a V_{s30} of 281 m/s, which is what was measured below the Arcadia Dam. In addition some of the ground motion prediction equations required specifications of depth to reference shear wave velocities of 1.0 and 2.5 km/s. These values were taken from a velocity model derived for this area from the nearby earthquakes. The depth values used are 100.0 m for a velocity of 1 km/s and 500.0 m for a velocity of 2.5 km/s.

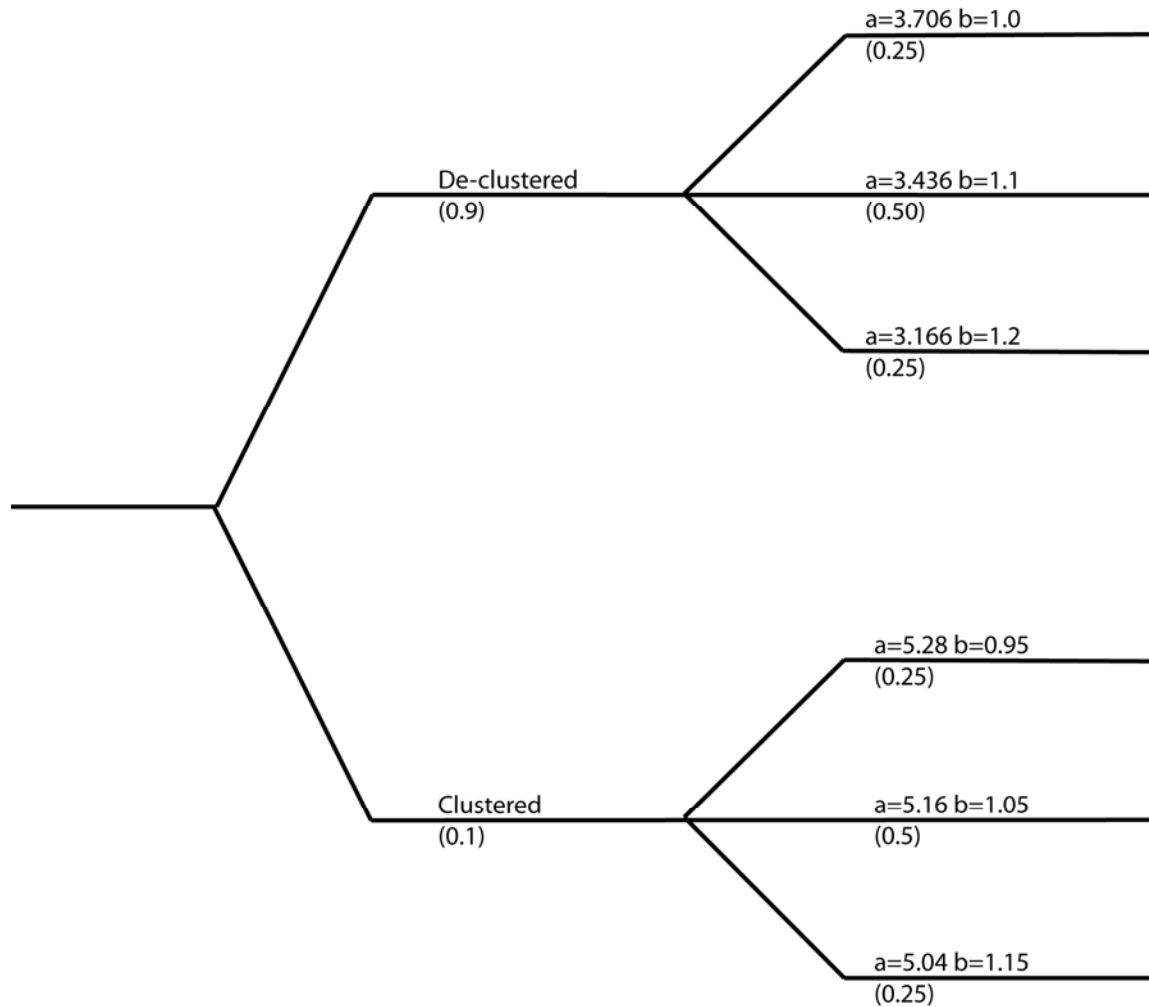


Figure 9.1 – Area source logic tree for the case shown in the final results. Earthquake occurrence models are shown above a branch line and the probability of occurrence for that branch is shown in parentheses below the branch line. This considers the occurrence of the increased clustered seismicity to be much less likely than the de-clustered earthquake rates.

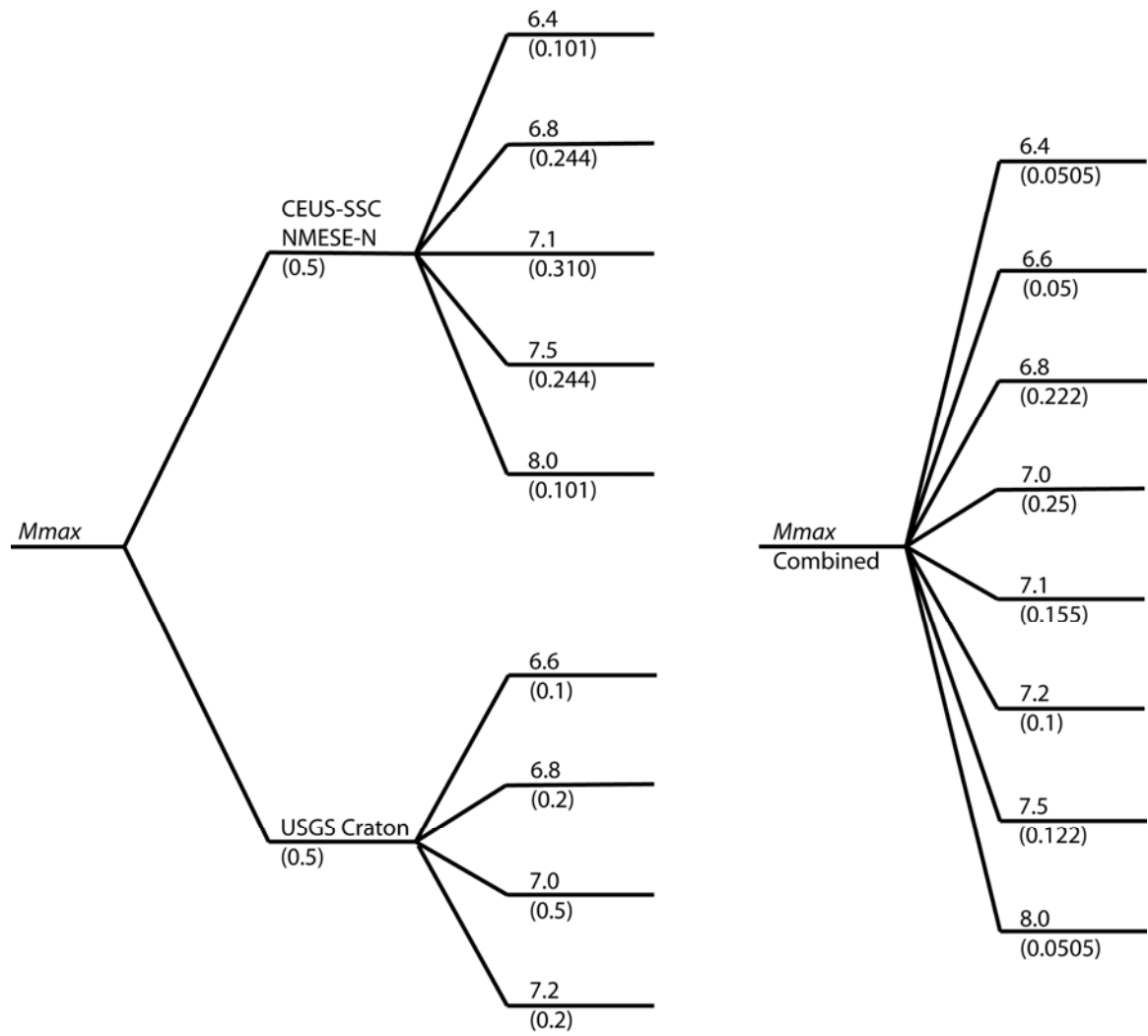


Figure 9.2 - M_{max} logic tree used for the determination of a truncated Gutenberg-Richter relationships for area source within the PSHA. The maximum magnitude model is listed above the branch line and the probability of occurrence for that branch is shown in parentheses below the branch line.

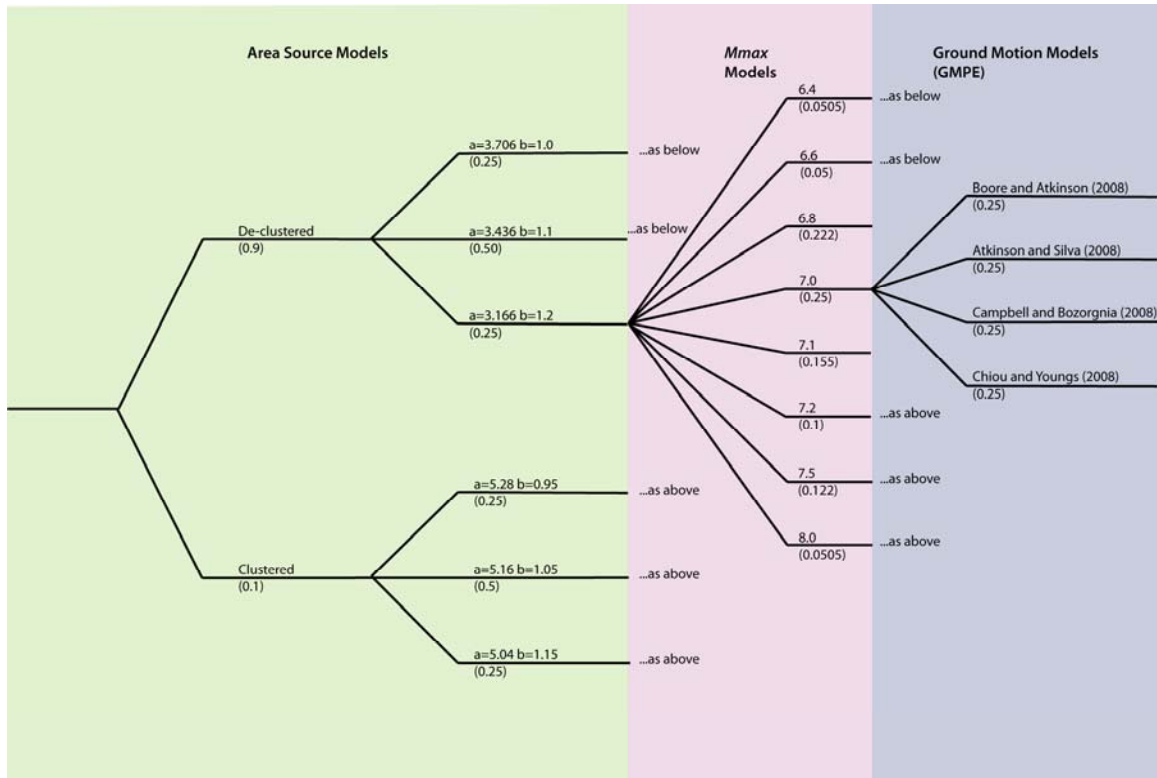


Figure 9.3 – Complete logic tree including only area sources used for comparing results of PSHA from the different area sources.

9.4 Comparison of Area Sources in PSHA

The logic tree including only area sources used in the comparison calculations is shown in Figure 9.3. The area sources were changed from the probabilities shown in Figure 9.1 and 9.3 such that one branch had a probability of 1.0 and the other branch had a probability of 0.0. The two different models are referred to by the name of the branch with a probability of 1.0 so de-clustered and clustered. The effect of the two different area source branches in the logic tree can be seen in Figure 9.4 and 9.5. The clustered model resulted in significantly greater UHS ground motions. For a spectral period of 0.1 s, the clustered model resulted in about 4 times greater ground motion for a 10,000 year return period and a about 10 times greater ground motion for a 950 year return period than the de-clustered model. We examined the difference in the use of point sources for the area source and finite line sources oriented in a cross-hair pattern. The finite line sources provide between about 30% and 150% greater ground motions than those determined from point sources. Figure 9.6 shows the PSHA results for point sources using the final logic tree.

The probability for the clustered logic tree branch in this example was set at 10%. It was selected to be a low value because the earthquake recurrence rates of the past few years are much greater than anything observed in the past. A comparison of Figures 9.7, 9.4 and 9.5 demonstrates that the 10% probability for the clustered source don't cause a significant deviation from the de-clustered source. For this reason, the final probability for the clustered source was set at 20% so that it is still a low likelihood occurrence, but also has some expression in the hazard calculation models.

Site amplification was largely modeled through the parameter of shear wave velocities within the first 30 m of the surface (V_{s30}). Because we measure two distinctly different V_{s30} values near the Arcadia Dam we conducted PSHA calculations for a V_{s30} of 600 m/s (Figure 9.7) and 281 m/s (Figure 6.8). V_{s30} at 281 m/s results in somewhat greater mean UHS ground motion than the higher V_{s30} value. The primary difference is that the mean UHS hazard at 0.3 s period is increased significantly using a V_{s30} of 281 m/s. Comparison with the USGS UHS (Figure 9.9) curves available online (USGS, 2012b) for the 2008 seismic hazard maps (Petersen et al., 2008) show much greater ground-motions than those obtained in this study. These ground motions are much more comparable to those of the clustered earthquake model. The USGS hazard calculations include the Meers fault as a known source and it is only 150 km from the Arcadia Dam, and was included in the final PSHA calculations.

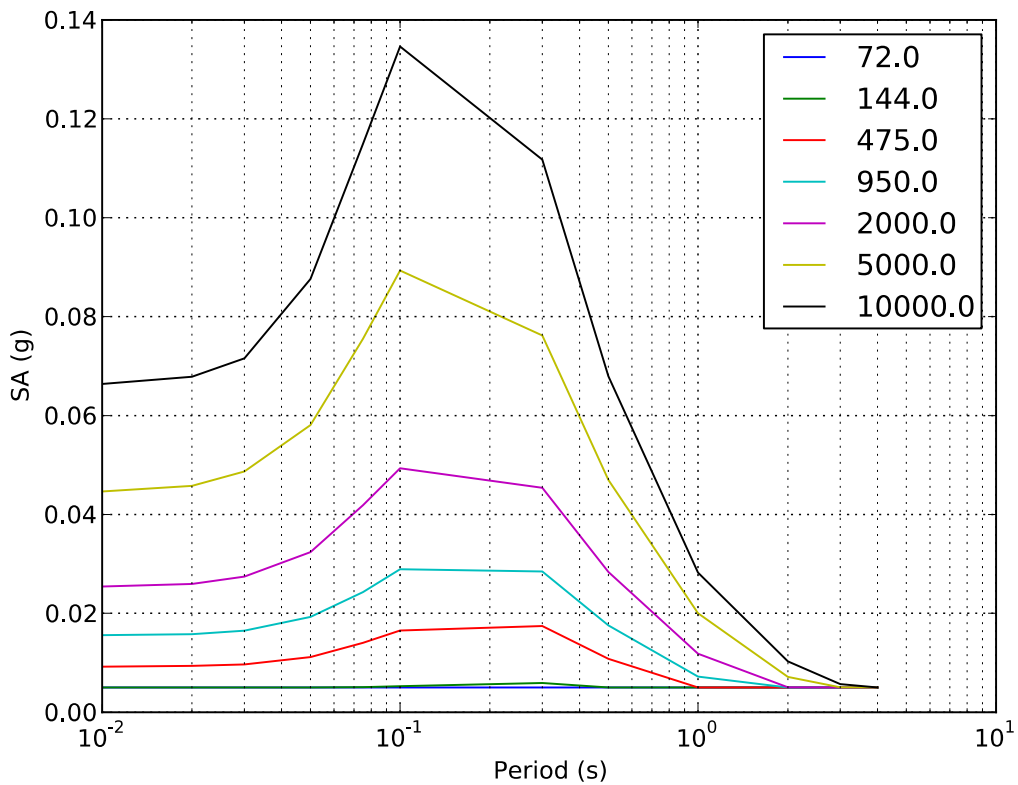


Figure 9.4 – Mean UHS for the de-clustered area source model is based on the Gutenberg-Richter recurrence parameters for the de-clustered earthquake catalog from 1882-2011 using a V_{s30} of 600 m/s. The de-clustered logic-tree is available in the Electronic Supplement ES5.

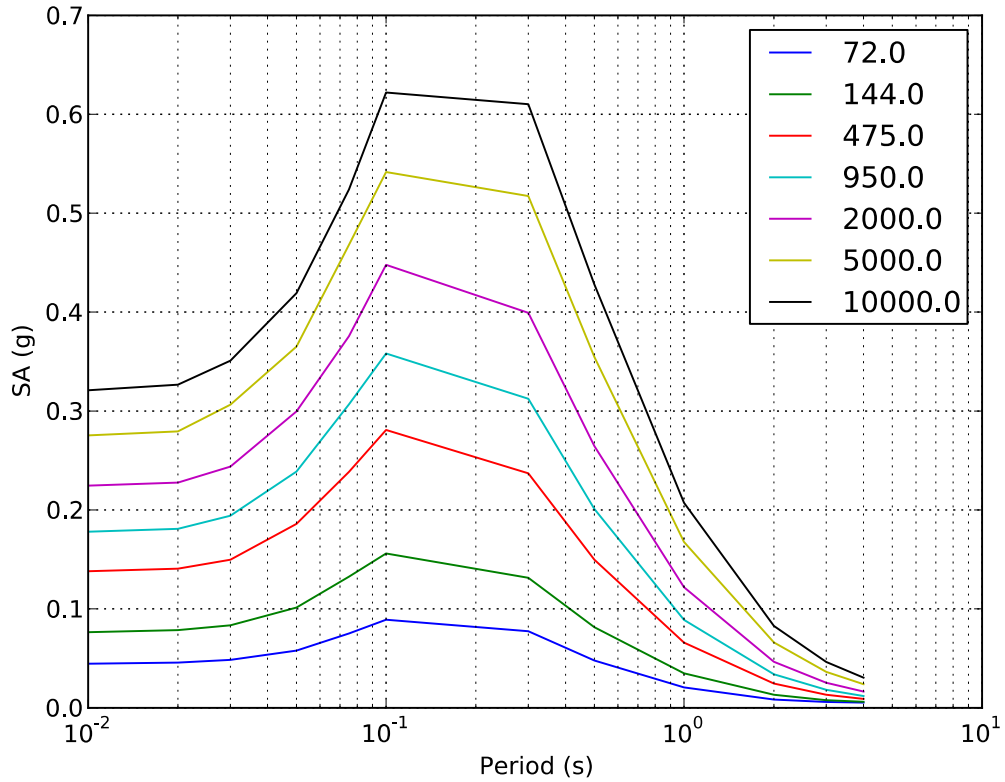


Figure 9.5 – Mean UHS for the clustered area source model is based on the Gutenberg-Richter recurrence parameters for the complete catalog from 2009-2011 using a V_{s30} of 600 m/s. The clustered logic tree is available in the Electronic Supplement ES5.

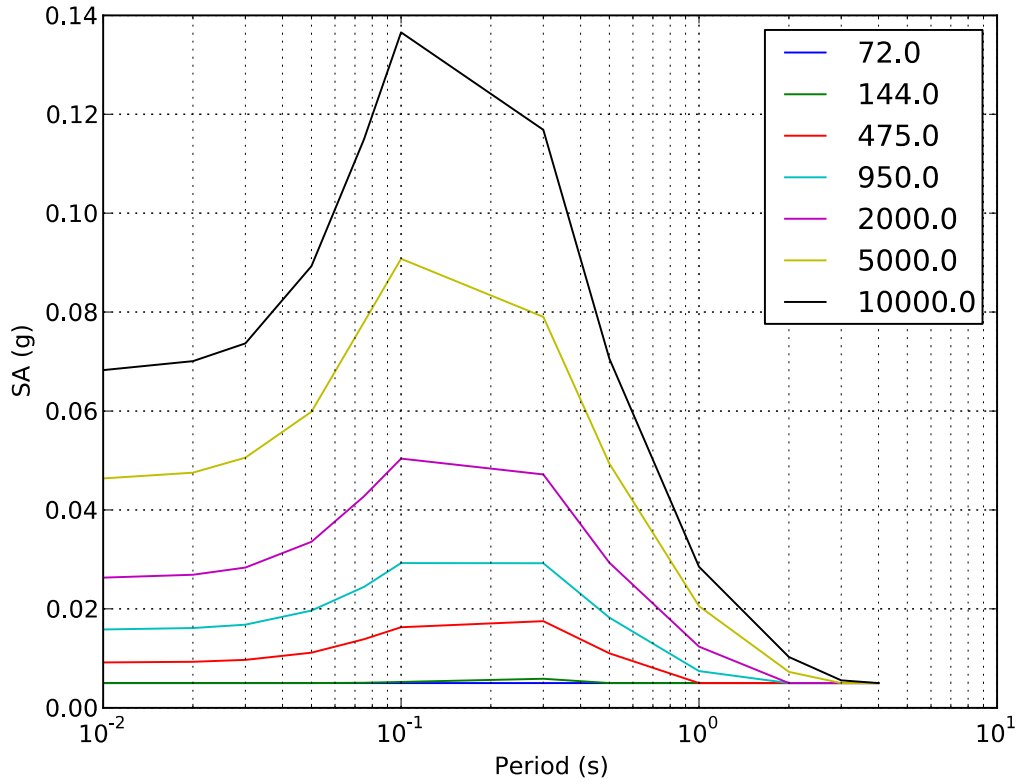


Figure 9.6 – Mean UHS for the complete logic tree and area point sources instead of line sources with a Vs30 of 600 m/s. The complete logic tree is available in the Electronic Supplement ES5 and can be seen in Figure 9.3.

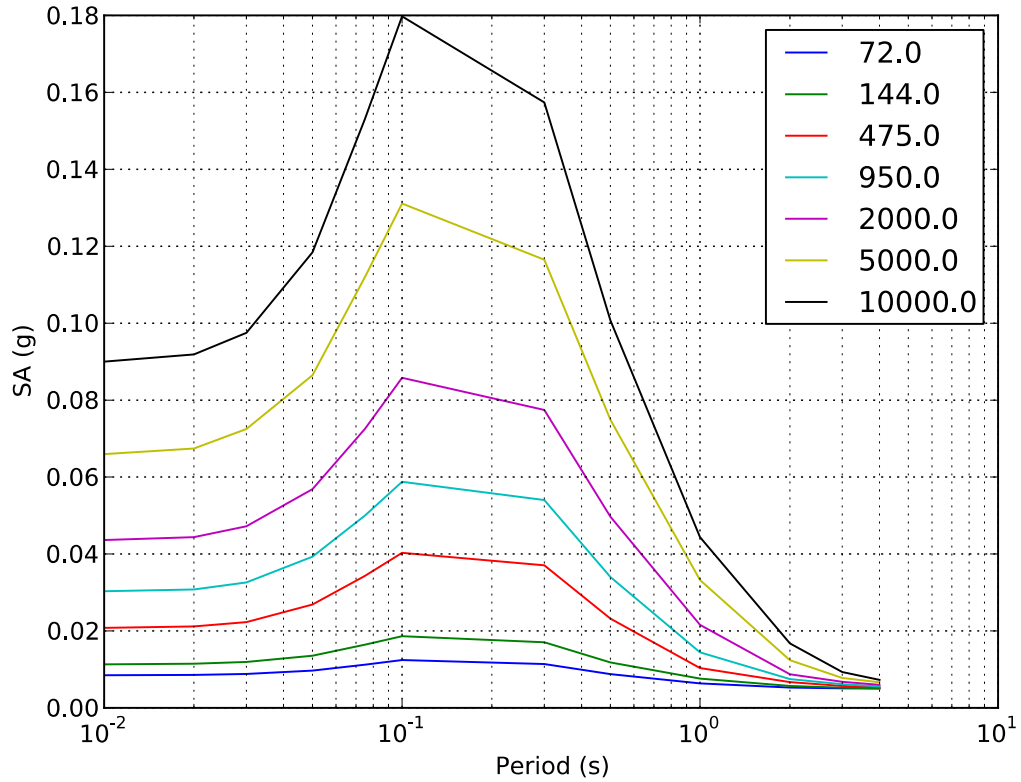


Figure 9.7 – Mean UHS for the complete area source logic tree using cross-hair line sources with a Vs30 of 600 m/s. The complete logic-tree is available in the Electronic Supplement ES5 and can be seen in Figure 9.3.

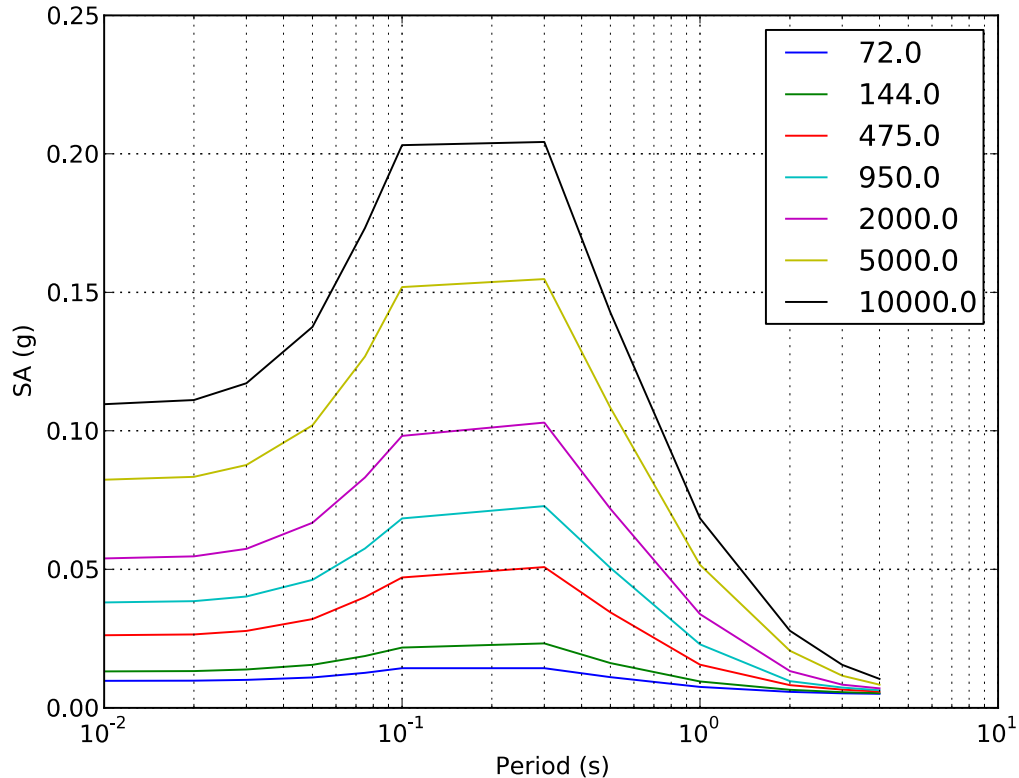


Figure 9.8 – Mean UHS for the complete area source logic-tree using cross-hair line sources with a V_{s30} of 281 m/s. The complete area source logic tree is available in the Electronic Supplement ES5 and can be seen in Figure 9.3.

9.5 Meers Fault PSHA Parameters

The Meers Fault is about 140 km from the Arcadia Dam, and the calculated UHS were not remarkably sensitive to the fault parameters used in this study. The USGS 2008 Hazard Map (Petersen et al., 2008) uses a simple model for the Meers Fault of a magnitude 7.0 ± 0.2 earthquake every 4,500 years. The Meers Fault sources considered in the CEUS-SSC (2012) are too complex to be considered in this study using the OpenQuake architecture to determine the PSHA. We first evaluated the sensitivity to the computed UHS for maximum magnitude and orientation of rupture along the fault. We consider the case from the USGS hazard map (Figure 9.9) and a strike-slip case with a maximum magnitude of 7.1 ± 0.25 (Figure 9.10). There is essentially no difference between Figures 9.9 and 9.10. The maximum magnitude of 7.1 is taken from the total possible length of the Meers Fault scarp and applying rupture length scaling relationships (Wells and Coppersmith, 1994). We now examine the effect associated with the dip of the Meers Fault assuming a dip of 70° and a rake of 30° , which is mostly strike-slip with a component of thrusting to account for the motion observed (Crone and Luza, 1990). The addition of the thrusting component increased ground motions slightly at the Arcadia Dam (Figure 9.11), and this scenario was used for the Meers Fault in all following calculations.

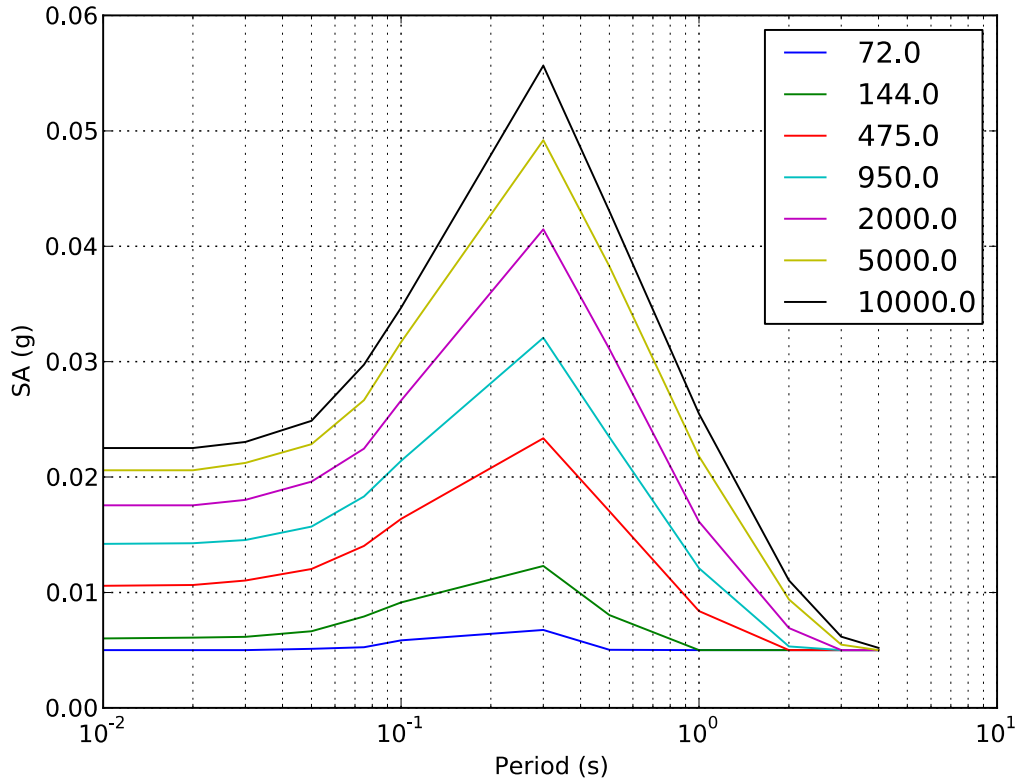


Figure 9.9 – Mean UHS computed for different return periods at the Arcadia Dam for the USGS hazard model (Petersen et al., 2008) for the Meers Fault.

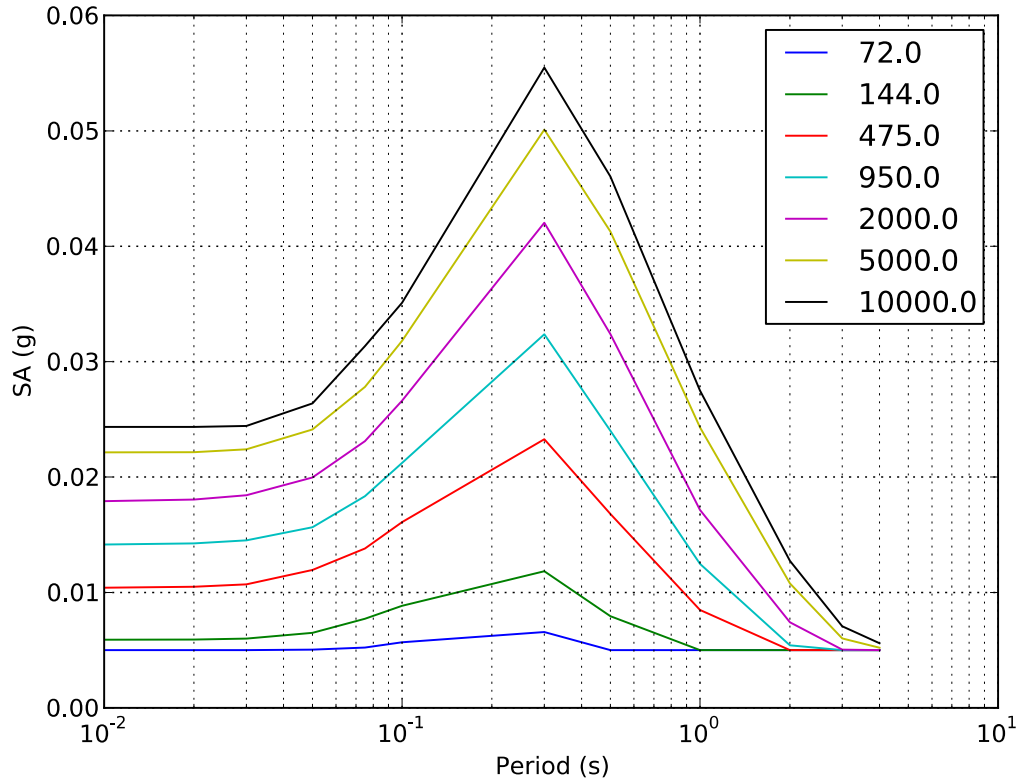


Figure 9.10 – Mean UHS for different return periods at the Arcadia Dam for strike-slip earthquakes on the Meers Fault.

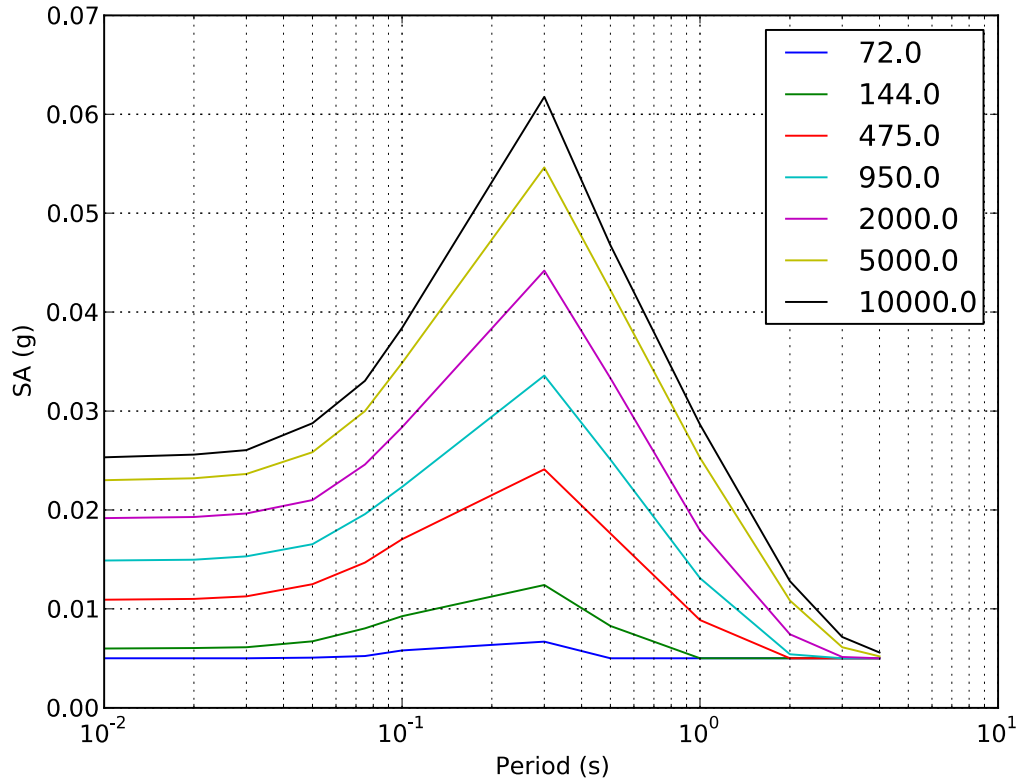


Figure 9.11 – Mean UHS for different return periods at the Arcadia Dam for earthquakes with mostly strike-slip and a component of reverse motion on the Meers Fault.

The greatest unknown and control to the hazard of the Meers Fault is the recurrence interval as discussed in Chapter 8. Here we examine the effect of recurrence interval on the estimated hazard at the Arcadia Dam. We evaluated recurrence intervals of 1,300, 4,500, 20,000, and 100,000 years (Figures 6.12). The effect on the inferred Gutenberg-Richter b-value relationship assuming a b-value of 1.0 and a magnitude 7.1 is presented in Table 9.1. For the final model a recurrence interval of 4,500 years was selected because the a-value is quite similar to that observed in the de-clustered catalog. However, a recurrence rate of 1,300 years is not inconsistent with the rates of de-clustered seismicity observed from 2009 through 2011. The recurrence rate of 20,000 years provides a slightly lower, but comparable a-value as the de-clustered catalog from 1882 through 2008.

Table 9.1 – Inferred Gutenberg-Richter a-values for different recurrence intervals of magnitude 7.1 earthquakes on the Meers Fault assuming a b-value of 1.0.

Recurrence Interval (Years)	a
1,300	3.9861
4,500	3.4468
20,000	2.799
100,000	2.01

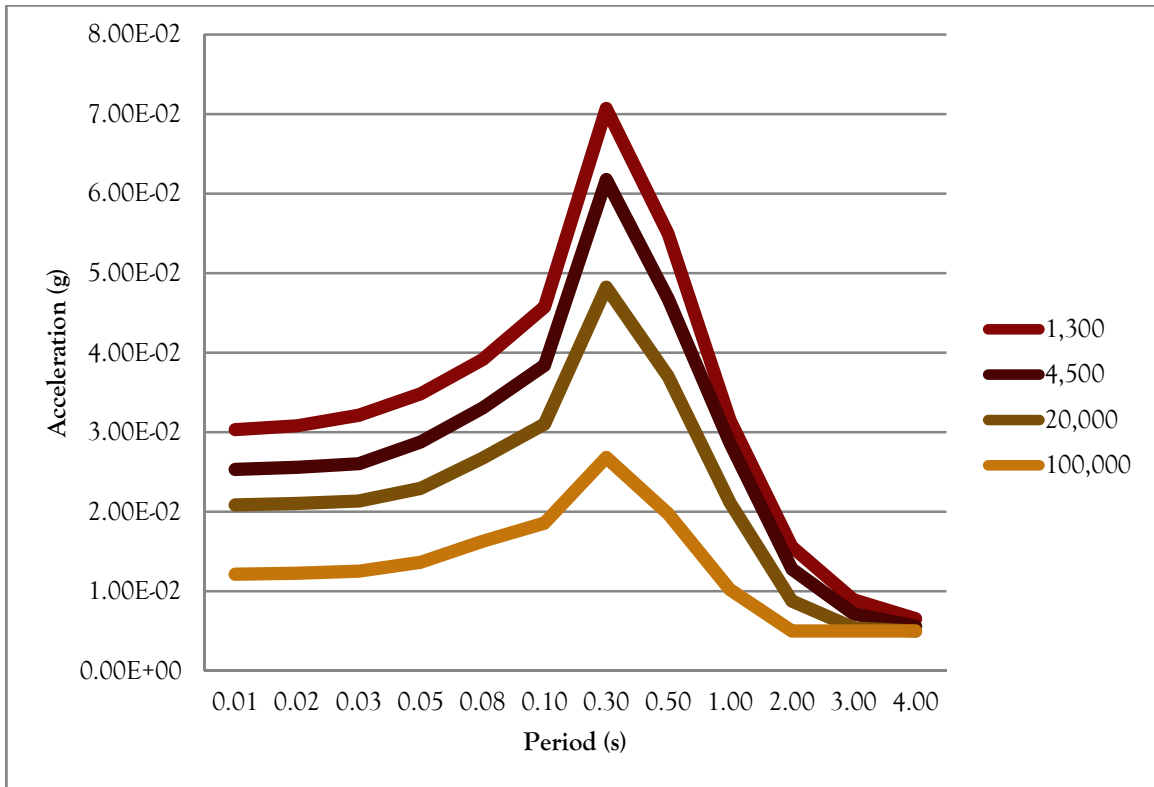


Figure 9.12 – Mean UHS for a return period of 10,000 years for different recurrence rates of a magnitude 7.1 earthquake on the Meers Fault.

10 Results of PSHA for Arcadia Dam

The final PSHA model includes two area sources. One represented the rate and its associated uncertainty determined for the de-clustered Oklahoma earthquake catalog from 1882 through 2011. The other area source considers the much greater earthquake rate from the complete catalog from 2009 through 2011 at a significantly smaller probability. The Meers Fault was included in all final PSHA models with a M 7.1 at a recurrence interval of 4,500 years. However, this did little to alter the overall hazard at the Arcadia Dam because it is about 140 km away. The final logic-tree (Figure 10.1) included the clustered source at a probability of 20% of the area sources. This probability did not have a significant effect on the overall computed mean UHS hazard curves. This value was chosen because the greater rate of seismicity has only occurred for a few years and has not been documented since the OGS installed a statewide monitoring system in 1978. For this reason a lower likelihood was given to the clustered model than the de-clustered model. The de-clustered model also includes the recent earthquake activity and so there is some input from the recent seismicity in the de-clustered model. When giving the clustered source full weight in the logic tree ground motion predictions from the PSHA are much greater. It is unclear how best to account for the observed increased seismicity rate over the past few years. The possibility of high seismicity rates were included in our PSHA calculations. This provided for a good deal of variability between different samples of the logic-tree. The logic tree was sampled 1,000 times for each of the final calculations, and took about 8 hours to compute.

We consider all earthquakes down to magnitude 4.7 in the hazard calculations. This is the magnitude that can potentially damage nearby structures. Generally this value is set to 5.0 or even greater for the same reason we used a value of 4.7. This choice may have the effect of slightly reducing the mean UHS.

For the final results we consider two different cases based on the two different V_{s30} velocities measured near the Arcadia Dam. The results for a V_{s30} of 600 m/s are shown in Table 10.1 and Figure 10.2, and the results for a V_{s30} of 281 m/s are shown in Table 10.2 and Figure 10.3. To demonstrate the variability between different logic tree samplings and the associated UHS for that sampling a compilation was made for the standard deviation of the UHS for the final two scenarios (Table 9.4). The results for a V_{s30} of 600 m/s provided fairly comparable ground motions to the previous study (Lawson, 1985). The PSHA results for a V_{s30} of 281 m/s resulted in larger ground motions than the Lawson (1985) study. The Lawson (1985) study determined the maximum ground motions expected for each return period, and we are determining the mean UHS (equal hazard spectra). The maximum ground motions would be significantly larger in this study than those reported previously. The maximum ground motions estimated for the M 5.6 2011 Prague earthquake exceeded maximum horizontal ground motion of Lawson (1985) for a 2,000-year return period.

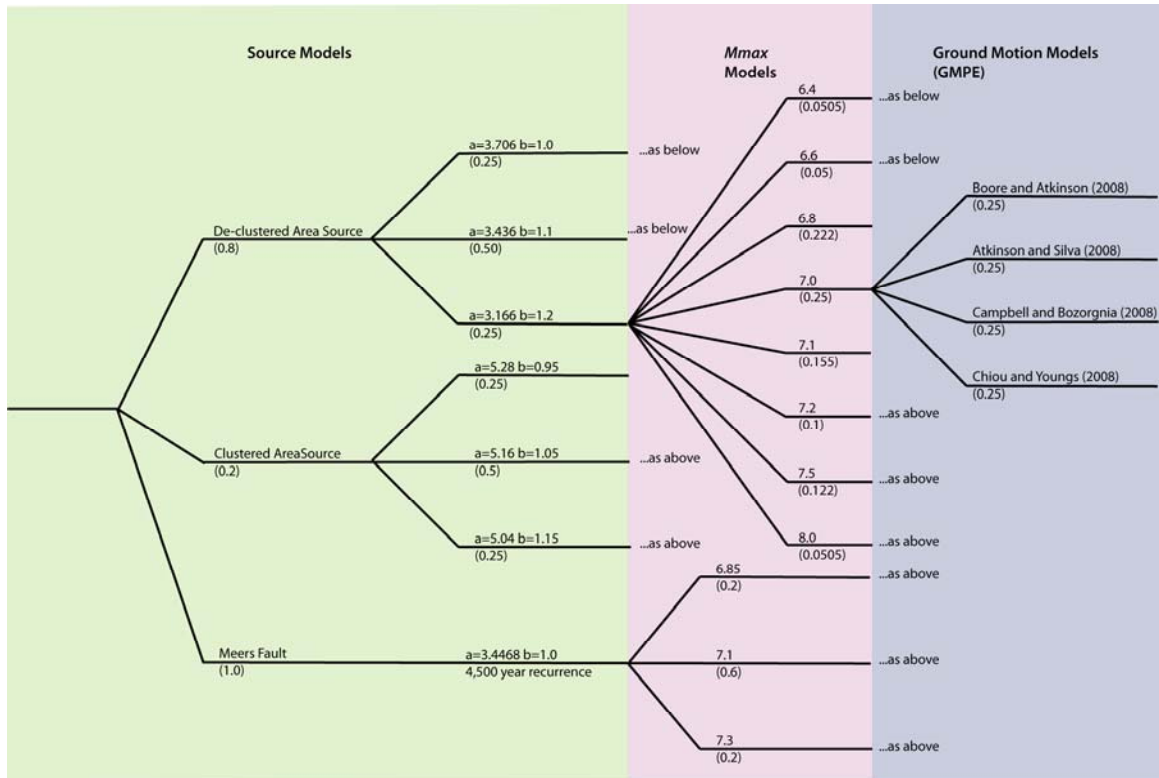


Figure 10.1 – Complete logic tree for final PSHA calculations. The Meers Fault is not a distinct source, but is included as a source with the shown parameters in each source model. The complete logic tree in expanded format is available in the Electronic Supplement ES5.

Table 10.1 – Mean UHS for acceleration in units of g for different spectral amplitude periods and return periods for the case where V_{s30} is 600 m/s.

Return Period (years)	72	144	475	950	2000	5000	10000	
Period (s)	0.01	1.29E-02	2.13E-02	4.02E-02	5.28E-02	6.74E-02	9.14E-02	1.18E-01
	0.02	1.31E-02	2.18E-02	4.08E-02	5.36E-02	6.86E-02	9.31E-02	1.20E-01
	0.03	1.37E-02	2.30E-02	4.30E-02	5.66E-02	7.30E-02	1.01E-01	1.28E-01
	0.05	1.57E-02	2.72E-02	5.16E-02	6.78E-02	8.76E-02	1.21E-01	1.55E-01
	0.08	1.97E-02	3.49E-02	6.52E-02	8.56E-02	1.10E-01	1.56E-01	1.99E-01
	0.10	2.31E-02	4.08E-02	7.65E-02	9.99E-02	1.30E-01	1.81E-01	2.34E-01
	0.30	2.23E-02	3.92E-02	7.36E-02	9.83E-02	1.27E-01	1.66E-01	2.12E-01
	0.50	1.39E-02	2.51E-02	4.85E-02	6.57E-02	8.61E-02	1.13E-01	1.41E-01
	1.00	8.03E-03	1.10E-02	2.23E-02	3.05E-02	4.22E-02	5.65E-02	6.68E-02
	2.00	5.59E-03	6.53E-03	8.89E-03	1.18E-02	1.65E-02	2.30E-02	2.82E-02
	3.00	5.12E-03	5.47E-03	6.54E-03	7.51E-03	9.24E-03	1.26E-02	1.57E-02
	4.00	5.02E-03	5.15E-03	5.70E-03	6.28E-03	7.16E-03	8.97E-03	1.08E-02

Table 10.2 – Mean UHS for acceleration in units of g for different spectral amplitude periods and return periods for the case where Vs30 is 281 m/s.

Return Period (years)	72	144	475	950	2000	5000	10000	
Period (s)	0.01	1.64E-02	2.77E-02	5.01E-02	6.49E-02	8.01E-02	1.09E-01	1.37E-01
	0.02	1.65E-02	2.80E-02	5.06E-02	6.55E-02	8.09E-02	1.11E-01	1.40E-01
	0.03	1.71E-02	2.93E-02	5.28E-02	6.82E-02	8.48E-02	1.17E-01	1.47E-01
	0.05	1.95E-02	3.37E-02	6.06E-02	7.75E-02	9.82E-02	1.35E-01	1.71E-01
	0.08	2.42E-02	4.20E-02	7.49E-02	9.48E-02	1.20E-01	1.66E-01	2.13E-01
	0.10	2.89E-02	4.96E-02	8.75E-02	1.12E-01	1.41E-01	1.97E-01	2.49E-01
	0.30	3.25E-02	5.56E-02	9.91E-02	1.28E-01	1.62E-01	2.08E-01	2.59E-01
	0.50	2.17E-02	3.81E-02	7.12E-02	9.57E-02	1.24E-01	1.61E-01	1.92E-01
	1.00	1.05E-02	1.74E-02	3.45E-02	4.80E-02	6.47E-02	8.51E-02	1.03E-01
	2.00	6.51E-03	8.22E-03	1.39E-02	1.95E-02	2.69E-02	3.70E-02	4.59E-02
	3.00	5.51E-03	6.31E-03	8.38E-03	1.11E-02	1.51E-02	2.09E-02	2.57E-02
	4.00	5.18E-03	5.61E-03	6.78E-03	8.07E-03	1.04E-02	1.43E-02	1.75E-02

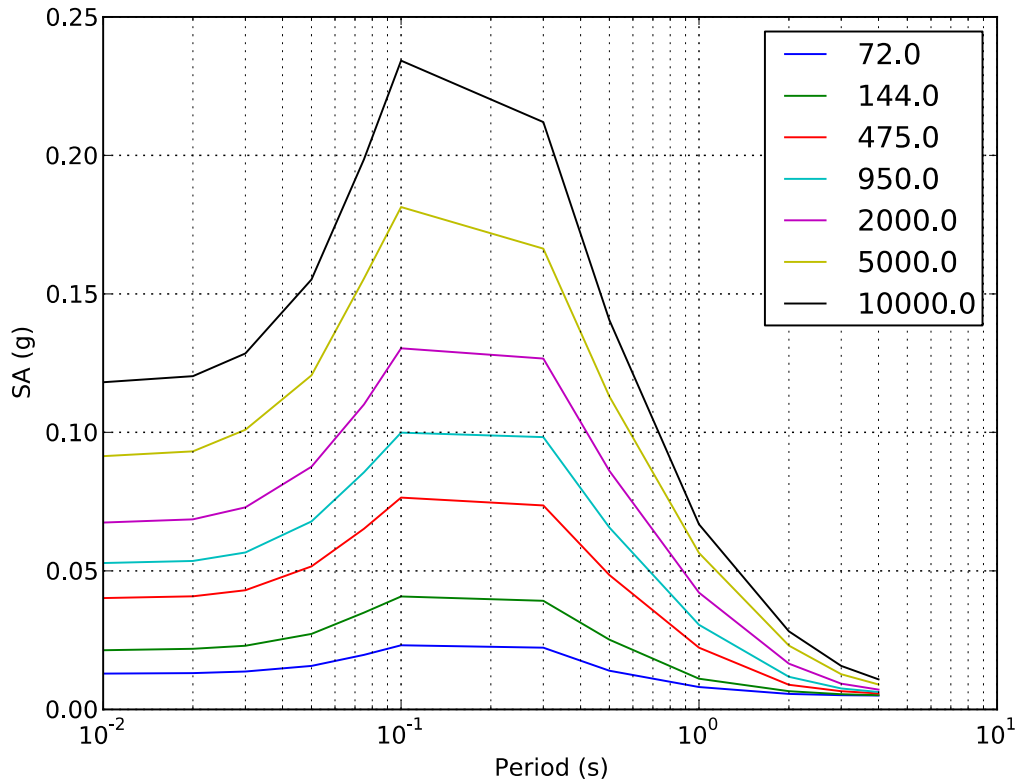


Figure 10.2 – Mean UHS for different return periods for the case where Vs30 is 600 m/s. The complete logic tree is available in the Electronic Supplement ES5 and can be seen in Figure 10.1.

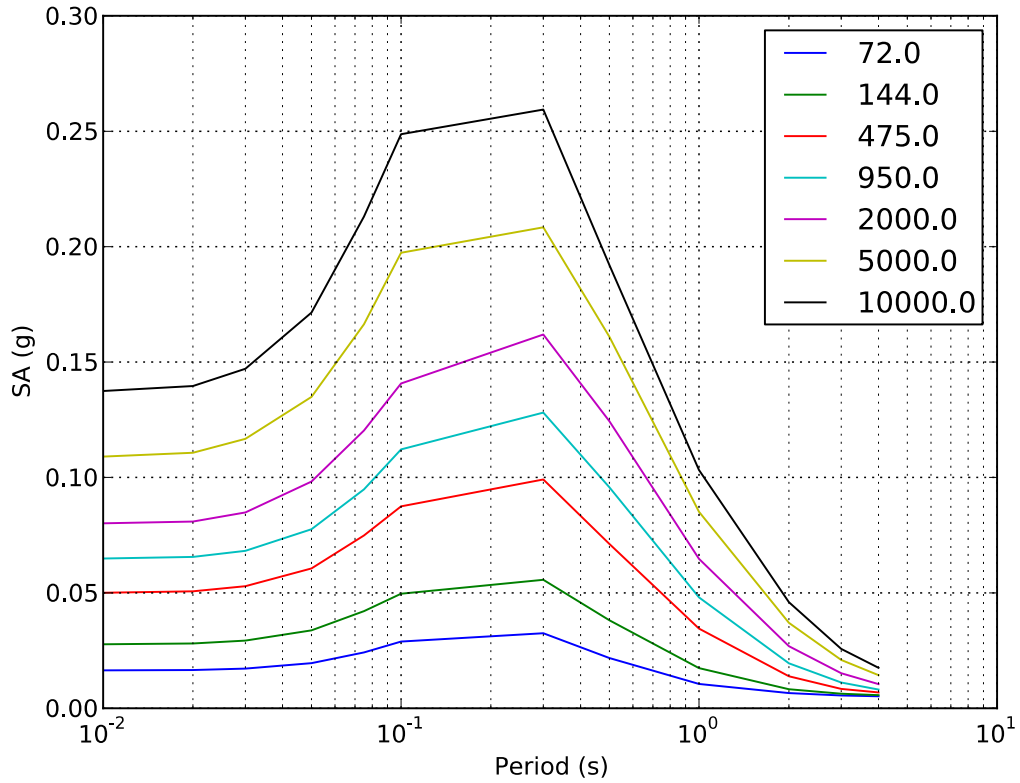


Figure 10.3 – Mean UHS for different return periods for the case where Vs30 is 281 m/s. The complete logic tree is available in the Electronic Supplement ES5 and can be seen in Figure 10.1.

Table 10.3 – Standard deviation values in acceleration units of g for the mean UHS values reported in this study. Demonstrating the significant variability between different logic-tree samples.

Return Period	72		144		475		950		2000		5000		10000		
VS30	600	281	600	281	600	281	600	281	600	281	600	281	600	281	
Period (s)	0.01	1.85E-02	2.43E-02	3.09E-02	3.80E-02	5.40E-02	6.11E-02	6.73E-02	7.45E-02	8.36E-02	8.80E-02	9.65E-02	9.87E-02	1.06E-01	1.03E-01
	0.02	1.90E-02	2.46E-02	3.17E-02	3.87E-02	5.48E-02	6.22E-02	6.84E-02	7.60E-02	8.45E-02	8.97E-02	9.78E-02	1.02E-01	1.08E-01	1.05E-01
	0.03	2.02E-02	2.60E-02	3.40E-02	4.10E-02	5.86E-02	6.60E-02	7.39E-02	8.04E-02	9.07E-02	9.47E-02	1.08E-01	1.07E-01	1.17E-01	1.10E-01
	0.05	2.47E-02	3.02E-02	4.18E-02	4.83E-02	7.38E-02	7.82E-02	9.19E-02	9.36E-02	1.12E-01	1.10E-01	1.28E-01	1.22E-01	1.37E-01	1.26E-01
	0.08	3.25E-02	3.86E-02	5.51E-02	6.20E-02	9.40E-02	9.83E-02	1.18E-01	1.17E-01	1.40E-01	1.35E-01	1.64E-01	1.45E-01	1.70E-01	1.45E-01
	0.10	3.86E-02	4.66E-02	6.45E-02	7.25E-02	1.12E-01	1.14E-01	1.37E-01	1.36E-01	1.67E-01	1.56E-01	1.88E-01	1.66E-01	2.02E-01	1.67E-01
	0.30	3.20E-02	4.43E-02	5.25E-02	6.85E-02	9.06E-02	1.07E-01	1.17E-01	1.32E-01	1.47E-01	1.58E-01	1.86E-01	1.90E-01	2.10E-01	2.06E-01
	0.50	1.96E-02	2.96E-02	3.22E-02	4.71E-02	5.70E-02	7.77E-02	7.53E-02	1.00E-01	9.80E-02	1.25E-01	1.30E-01	1.61E-01	1.53E-01	1.84E-01
	1.00	7.64E-03	1.37E-02	1.38E-02	2.24E-02	2.49E-02	3.91E-02	3.31E-02	5.11E-02	4.47E-02	6.76E-02	6.11E-02	9.09E-02	7.56E-02	1.10E-01
	2.00	2.06E-03	4.63E-03	4.27E-03	8.52E-03	9.20E-03	1.63E-02	1.28E-02	2.21E-02	1.74E-02	3.00E-02	2.43E-02	4.15E-02	3.00E-02	5.10E-02
3.00	6.52E-04	1.96E-03	1.70E-03	4.03E-03	4.27E-03	8.59E-03	6.46E-03	1.21E-02	9.38E-03	1.70E-02	1.35E-02	2.46E-02	1.72E-02	3.10E-02	
4.00	1.94E-04	9.41E-04	7.38E-04	2.20E-03	2.31E-03	5.20E-03	3.73E-03	7.73E-03	5.75E-03	1.11E-02	8.68E-03	1.63E-02	1.12E-02	2.07E-02	

11 Recommendations

Until it is determined which V_{s30} value is most applicable to the actual geologic conditions on which the Arcadia Dam was constructed, we recommend using ground motions determined for the more conservative V_{s30} estimate of 281 m/s. This V_{s30} measurement occurred close to the dam itself and may provide a better estimate of geologic conditions on which the Arcadia Dam was constructed. These results are shown in Table 10.2 and Figure 10.3. Geotechnical and as-built reports for the Arcadia Dam could help determine which V_{s30} measurement is most applicable to the site conditions. The choice to use the clustered area source model at a weight of 20% was arbitrarily chosen by the investigators. An independent panel of seismologist could evaluate the weight given to the different branches in the logic tree. This may be particularly important because there are no documented methods to deal with comparable changes in the seismicity rates for an area.

12 Acknowledgements

This work was funded in part through an inter-personnel agreement with the Army Corp of Engineers. We would like to thank Dr. Ken Luza and Dr. G. Randy Keller for the helpful comments and reviews, which improved this study. We would also like to thank Amie Gibson for locating a large number of earthquakes used in this study.

13 References

- Abrahamson, N. A., and Silva, W., 2008, Summary of the Abrahamson and Silva NGA Ground-Motion Relations: *Earthquake Spectra*, v. 24, no. 1, p. 67-97.
- Aki, M., 1965, Maximum likelihood estimate of b in the formula $\log N = a - bM$ and its confidence limits: *Bull. Earthquake Res. Inst., Tokyo Univ.*, v. 43, p. 237-239.
- Atkinson, G. M., 1993, Earthquake source spectra in eastern North America: *Bull. Seismol. Soc. Amer.*, v. 83, p. 1778-1798.
- , 2004, Empirical attenuation of ground-motion spectral amplitudes in Southeastern Canada and the Northeastern United States: *Bull. Seismol. Soc. Amer.*, v. 94, no. 3, p. 1079-1095.
- Bender, B., 1983, Maximum Likelihood Estimation of b Values for Magnitude Grouped Data: *Bull. Seismol. Soc. Amer.*, v. 73, no. 3, p. 831-851.
- Beyreuther, M., Barsch, R., Krischer, L., Megies, T., Behrd, Y., and Wassermann, J., 2010, ObsPy: A python tool for seismology: *Seismol. Res. Lett.*, v. 81, p. 530-533.
- Boore, D. M., and Atkinson, G. M., 2008, Ground-Motion Prediction Equations for the Average Horizontal Component of PGA, PGV, and 5%-Damped PSA at Spectral Periods between 0.01s and 10.0 s: *Earthquake Spectra*, v. 24, no. 1, p. 99-138.
- Boore, D. M., Watson-Laprey, J., and Abrahamson, N. A., 2006, Orientation-Independent Measures of Ground Motion: *Bull. Seismol. Soc. Amer.*, v. 96, no. 4, p. 1502-1511.
- Campbell, K. W., 2003, Prediction of strong ground motion using the hybrid empirical method and its use in the development of ground-motion (attenuation) relations in eastern North America: *Bull. Seismol. Soc. Amer.*, v. 93, p. 1012-1033.
- Campbell, K. W., and Bozorgnia, Y., 2008, NGA Ground Motion Model for the Geometric Mean Horizontal Component of PGA, PGV, PGD and 5Ranging from 0.01 to 10 s: *Earthquake Spectra*, v. 24, no. 1, p. 139-171.
- CEUS-SSC, 2012, Technical Report: Central and Eastern United States Seismic Source Characterization for Nuclear Facilities, EPRI, Palo Alto, CA, U.S. DOE, and U.S. NRC, p. 3176.
- Chiou, B. S.-J., and Youngs, R. R., 2008, An nga model for the average horizontal component of peak ground motion and response spectra: *Earthquake Spectra*, v. 24, no. 1, p. 173-215.
- Crone, A. J., and Luza, K. V., 1990, Style and timing of Holocene surface faulting on the Meers fault, southwestern Oklahoma: *Geological Society of America Bulletin*, v. 102, p. 1-17.
- Crowley, H., Monelli, D., Pagani, M., Silva, V., and Weatherill, G., 2012, OpenQuake User's Manual: *openquake.org*, no. 1.1, p. 130.
- Dangkua, D. T., and Cramer, C. H., 2011, Felt intensity versus instrumental ground motion: A difference between California and Eastern North America?: *Bull. Seismol. Soc. Amer.*, v. 101, no. 4, p. 1847-1858.
- Dobry, R., Borcherdt, R. D., Crouse, C. B., Idriss, I. M., Hoyner, W. B., Martin, G. R., Power, M. S., Rinne, E. E., and Seed, R. B., 2000, New Site Coefficients and Site Classification

- System Used in Recent Building Seismic Code Provisions: *Earthquake Spectra*, v. 16, no. 2, p. 41-56.
- FDSN, 2012, SEED Reference Manual, Seattle, WA, Incorporated Research Institutions for Seismology, 224 p.:
- Field, E. H., Jordan, T. H., and Cornell, C. A., 2003, OpenSSA: A Developing Community-Modelling Environment for Seismic Hazard Analysis: *Seismol. Res. Lett.*, v. 74, no. 4, p. 406-419.
- Gardner, J. K., and Knopoff, L., 1974, Is the Sequence of Earthquakes in Southern California, with Aftershocks Remove, Poissonian?: *Bull. Seismol. Soc. Amer.*, v. 64, no. 5, p. 1363-1367.
- Gutenberg, B., and Richter, C. F., 1944, Frequency of Earthquakes in California: *Bull. Seismol. Soc. Amer.*, v. 34, no. 4, p. 185-188.
- Ham, W. E., Denison, R. E., and Merritt, C. A., 1964, Basement rocks and structural evolution of southwestern Oklahoma: *Oklahoma Geological Survey Bulletin*, v. 95, p. 302.
- Hanks, T. C., and Kanamori, H., 1979, A Moment Magnitude Scale: *J. Geophys. Res.*, v. 84, no. 5, p. 2348-2350.
- Harlton, B. H., 1963, Frontal Wichita fault system of southwestern Oklahoma: *Am. Assoc. Petr. Geol. B.*, v. 47, p. 1552-1580.
- Havskov, J., and Ottemoller, L., 1999, SeisAn Earthquake Analysis Software: *Seismol. Res. Lett.*, v. 70, p. 532-534.
- Johnston, A. C., 1996a, Seismic moment assessment of earthquakes in stable continental regions--I. Instrumental seismicity: *Geophys. J. Int.*, v. 124, p. 381-414.
- , 1996b, Seismic moment assessment of earthquakes in stable continental regions--II. Historical seismicity: *Geophys. J. Int.*, v. 125, p. 639-678.
- Jones-Cecil, M., 1995, Structural controls of Holocene reactivation of the Meers fault, southwestern, Oklahoma, from magnetic studies: *Geological Society of America Bulletin*, v. 107, p. 98-112.
- Kanamori, H., and Anderson, D. L., 1975, Theoretical basis of some empirical relations in seismology: *Bull. Seismol. Soc. Amer.*, v. 65, p. 1073-1095.
- Kelson, K. I., and Swan, F. H., 1990, Paleoseismic History of the Meers Fault, Southwestern Oklahoma, and Implications for Evaluations of Earthquake Hazards in the Central and Eastern United States: Unpublished Report, p. 25.
- Lawson, J. E., 1985, Expected Earthquake Ground-Motion Parameters at the Arcadia, Oklahoma, Dam Site: *OGS Special Publication*, v. 85-1, p. 41.
- Luza, K. V., Madole, R. F., and Crone, A. J., 1987, Investigation of the Meers Fault, Southwestern, Oklahoma: *Oklahoma Geological Survey Special Publication*, v. 87-1, p. 75.
- Madole, R. F., 1988, Stratigraphic evidence of Holocene faulting in the mid-continent: The Meers fault, southwestern Oklahoma: *Geological Society of America Bulletin*, v. 100, p. 392-401.
- Miao, Q., and Langston, C. A., 2007, Empirical Distance Attenuation and the Local-Magnitude Scale for the Central United States: *Bull. Seismol. Soc. Amer.*, v. 97, no. 6, p. 2137-2151.
- Newmark, N. M., and Hall, W. J., 1982, *Earthquake spectra and design*, Oakland, CA, Earthquake Engineering Research Institute.

- Northcutt, R. A., and Campbell, J. A., 1995, Geological provinces of Oklahoma: Oklahoma Geological Survey Open File Report, v. OF5-95.
- Park, C. B., Miller, R. D., and Xia, J., 1999, Multichannel analysis of surface waves: *Geophys.*, v. 64, no. 3, p. 800-808.
- Petersen, M. D., Frankel, A. D., Harmsen, S. C., Mueller, C. S., Haller, K. M., Wheeler, R. L., Wesson, R. L., Zeng, Y., Boyd, O. S., Perkins, D. M., Luco, N., Field, E. H., Wills, C. J., and Rustales, K. S., 2008, Documentation for the 2008 Update of the United States National Seismic Hazard Maps, Volume Open-File Report 2008-1128, USGS, p. 128.
- Ramelli, A. K., and Slemmons, D. B., 1986, Neotectonic activity of the Meers fault: Oklahoma Geological Survey Guidebook, v. 24, p. 45-54.
- Scherbaum, F., 2007, *Of poles and zeros: Fundamentals of digital seismology*, Norwell, MA, Springer, 268 p.:
- Slemmons, D. B., Ramelli, A. K., and Brocoum, S., 1980, Earthquake potential of the Meers Fault, Oklahoma: Seismological Society of America Annual Meeting Abstracts, v. 80th.
- Stepp, J. C., 1972, Analysis of completeness of the earthquake sample in the Puget Sound area and its effect on statistical estimates of earthquake hazard: *Proc. Intern. Conf. Microzonation*, v. 2, p. 897-910.
- Toth, C. R., Holland, A. A., Keranen, K., and Gibson, A., 2012, Relocation and Comparison of the 2010 M4.3 and 2011 M5.6 earthquake sequences in Lincoln County, Oklahoma: *Seismol. Res. Lett.*, v. 83, no. 2, p. 419.
- USGS, 1994, Rault number 1031b, Meers fault, in Quaternary fault and fold database of the United States: , in Crone, A. J., ed., <http://earthquakes.usgs.gov/regional/qfaults>.
- , 2012a, Earthquake Search, http://earthquake.usgs.gov/earthquakes/eqarchives/epic/epic_rect.php, USGS.
- , 2012b, Hazard Curve Application, <http://geohazards.usgs.gov/hazardtool/application.php>, USGS Earthquake Hazards.
- Waldhauser, F., and Ellsworth, W. L., 2000, A double-difference earthquake location algorithm: Method and application to the northern Hayward fault: *Bull. Seismol. Soc. Amer.*, v. 90, p. 1353-1368.
- Weichert, D. H., 1980, Estimation of the earthquake recurrence parameters for unequal observation periods for different magnitudes: *Bull. Seismol. Soc. Amer.*, v. 70, no. 4, p. 1337-1346.
- Wells, D. L., and Coppersmith, K. J., 1994, New Empirical Relationships among Magnitude, Rupture Length, Rupture Width, Rupture Area, and Surface Displacement: *Bull. Seismol. Soc. Amer.*, v. 84, no. 4, p. 974-1022.

Appendix A - Table of Abbreviations

Abbreviation	Description
a	Gutenberg-Richter relationship for intercept with zero magnitude
ADOK	ADOK is the station code to represent the accelerometer located at the Arcadia Dam office
b, b-value	Gutenberg-Richter relationship for slope
B.P.	Before Present
C14	Carbon 14, C ¹⁴
CEUS	Central and Eastern United States
CEUS-SSC	Central and Eastern United States Seismic Source Characterization for Nuclear Facilities
CMT	Centroid moment tensor
E	Exponential $yE_x = y \times 10^x$
g	Alleceration due to gravity at see level nominally 9.81 m/s ²
GMRotI50	modified average horizontal acceleration
Hz	Hertz, measure of frequency
I0	Maximum Modified Mercalli Intensity
km	kilometers
km/s	velocity in kilometers per second
m	meters
M, M _w	Moment Magnitude
m/s	Velocity meters per second
MASW	Multichannel Analysis of Surface Wave
m _b	body wave magnitude
m _{bLg}	Lg body wave magnitude
M _d , M _D	Duration magnitude
MFA	magnitude estimated from felt area
M _L	local magnitude
M _{max}	Maximum magnitude considered in a particular traverse of the logic tree
MMI	Modified Mercalli Intensity
M _s , M _S	surface wave magnitude
OGS	Oklahoma Geological Survey
PSHA	Probabilistic Seismic Hazard Assessment
RMS	root of the mean square of the error
RMT	Regional moment tensor
SA	Spectral acceleration
UHS	Uniform Hazard Spectra, or mean equal hazard spectra
USGS	United States Geological Survey
Vs30	Shear-wave velocity to 30 meters depth
WFF	Wichita frontal fault system

